NUMERICAL STUDY OF PHASE TRANSITION PROBLEMS USING STRING METHOD

LI YUNZHI

NATIONAL UNIVERSITY OF SINGAPORE

2016

NUMERICAL STUDY OF PHASE TRANSITION PROBLEMS USING STRING METHOD
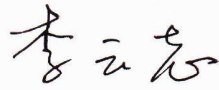
LI YUNZHI

(B.Sc.(Hons.), NUS)

A THESIS SUBMITTED

FOR THE DEGREE OF DOCTOR OF PHILOSOPHY

DEPARTMENT OF MATHEMATICS

NATIONAL UNIVERSITY OF SINGAPORE

2016

DECLARATION

I hereby declare that this thesis is my original work and it has been written by me in its entirety. I have duly acknowledged all the sources of information which have been used in the thesis.

This thesis has also not been submitted for any degree in any university previously.

LI YUNZHI
12 August 2016

Acknowledgements

I would like to express my sincerest thanks to my supervisor Associate Professor Ren Weiqing, for his invaluable guidance and support.

I also would like to thank Professor Bao Weizhu for his invitation to the SIAM conference. I am deeply benefited from the academic atmosphere.

I also appreciate Dr. Yao Wenqi for the helpful discussion on this thesis as well as for reading the draft.

Many thanks to NUS for awarding me the scholarship to support my study during my Ph.D candidature, and for the financial assistance for overseas conference.

Lastly, I would like to thank my families for both the emotional and material supports.

Contents

Contents   iv

Summary

Rare events play important roles in the dynamics of the complex system, such as the nucleation events during phase transition, conformational change of macromolecules, chemical reactions, etc. In this thesis, we focus on numerical studies of one type of rare events, the nucleation events during phase transition using the string method.

The main contributions of this thesis include:

1. Based on the string method in collective variables, we developed the climbing string method in collective variables focusing on the study of saddle points on the free energy landscape.

2. We apply the string method and its extensions to study three different phase transition problems using different mathematical models.

In the first problem, we numerically study the vapor condensation on hydrophobic surfaces patterned with microstructures using a phase field model. The critical nuclei, energy barriers and minimum energy paths (MEP) of nucleation process are determined using the climbing string method. Two nucleation scenarios are observed. In the case of high pillar, narrow interpillar spacing, low supersaturation level and low surface wettability, the critical nucleus is suspended with air trapped

inside the microstructures which leads to the Cassie state; otherwise, the liquid penetrates the microstructures which leads to the Wenzel state. Furthermore, it is observed that in the case of low pillar or wide interpillar spacing, the vapor condensate initially at the Cassie state will evolve to the Wenzel state after passing through the critical nucleus.

In the second problem, we numerically study the Wenzel-to-Cassie dewetting transition on a grooved solid surface on the free energy landscape, in which the mean force is computed using a molecular dynamics model. The free energy landscape is mapped in a set of collective variables, the coarse-grained density of fluid particles. We give a detailed mathematical formulation for the collective variables. The transition states, free energy barriers and minimum free energy paths (MFEP) are determined using the on-the-fly climbing string method. It is observed that the Wenzel-to-Cassie dewetting transition starts at the two bottom corners of the groove. At the transition state, the liquid droplet is completely detached from the bottom solid surface and a symmetric liquid meniscus is formed inside the groove.

In the last problem, we numerically study the isotropic-nematic phase transition in the hard spherocylinder system on the free energy landscape, in which the mean force is computed using a molecular dynamics model. Under specific pressure, the spherocylinders may exhibit both the isotropic phase and the nematic phase. The spherocylinders are randomly oriented and distributed in the former case and well aligned with each other in the latter case. The system can be characterized by an order parameter which measures the alignment of the spherocylinders in the nematic direction. We use the order parameter as the collective variable. The transition states, free energy barriers and minimum free energy paths (MFEP) are determined using the on-the-fly string method. At the transition state, it is observed that the critical nematic nucleus has a multilayer structure. Furthermore, under the effects of an external aligning field, the free energy barrier is lowered and the nucleation process is enhanced.

List of Figures

Introduction

The dynamics of a complex system is usually driven by some rare but important events, for example the nucleation events during phase transition, conformational change of macromolecules, chemical reactions, etc. The complex system stays at the metastable states for long periods with infrequent switching from one to another. Many sophisticated numerical methods have been developed to study the transition pathways, transition states and energy barriers between the metastable states, such as the nudged elastic band (NEB) method [29], the dimer method [28], the string method [15], etc. In this thesis, we focus on the applications of the string method in studying rare events.

1.1 The Minimum Energy Path and the String Method

Consider a system with a smooth energy landscape $V(x)$ with at least two local minima. Suppose the dynamics of the system is governed by the gradient flow under the effects of thermal noise given by

$$\dot{x}(t) = -\nabla V(x) + \sqrt{2\epsilon}\eta(t), \quad x \in \mathbb{R}^d, \tag{1.1}$$

where ϵ is the magnitude of the thermal effects and $\eta(t) \in \mathbb{R}^d$ is the white noise with $\langle \eta_i(t), \eta_j(t') \rangle = \delta_{ij}\delta(t - t')$. The term $\sqrt{2\epsilon}\eta(t)$ describes the thermal noise, which introduces thermal fluctuations to the dynamics of the system. When the thermal effects ϵ is much smaller than the energy barrier of $V(x)$, the dynamics of the system is mainly governed by the potential force $-\nabla V(x)$ and driven to the closest local minimum. The system will fluctuate around the local minimum for a very long period until a large thermal noise makes the system switch to another local minimum.

The transition pathways between the two local minima are defined as the trajectories by which the system hops from one local minimum to another. The most probable transition pathway is given by the minimum energy path (MEP) in the zero noise limit. By definition, the MEP is a smooth curve φ^* in the configuration space connecting the two local minima and satisfies the following:

$$(\nabla V)^{\perp}(\varphi^*) = 0, \tag{1.2}$$

where $(\nabla V)^{\perp}$ is the component of ∇V normal to φ^*. Moreover, the MEP passes through the saddle points of $V(x)$, at which the energy attains the local maxima along the MEP. Therefore the saddle points correspond to the transition states between the two local minima. From the saddle points, we can determine the activation energy barrier for the transition between the two local minima.

In Fig. 1.1, we use a two-dimensional Mueller potential as a simple example to illustrate the concept of MEP. The MEP is given by the yellow curve in the figure, whose two end points are located at the two local minima. It describes the most probable transition pathway between the two local minima. At each point along the MEP, the potential force $-\nabla V(x)$ is tangent to the MEP. The white dots are the saddle points, at which the energy attains the local maxima along the MEP (see Fig. 1.2).

String method was proposed by E, Ren and Vanden-Eijnden [15]. It has been demonstrated to be an efficient numerical tool for the computation of the MEP and
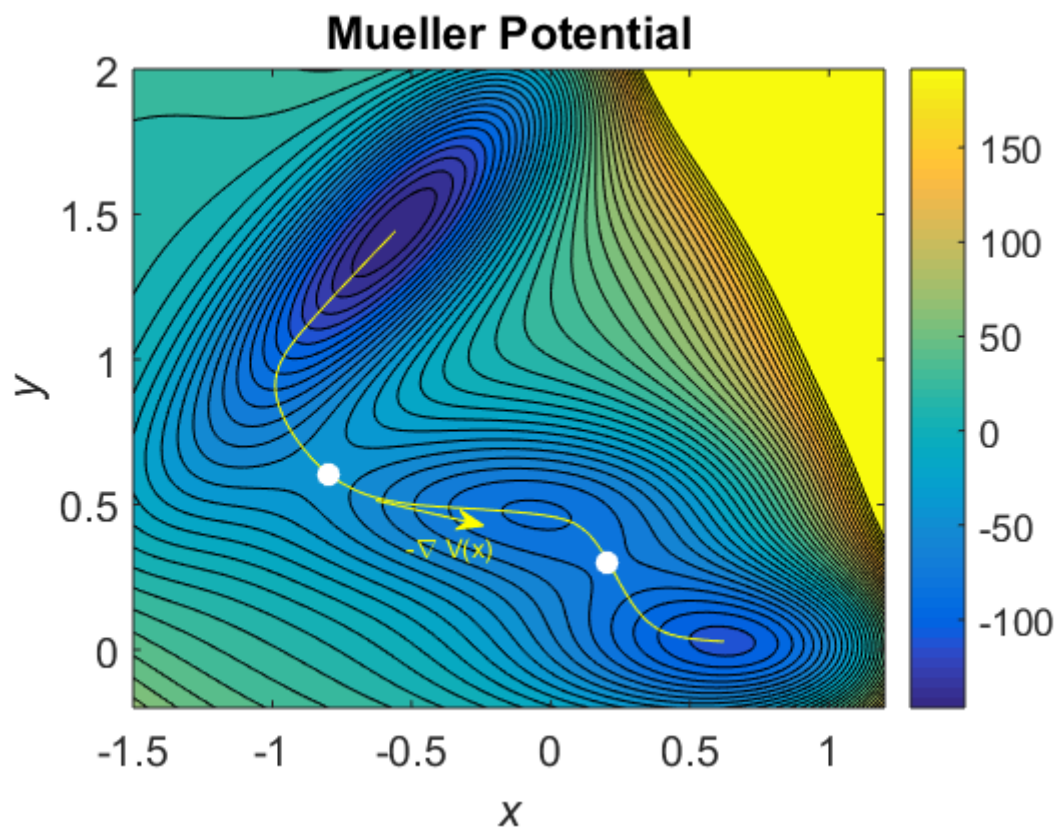
Figure 1.1: The MEP (yellow) and the saddle points (white). At each point along the MEP, the potential force $-\nabla V(x)$ is tangent to the MEP. The energy attains local maxima at the saddle points along the MEP (see Fig. 1.2).
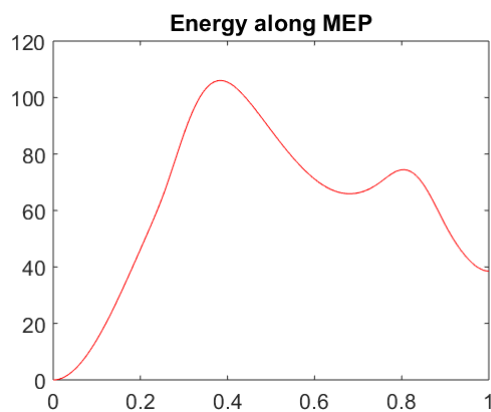
Figure 1.2: Energy profile along the MEP in Fig. 1.1. The local maxima of the energy correspond to the two saddle points.

the transition states. It was applied to study phase transitions in various systems, for example the magnetization reversal in sub-micrometer-sized ferromagnetic elements [13], the liquid-vapor transition in capillary tubes [43], the Cassie-to-Wenzel wetting transition on pillared surfaces [46].

The implementation of the string method is simple. Consider the following gradient system:

$$\dot{x}(t) = -\nabla V(x), \tag{1.3}$$

where the potential energy $V(x)$ is a smooth function. Suppose the system has two metastable states located at A and B, corresponding to the local minima of $V(x)$. We look for the MEP connecting A and B. An initial string is constructed in the configuration space connecting A and B with some suitable parametrization, for example equal arc length. Then the string is evolved according to a differential equation, which guarantees the convergence of the string to the MEP connecting A and B. Simply speaking, the string is evolved using the steepest descent dynamics while keeping an intrinsic parametrization along the string. After the MEP is identified, the saddle points and energy barriers can be computed from the local maxima of the energy along the MEP.

1.2 The Climbing String Method

In case when two local minima are given in a gradient system, the string method allows to compute the MEP connecting the two local minima. However, in case when only one local minimum is given, we want to find out the transition pathways by which the system moves out of the basin of attraction at the given local minimum. The original string method is no longer applicable. The climbing string method is a modified version of the string method proposed by Ren and Vanden-Eijnden [45] focusing on the study of saddle points on the potential energy landscape. The most probable transition pathway for the system leaving the given local minimum is given by half of the MEP connecting the local minimum and the saddle point.

Consider the same gradient system given by Eq. 1.3. We start from the local minimum A. We look for the saddle points directly connected to A. An initial string is constructed in the configuration space, whose two end points are located at the local minimum A and a small perturbation from A. During the string evolution, one end point of the string is fixed at A and the other end point evolves to the saddle point of $V(x)$ with a modified potential force in which the component of potential force tangent to the string is reversed. The string converges to half of the MEP connecting the local minimum and the saddle point at the steady state.

1.3 The Minimum Free Energy Path and the String Method in Collective Variables

The string method and climbing string method require the energy landscape of the system be smooth. However, the dynamics of a complex system are usually stochastic in nature due to the thermal effects. Therefore, we need to take the thermal effects into account, for example in the study of molecular dynamics system. The corresponding energy landscape is very rough, thus the string method and climbing string method are not applicable in this case.

To overcome this difficulty, we change our view by looking at the system in a few collective variables of interest rather than the entire configuration space. For example, the conformational change of the macromolecules are usually characterized by the change of the dihedral angles in the macromolecules. Thus the dihedral angles are chosen as the collective variables to describe the system. Many numerical methods have been developed to map the free energy of the system in the collective variable space, such as the adaptive biasing force [11], the adiabatic molecular dynamics [47] and the metadynamics [32]. The free energy landscape defined in the collective variable space is usually much smoother than the original energy landscape defined in the configuration space. Thus the string method and climbing

string method can be implemented to study the transition mechanism in the collective variable space.

The string method in collective variables was proposed by Maragliano and Vanden-Eijnden [38]. It combines the string method and some biased sampling techniques to determine the minimum free energy paths (MFEP) on the free energy landscape. The definition of MFEP is derived from the MEP in the configuration space. By definition, it describes the most probable transition pathway between two local minima in the collective variable space. Along the MFEP, the free energy attains the local maxima at the saddle points on the free energy landscape. If the collective variables are well chosen, then the saddle point indeed describes the transition state. The significance of the collective variables can be verified by computing the committor value distribution at the saddle point, which will be discussed in chapter 2.

For the implementation of the string method in collective variables, firstly we need to choose a set of collective variables z to describe the system, such as the dihedral angles used in the study of the conformational change of the macromolecules. Let $F(z)$ be the free energy of the system mapped in the collective variable space. Suppose $F(z)$ has two local minima z_A and z_B. We look for the MFEP connecting z_A and z_B. An initial string is constructed in the collective variable space, connecting z_A and z_B with some intrinsic parametrization such as equal arc length. The string evolves according to a differential equation similar to that in the string method. In contrast, the mean force on the string is computed via a time-averaging approach using restrained molecular dynamics simulations. The string converges to the MFEP at the steady state. After the MFEP is identified, the free energy profile along the MFEP can be computed by thermodynamic integrations. The saddle points and the free energy barriers can be determined from the local maxima of the free energy along the MFEP.

1.4 The Climbing String Method in Collective Variables

As a major contribution of this thesis, we extend the string method in collective variables to the climbing string method in collective variables, focusing on the study of saddle points on the free energy landscape. We explain in details, the theoretical derivation and algorithm of this new method in chapter 2. Then we use the conformational change of alanine dipeptide as an example to test this new method. The transition state between two metastable conformers of alanine dipeptide is identified from the saddle point on the free energy landscape. Our result is consistent with the work done by Maragliano and Vanden-Eijnden [38].

1.5 The On-the-fly String Method

In the string method in collective variables, the computation of the mean force at each step during the string evolution is very costly. The on-the-fly string method proposed by Maragliano and Vanden-Eijnden [39] is a modified version of the string method in collective variables which avoids the computation of the mean force. It has been shown to be more efficient and stable than the original string method in collective variables.

For the implementation of the on-the-fly string method, the string is initially discretized into a finite number of images uniformly distributed along the string. Each image is assigned a molecular dynamics (MD) replica constrained at the corresponding image. In the computation, the discretized string is evolved concurrently with the MD replicas, where the evolution of the MD replicas is governed by restrained MD simulations. The evolution of the MD replicas provides on-the-fly the data to evolve the discretized string, thus the computation of the mean force at each step is avoided. The string converges to the MFEP connecting the two local minima when it reaches the steady state.

The techniques of the 'on-the-fly' computation can be applied to the climbing string method in collective variables directly. Base on that, we develop the on-the-fly climbing string method, which is more efficient than the climbing string method in collective variables.

1.6   Applications to Phase Transition Problems

In this thesis we focus on the numerical studies of one type of rare events, the nucleation events during phase transition. Phase transition is the transformation of the system from one metastable phase to another. A daily example is the transition between solid, liquid and gaseous states of matters. As in first-order phase transition, nucleation process is involved which refers to the formation and growth of a nucleus of new phase. When the nucleus reaches the critical size, it becomes stable and grows further followed by the entire system evolving to the new phase. The nucleation event is a rare event, since it involves crossing of an energy barrier in order to form the critical nucleus.

We study the following three different phase transition problems using different mathematical models:

1. Vapor condensation on hydrophobic surfaces patterned with microstructures using a phase field model (chapter 3).

2. Wenzel-to-Cassie transition of a liquid droplet on a grooved solid surface using a molecular dynamics model (chapter 4).

3. Isotropic-nematic phase transition in the hard spherocylinder system using a molecular dynamics model (chapter 5).

Next, we give an introduction to each problem.

Problem 1: Vapor condensation on hydrophobic surfaces patterned with microstructures

Vapor condensation is ubiquitous in nature and plays an important role in a wide range of applications. It has been the subject of theoretical and experimental studies for a long time. As a first-order phase transition, vapor condensation occurs via nucleation followed by the growth of nucleus. The process may occur via either homogeneous nucleation or heterogeneous nucleation, depending on whether the nucleus is formed in the bulk of vapor phase, or in contact with a foreign object, such as a solid substrate. The nucleation process under microscopic scale has been investigated extensively using computer simulations, such as biased molecular dynamics, Monte Carlo methods in conjunction with umbrella sampling techniques and constrained minimization [2, 3, 8, 27, 35, 36, 40–42, 51, 53, 55, 56, 61, 63, 65]. In this thesis, we study the mechanism of vapor condensation on hydrophobic surfaces patterned with microstructures using the climbing string method [15, 45].

Superhydrophobic surfaces patterned with microstructures have attracted much attention in both the industry and the scientific community in recent years due to their unique wetting properties and a wide range of applications in practice, such as defrosting, anti-icing and self-cleaning [7, 10, 12, 37]. It is well-known now, the hydrophobicity of the surface can be greatly enhanced with nano- and microscale structures. On such surfaces, water may exhibit either the suspended Cassie state [9] or the impaled Wenzel state [60], depending on whether the air is trapped inside the microstructures, see Fig. 1.3. The hydrophobicity of the surface is enhanced if the Cassie state is formed. In contrast, the hydrophobicity of the surface is lowered if the Wenzel state is formed. We investigate the effects of different microstructures on the vapor condensation process, i.e. the wetting states of the vapor condensate during its formation and growth.

The effect of the microstructures on the vapor condensation process was recently studied by Guo et al. [26] using a lattice functional model. The free energy as a function of volume of nucleus is computed using a constrained minimization method, and the critical nucleus is identified from the maximum of the free energy. While the two nucleation scenarios are successfully observed, i.e. the critical nucleus taking
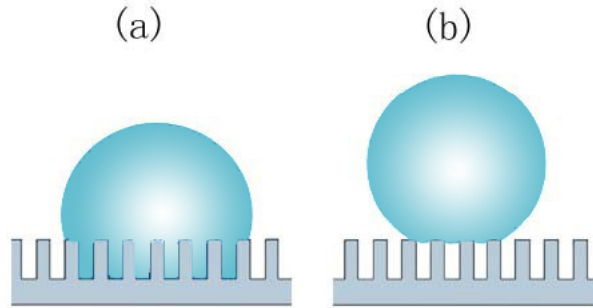
Figure 1.3: Wenzel state and Cassie state of a liquid droplet on a surface patterned with microstructures.

either the Cassie state or the Wenzel state. However, the method is based on the prescription of the volume of the nucleus as a reaction coordinate, which may lead to inaccurate critical nucleus and energy barrier. Furthermore, the sequence of minimizers using constrained minimization, parametrized by the volume of the nucleus has no dynamic significance.

In this thesis, the system under our study consists of a two-phase fluid on a solid substrate modelled by the density field of fluid. The solid substrate is patterned with a square lattice of rectangular pillars. The potential energy of the system is expressed as a functional of the density field. We study the nucleation process and accurately determine the critical nuclei, energy barriers and MEP using the climbing string method. Starting from the vapor state, which is a local minimum of the potential energy, we use climbing string method to determine the saddle points and at the same time, the MEP connecting the vapor minimum and the saddle points. From the saddle points, we can determine the critical nuclei. The MEP shows the pathway for the formation of the critical nucleus. Once the critical nucleus is identified, the subsequent growth to the liquid phase is computed from the steepest descent dynamics with (perturbed) saddle point as the initial condition.

Two nucleation scenarios are observed: in case of high pillar, narrow interpillar spacing, low supersaturation level and low surface wettability, the critical nucleus prefers the Cassie state; otherwise, the critical nucleus prefers the Wenzel state. A

comparison of the energy barrier with nucleation on a flat surface with the same material reveals that the nucleation process is inhibited in the former case and enhanced in the latter case. The effects of the pillar height, interpillar spacing, supersaturation level and the intrinsic wettability of the solid surface on the nucleation process are investigated. The critical values of pillar height, interpillar spacing and supersaturation level at which the critical nucleus changes from the Wenzel state to the Cassie state are identified from the phase diagram. It is observed that the critical value of interpillar spacing follows closely to the critical radii in the homogeneous nucleation. Moreover, in case of low pillar or wide interpillar spacing, the vapor condensate initially at the Cassie state will evolve to the Wenzel state during the relaxation after passing through the critical nucleus.

Problem 2: Wenzel-to-Cassie transition of a liquid droplet on a grooved solid surface

The hydrophobicity of the surface can be enhanced with nano- and microscale structures. On such a surface, the liquid droplet may exhibit either the suspended Cassie state or the impaled Wenzel state as shown in Fig. 1.3. The hydrophobicity of the surface is enhanced in the former case and lowered in the latter case. Thus understanding the transition mechanism between the Wenzel state and the Cassie state on surfaces patterned with microstructures is important for the design of superhydrophobic surfaces.

The existence of the Wenzel state and the Cassie state and the transition between them are studied extensively using computer simulations [30, 48, 49], [21–24, 46, 66]. Savoy et al. [49] used forward flux sampling and molecular dynamics to study the wetting transition of an oily fluid on a surface of nails. Ren and Zhang [46], [66] used a phase field model to study the wetting of a liquid droplet on hydrophobic surfaces patterned with microscale pillars. The transition pathways, transition states and energy barriers are determined using the string method. Giacomello et al. [21–24] studied wetting transition of a submerged hydrophobic cavity of nanometer size using both atomistic and continuum models.

Azar, Ali and Kristen [52] investigated the wetting states of a liquid droplet on grooved surfaces using molecular dynamics simulations. It is observed that the liquid droplet may exhibit both the suspended Cassie state and the impale Wenzel state under specific structures of the groove. The energy barrier between the Cassie state and the Wenzel state is much larger than the thermal effects $k_B T$ in the molecular dynamics system. Therefore the transition between the Cassie state and the Wenzel state becomes a rare event.

In this thesis, we study the Wenzel-to-Cassie transition based on the molecular dynamics model above. We choose the coarse-grained density of fluid particles in the molecular dynamics system as the collective variables, following the works done by Giacomello et al. [21–24]. As a major contribution of the thesis, we give a detailed mathematical formulation for the collective variables. The phase transition is then studied on the free energy landscape mapped in the collective variable space. The transition pathways, transition states and free energy barriers are determined using the on-the-fly climbing string method. Starting from the Wenzel state, which is a local minimum of the free energy, we use the on-the-fly climbing string method to determine the saddle point and at the same time, the MFEP connecting the Wenzel state and the saddle point. The MFEP describes the most probable pathway for the dewetting process from the Wenzel state to the Cassie state. It is observed that the dewetting process starts from the two bottom corners of the groove. From the saddle point, we determine the transition state. It is observed that at the transition state, the liquid droplet is completely detached from the bottom solid surface and a symmetric liquid meniscus is formed inside the groove.

Problem 3: Isotropic-nematic phase transition in the hard spherocylinder system

A spherocylinder consists of a cylinder capped with hemispheres at the two ends. Let L and D be the length and the diameter of the central cylinder part. In case of $L/D = 0$, the spherocylinder is just a spherical particle. While in case of $L/D = \infty$, the spherocylinder is an infinitely thin needle. The term 'hard' refers to the collisions

as the only interactions among the spherocylinders.

The study of the hard spherocylinder system trace back to 1970s and work done by Vieillard-Baron, Jacques [59] and Few, Rigby [16]. Since then, the study of the hard spherocylinder system attracts much attention due to its similarity to the colloidal materials in nature, such as rodlike virus particles [4] and colloidal silicon rods [31]. Rebertus and Sando studied the hard spherocylinder system using molecular dynamics simulations [44]. It is shown that under high density and large length-to-width ratio L/D, the spherocylinders prefer alignments with each other, which leads to the nematic phase; otherwise, the spherocylinders prefer random distributions and orientations, which leads to the isotropic phase. Later on, Veerman, Bolhuis, Frenkel gave a report on the phase diagram of the hard spherocylinder system with respect to the density of the spherocylinders and the length-to-width ratio L/D [58], [5]. Under specific condition of the density and length-to-width ratio L/D, the isotropic phase and nematic phase may coexist as metastable states. Thus, the isotropic-nematic phase transition in the hard spherocylinder system becomes a rare event. The isotropic-nematic phase transition in the hard spherocylinder system was investigated by Frenkel and his co-workers using molecular dynamics and Monte Carlo simulations [18, 20, 50]. In [50], Schilling and Frenkel studied the problem using Monte Carlo simulations. It is observed that a lamella crystallite is formed at the early stage of the isotropic-nematic phase transition. The subsequent thickening of the lamella is hindered by the fact that top and bottom surfaces of the crystallite are preferentially covered by the spherocylinders that align parallel to the surface.

The isotropic-nematic phase transition in the hard spherocylinder system is purely driven by the entropic effects since the particles interact exclusively with each other via excluded volume [19]. There are two kinds of entropies competing with each other during phase transition: orientational entropy and translational entropy. The former favors the random distribution and orientation of hard spherocylinders corresponding to the isotropic phase. And the latter favors the uniform

distribution of the hard spherocylinders to minimize the excluded volume corresponding to the nematic phase. The system controlled by entropic effects can be characterized by some orientational order parameters. For example in the spherical particle system, the Steinhardt order parameters [54] are widely used to describe the crystal structures, such as simple cubic lattice, face-centered cubic (fcc) lattice and body-centered cubic (bcc) lattice. Yu et al. [64] used the Steinhardt order parameters to explore the free energy landscape and study the phase transitions between different crystal structures using the string method. Similarly, the hard spherocylinder system can be characterized by an order parameter, which measures the nematic ordering of the system, i.e. the alignment of the spherocylinders with respect to a common direction, the nematic direction.

In this thesis, we make a strong assumption by fixing the nematic direction in advance. Thus the order parameter by our definition measures the alignments of the spherocylinders with respect to the prescribed nematic direction. The order parameter is chosen as the collective variable and the phase transition is studied on the free energy landscape mapped in the collective variable space. The transition states, free energy barriers and MFEP are determined using the on-the-fly string method. The MFEP shows the pathway for the formation and growth of the nematic nucleus. The saddle points and the free energy barriers can be determined from the maximum of the free energy along the MFEP. From the saddle point, we determine the transition state. It is observed that at the transition state, the critical nematic nucleus has a multilayer structure. Furthermore, we investigate the effects of an external aligning field on the isotropic-nematic phase transition. It is observed that the external aligning field lowers the free energy barrier for the isotropic-nematic phase transition, thus enhances the nucleation process.

The three problems are arranged in the order of increasing complexities. For the phase field model used in the problem 1, the potential energy of the system is defined as a functional of the density field of fluid. Although the dimension of the system is large, the energy landscape is smooth. In contrast, the molecular dynamics model

used in the problems 2 and 3 are stochastic in nature and the corresponding energy landscapes are non-smooth or even discontinuous. Thus the problem 2 and 3 are more complicated than the problem 1. Furthermore in the problem 2, the interaction between particles is modelled by the pairwise Lennard-Jones potential [33] given by

$$V(r) = 4\epsilon \left[\left(\frac{\sigma}{r} \right)^{12} - \left(\frac{\sigma}{r} \right)^{6} \right], \tag{1.4}$$

where r is the distance between two particles, ϵ is the depth of potential well and σ is the distance for zero potential. The pairwise potential $V(r)$ is a continuous function for $r > 0$. In contrast in the problem 3, the spherocylinders interact with each other via collisions only. The pairwise potential U between two spherocylinders [44] is given by

$$\begin{cases} U = \infty & \text{if collision occurs,} \\ U = 0 & \text{otherwise.} \end{cases} \tag{1.5}$$

The potential energy of the hard spherocylinder system is discontinuous. Thus the problem 3 is more complicated than the problem 2.

Chapter 2

Theoretical Background and the Algorithm of String Method

In this chapter, we develop the climbing string method in collective variables which focuses on the saddle point search on the free energy landscape. This is a major contribution of this thesis. The details of the algorithm and its application in studying conformational change of alanine dipeptide are discussed.

Firstly, we review the string method [15] and climbing string method [45]. We use the two dimensional Mueller potential as a simple example to illustrate the performance of the two methods. The minimum energy paths (MEP), energy barriers and saddle points are determined using the two methods.

Secondly, we go through the string method in collective variables [38]. It combines the string method and some biased sampling techniques to determine the minimum free energy path (MFEP), which corresponds to the most probable transition pathway between two metastable states in the collective variable space. The saddle points and free energy barriers can be determined from the maximum of the free energy along the MFEP.

Thirdly, we explain the concepts of the MFEP, committor function and isocommittor surface [38]. Based on these concepts, we extend the string method in

collective variables to the climbing string method in collective variables. The details of the algorithm are discussed in this section.

At last, we discuss the on-the-fly string method [39] which is an improved and simplified version of the string method in collective variables. It has been shown to be more efficient and stable than the original method. The techniques of the 'on-the-fly' computation can be applied to the climbing string method in collective variables directly. Based on that, we have the on-the-fly climbing string method. We use the conformational change of alanine dipeptide as an example to test the new method. The transition pathways and transition states are determined on the free energy landscape. Our results show good consistency with Ref. [38].

2.1 The String Method

Consider the system modelled by the following dynamics:

$$\gamma \dot{x}(t) = -\nabla V(x) + \xi(t), \quad x \in \mathbb{R}^d, \tag{2.1}$$

where γ is the friction coefficient, $V(x)$ is the potential energy and $\xi(t) \in \mathbb{R}^d$ are the white noise with $\langle \xi_i(t')\xi_j(t) \rangle = 2\gamma k_B T \delta_{ij} \delta(t - t')$. Suppose the potential energy $V(x)$ is a smooth function with two local minima at A and B. We look for the MEP, which is the most probable transition path between A and B in the zero noise limit. By definition, the MEP is a smooth curve φ^* defined in the configuration space connecting A and B satisfying

$$(\nabla V)^\perp(\varphi^*) = 0, \tag{2.2}$$

where $(\nabla V)^\perp(\varphi^*)$ is the component of ∇V normal to φ^*.

String method was proposed by E, Ren and Vanden-Eijnden [15] to study the transition states and MEP in the system above. Firstly, an initial string $\varphi(\alpha)$ is constructed in the configuration space connecting A and B, where $\alpha \in [0, 1]$ is for some suitable parametrization such as equal arc length. Let $\varphi(\alpha, t)$ be the

instantaneous position of $\varphi(\alpha)$ at time t during the string evolution. The string is evolved according to the following differential equation:

$$\begin{cases} \varphi_t(\alpha, t) = -[\nabla V(\varphi)]^\perp + \gamma_\alpha \tau_\alpha \text{ for } \alpha \in (0, 1), \\ \varphi(0, t) = A, \quad \varphi(1, t) = B, \end{cases} \tag{2.3}$$

where γ_α is a Lagrangian multiplier uniquely determined by the choice of parametrization. $\tau_\alpha = \frac{\partial \varphi}{\partial \alpha} / |\frac{\partial \varphi}{\partial \alpha}|$ is the unit tangent vector along the string at $\varphi(\alpha)$. The stationary solution of Eq. 2.3 is the MEP connecting A and B.

An improved and simplified version of the string method is proposed in [14]. In the simplified string method, we simply replace the term $[\nabla V(\varphi)]^\perp$ with $\nabla V(\varphi)$ in Eq. 2.3, thus the computation of the projection onto the subspace perpendicular to the string is avoided. Therefore the simplified version is easier to implement. It also has been proved to have better stability than the old version.

In practice, the differential equation 2.3 can be solved by a time-splitting method. Firstly, the string is discretized into $R + 1$ images $\{\phi^0, \phi^1, ..., \phi^R\}$ uniformly distributed along the string. Secondly, the discretized string is moved according to the potential force $-\nabla V(x)$ with a discrete time step Δt. After each step of evolution, we reparametrize the string to enforce equal arc length among the contiguous images.

Algorithm of the string method

Let ϕ_n^k be the instantaneous position of the image ϕ^k at the n-th iteration during the string evolution. To update the discretized string at the n-th iteration, we proceed to the following 2 steps:

1. Evolve the intermediate images for one time step according to

$$\phi^{k,*} = \phi_n^k - \nabla V(\phi_n^k)\Delta t, \text{ for } k = 1, ..., R - 1. \tag{2.4}$$

   Let $\phi^{0,*} = A$ and $\phi^{R,*} = B$. We end up with a set of new images $\{\phi^{0,*}, \phi^{1,*}, ..., \phi^{R,*}\}$.

2. Interpolating a curve through the images $\{\phi^{0,*}, \phi^{1,*}, ..., \phi^{R,*}\}$ with a suitable interpolation, for example piecewise linear interpolation. Then distribute $R+1$
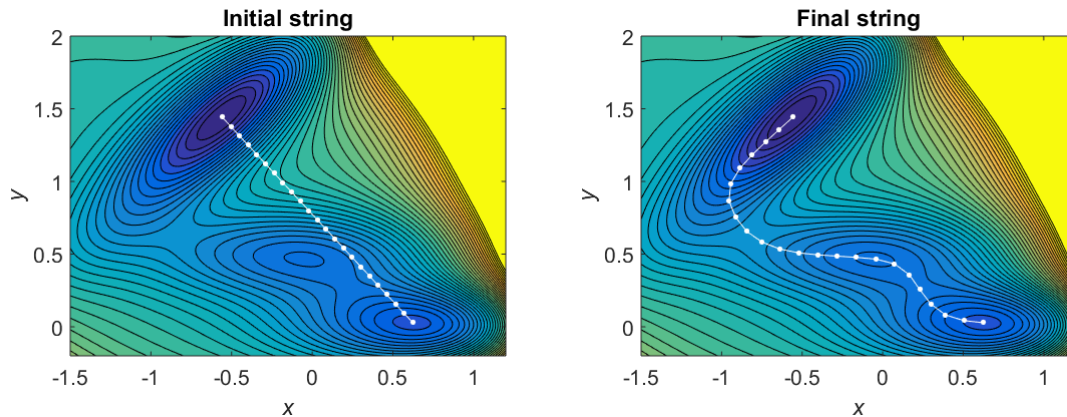
Figure 2.1: The string is discretized into 23 images. The initial string is a straight line connecting the two local minima. The string converges to the MEP at the steady state. The MEP passes through two saddle points and another local minimum. The pictures are taken from Eric Vanden-Eijnden's Homepage.

new images uniformly along this interpolated curve according to the equal arc length parametrization to obtain the string $\{\phi_{n+1}^0, \phi_{n+1}^1, ..., \phi_{n+1}^R\}$ at the new iteration. Go to step 1 or stop when the string reaches the steady state.

The application of the string method to study the MEP on Mueller potential can be found on Eric Vanden-Eijnden's homepage. The initial string is a line connecting the two local minima with linear interpolation as shown in Fig. 2.1 (left). The string is discretized into 23 images uniformly distributed along the string. The discretized string is then evolved according to the algorithm above, with a discrete time step $\Delta t = 2.5 \times 10^{-5}$. It finally converges to the MEP as shown in Fig. 2.1 (right). The energy profile along the MEP shown in Fig. 2.2 indicates the energy attains the maxima at the saddle points. Along the MEP, there is another local minimum between the two saddle points.

2.2 The Climbing String Method

Climbing string method was proposed by Ren and Vanden-Eijnden [45] focusing on the study of saddle points. Consider the system discussed in the previous section
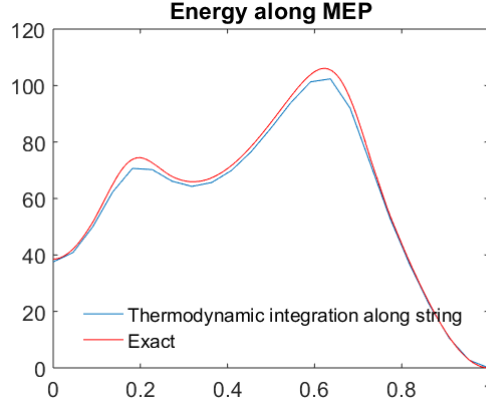
Figure 2.2: Energy profile along the MEP. The red curve shows the exact potential energy computed at each image. The blue curve shows the potential energy computed using thermodynamics integration. The picture is taken from Eric Vanden-Eijnden's Homepage.

modelled by Eq. 2.1. We start from the local minimum A. The climbing string method allows one to compute the saddle points directly connected to the given local minimum A. At the beginning, a string $\varphi(\alpha)$, $\alpha \in [0, 1]$ is constructed in the configuration space, with one end point fixed at A. The other end point of $\varphi(\alpha)$ is defined by a small perturbation of A, denoted as ϕ_0. Let $\varphi(\alpha, t)$ be the instantaneous position of $\varphi(\alpha)$ at time t during the string evolution. Then the string is involved according to the following differential equation:

$$\begin{cases} \varphi_t(\alpha, t) = -\nabla V(\varphi) + \gamma_\alpha \tau_\alpha \text{ for } \alpha \in (0, 1), \\ \varphi_t(1, t) = -\nabla V(\varphi) + 2 \langle \nabla V(\varphi), \tau_1 \rangle \tau_1, \\ \varphi(0, t) = A, \quad \varphi(1, 0) = \phi_0, \end{cases} \tag{2.5}$$

where γ_α and τ_α are defined previously in the string method. $<,>$ denotes the inner product. The stationary solution of Eq. 2.5 is half of the MEP connecting A and the saddle point. During the string evolution, the starting point $\varphi(0)$ is fixed at the local minimum A. The final point $\varphi(1)$ evolves according to the second equation above. In the second equation, $\langle \nabla V(\varphi), \tau_1 \rangle \tau_1$ is the projection of $\nabla V(\varphi)$ onto the tangent direction of the string, as a result the potential force on the final point is reversed in the direction tangent to the string. Thus the final point of the string climbs uphill

towards a saddle point on the energy landscape. In the subspace perpendicular to the string, the system relaxes following the original steepest descent dynamics.

In practice, the differential equation above can be solved by a time-splitting method. Firstly, the string is discretized into $R+1$ images $\{\phi^0, \phi^1, ..., \phi^R\}$ uniformly distributed along the string. The discretized string is evolved using a discrete time step Δt. During the evolution, the first image ϕ^0 is fixed at A. The intermediate images $\phi^1, ..., \phi^{R-1}$ are moved according to the potential force $-\nabla V$. The end image ϕ^R is moved according to the second equation in Eq. 2.5, solved using the forward Euler method. After each step of evolution, we reparametrize the string to enforce equal arc length among the contiguous images.

Algorithm of the climbing string method

Let ϕ^k_n be the instantaneous position of the image ϕ^k at the n-th iteration during the string evolution. To update the discretized string at the n-th iteration, we proceed to the following 3 steps:

1. The first image is fixed at the local minimum A, i.e. $\phi^{0,*} = A$. The intermediate images of the string are moved for one time step according to

$$\phi^{k,*} = \phi^k_n - \nabla V(\phi^k_n)\Delta t \text{ for } k = 1, ..., R-1, \quad (2.6)$$

and the last image is moved for one time step according to

$$\phi^{R,*} = \phi^R_n - \left[\nabla V(\phi^R_n) - 2\left\langle \nabla V(\phi^R_n), \hat{\tau} \right\rangle \hat{\tau}\right]\Delta t. \quad (2.7)$$

We end up with a set of new images $\{\phi^{0,*}, ..., \phi^{R,*}\}$.

2. A constraint is imposed to ensure increasing of energy monotonically along the string. For each image $\phi^{k,*}$, the energy is computed. If the energy is monotonically increasing, then we proceed to step 3 directly. Otherwise, we identify the J-th image at which the energy first attains local maximum along the string. Then we do a truncation at the J-th image, the resulting sequence of images are $\{\phi^{0,*}, ..., \phi^{J-1,*}\}$.
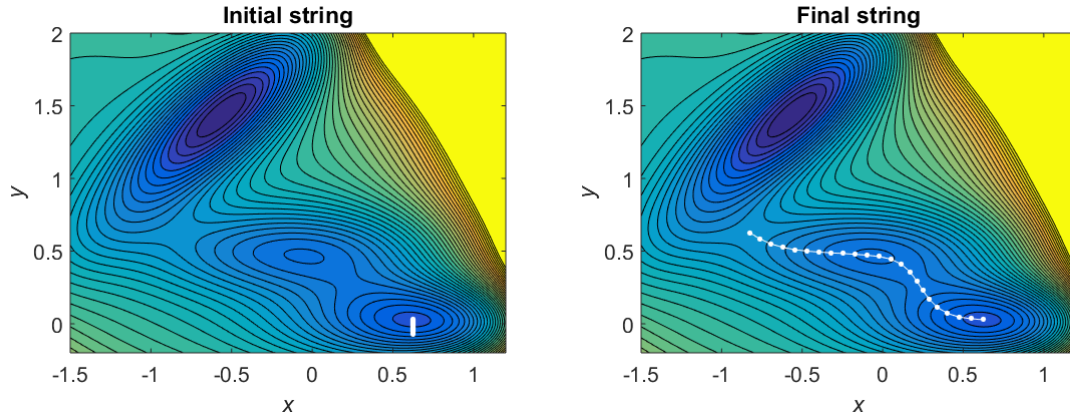
Figure 2.3: The final point of the initial string is given by a small perturbation from the local minimum downwards. If we discard truncation step in the climbing string method, then the final point converges to the saddle point which is not directly connected to the given local minimum.

3. Interpolate a curve through the images obtained from step 2 with a suitable interpolation, for example piecewise linear interpolation. Then distribute $R+1$ new images uniformly along this interpolated curve according to the equal arc length parametrization to obtain the string $\{\phi_{n+1}^0, \phi_{n+1}^1, ..., \phi_{n+1}^R\}$ at the new iteration. Go to step 1 or stop when the string reaches the steady state.

The truncation in step 2 is to guarantee that the saddle points computed are directly connected to the given local minimum A. Without the truncation, we may end up with the saddle point which is not directly connected to A as shown in Fig. 2.3. However, if the initial string is chosen properly, the final point converges to the saddle point directly connected to the given local minimum even if we discard the truncation step as shown in Fig. 2.4. That means the truncation in step 2 is not compulsory if the initial string is chosen properly.

Furthermore, in case of multiple saddle points connecting to the given local minimum, the saddle point computed using the climbing string method strongly depends on the perturbation of the initial string. For example in the Mueller potential, the local minimum located at $x = -0.05, y = 0.4667$ are connected to two saddle points. As shown in Fig. 2.5, if the initial perturbation is made towards left, then the final
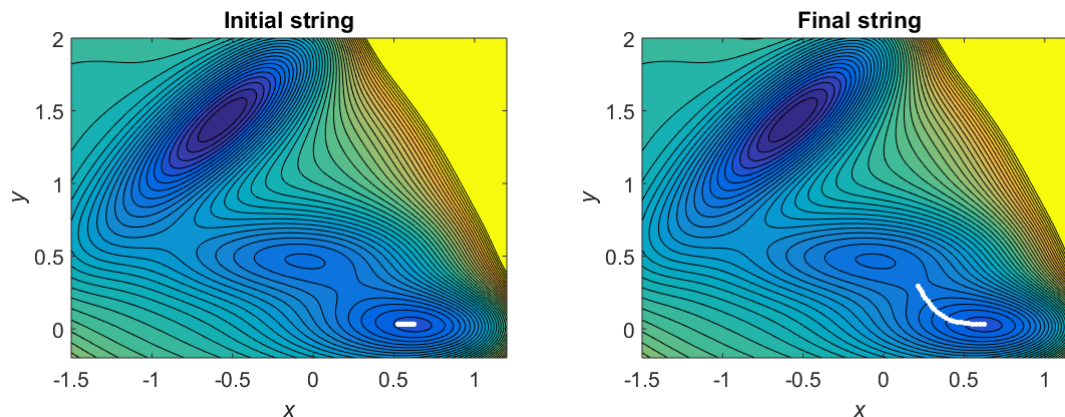
Figure 2.4: The final point of the initial string is given by a small perturbation from the local minimum towards left. Even if we discard the truncation step in the climbing string method, the final point still converges to the saddle point directly connected to the given local minimum.

point of the string converges to the saddle point on the left; otherwise, if the initial perturbation is made towards right, it converges to the saddle point on the right.

2.3 The String Method in Collective Variables

In this section, firstly we recall the concepts of collective variables, free energy and minimum free energy path (MFEP). Secondly, we recall the string method in collective variables in studying the transition states, free energy barriers and MFEP. Finally, we explain the concepts of committor function and isocommittor surfaces, which are used to define the transition state and transition region for a given reaction.

2.3.1 The Minimum Free Energy Path

Consider the molecular dynamics system under NVT ensemble. Let $x = (x_1, ..., x_n)$ be the positions of the particles. The probability density function of the system follows the Boltzmann distribution given by

$$\rho(x) = Z^{-1} e^{-\beta V(x)}, \tag{2.8}$$
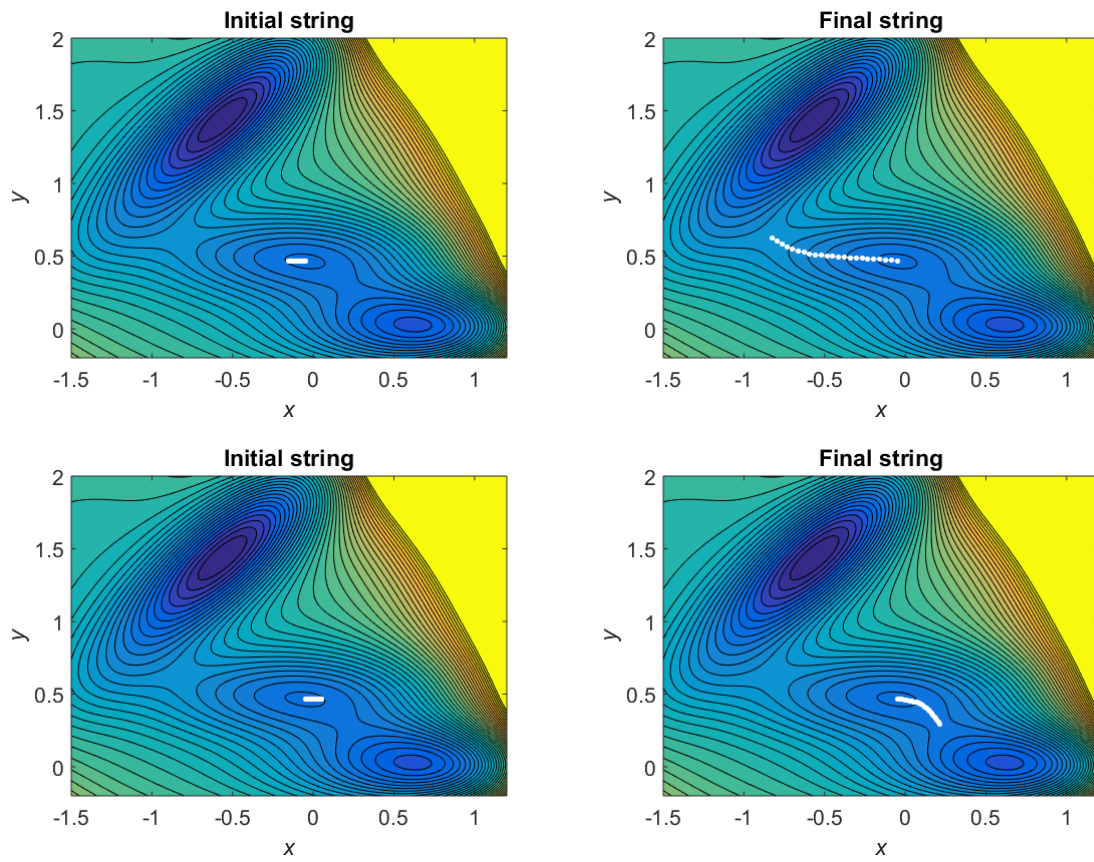
Figure 2.5: The final point of the initial string is given by a small perturbation from the local minimum towards left (upper panel) and right (lower panel). The final point of the string converges to different saddle points at the steady state.

where $V(x)$ is the potential energy, $Z = \int_{R^n} e^{-\beta V(x)} dx$ is the normalizing constant and $\beta = 1/k_B T$ is the inverse of temperature.

We introduce N collective variables $\theta(x) = (\theta_1(x), ..., \theta_N(x))$, which are functions of x and assumed to be good coordinates to describe the system. The free energy $F(z)$ mapped in these collective variables is a function depending on $z = (z_1, ..., z_N)$ defined as

$$F(z) = -\frac{1}{\beta} \times ln \left[Z^{-1} \int_{R^n} e^{-\beta V(x)} \delta(\theta(x) - z) dx \right], \tag{2.9}$$

where $\delta(\cdot)$ is the Dirac delta function.

Before we explain the MFEP, it is useful to recall the MEP defined in the original configuration space. By definition, the MEP is a smooth curve $x(\alpha)$ connecting the two local minima of $V(x)$ and the gradient of potential energy is tangent to the MEP everywhere, i.e.

$$\nabla V(x) \parallel \frac{dx}{d\alpha}. \tag{2.10}$$

Now consider things in the collective variable space. Let $\theta(x(\alpha)) = z(\alpha)$ and $V(x(\alpha)) = F(z(\alpha))$. For the details of replacement of $V(x)$ using $F(z)$, we refer the readers to Ref. [38]. Then by change of variables, we have the following relationship [38]:

$$M(z)\nabla F(z) \parallel \frac{dz}{d\alpha}, \tag{2.11}$$

where $\nabla F(z)$ is the gradient of the free energy and the tensor matrix $M(z)$ denotes the projection from the original configuration space onto the collective variable space. The mathematical formulations of $M(z)$ and $\nabla F(z)$ are given by Eq. 2.13 and 2.14, respectively. The condition given in Eq. 2.11 can be rewritten as

$$(M(z)\nabla F(z))^{\perp} (z(\alpha)) = 0, \tag{2.12}$$

which means that the component of $M(z)\nabla F(z)$ normal to the curve $z(\alpha)$ is zero. The MFEP is defined as the curve $z(\alpha)$ connecting the two local minima of $F(z)$ and satisfying Eq. 2.12. By definition, the MFEP corresponds to the most probable transition pathway between the two local minima on the free energy landscape. The free energy attains the maximum at the saddle point along the MFEP.

The tensor matrix $M(z)$ and the gradient of the free energy $\nabla F(z)$ are computed via a time-averaging approach by restrained molecular dynamics simulations [38] given by

$$M_{ij}(z) = \frac{1}{T} \int_0^T \sum_{k=1}^n \frac{\partial \theta_i(x(t))}{\partial x_k} \frac{\partial \theta_j(x(t))}{\partial x_k} dt, \qquad (2.13)$$

where M_{ij} is the (i, j) entry of tensor matrix $M(z)$ and

$$\frac{\partial F(z)}{\partial z_j} = \frac{\kappa}{T} \int_0^T (z_j - \theta_j(x(t))) \, dt, \qquad (2.14)$$

for κ and T large enough. The restrained molecular dynamics of $x(t)$ constrains the system at $\theta(x) = z$, where $\theta(x)$ is the current value of collective variable and z is the target value. It is realized by adding the restrained potential $\frac{\kappa}{2} \sum_{i=1}^N (z_i - \theta_i(x))^2$ to the Hamiltonian of the original system. For example, the Langevin dynamics with the restrained potential is given by

$$\ddot{x}_k(t) = -\frac{\partial V}{\partial x_k} - \gamma \dot{x}_k(t) + \sqrt{2\gamma k_B T} R_k(t) + \kappa \sum_{i=1}^N (z_i - \theta_i(x)) \frac{\partial \theta_i}{\partial x_k}, \qquad (2.15)$$

for $k = 1, ..., n$ where $R(t) \in \mathbb{R}^n$ is a white noise with $\langle R_i(t), R_j(t') \rangle = \delta_{ij}\delta(t - t')$, $k_B T$ is the temperature and γ is the frictional coefficient.

2.3.2 The Algorithm of String Method in Collective Variables

Suppose the free energy $F(z)$ of the system has two local minima located at z_a and z_b, the string method in collective variables allows one to compute the MFEP connecting z_a and z_b. At the beginning, a string $z(\alpha)$ is constructed connecting the two local minima z_a and z_b, where $\alpha \in [0, 1]$ is for some suitable parametrization such as equal arc length. Then the string is evolved according to the following differential equation:

$$\begin{cases} z_t(\alpha, t) = -\bar{F}(z(\alpha, t)) + \gamma_\alpha \tau_\alpha \text{ for } \alpha \in (0, 1), \\ z(0) = z_a, z(1) = z_b, \end{cases} \qquad (2.16)$$

where $\bar{F}(z) = (M(z)\nabla F(z))^{\perp}$, γ_{α} is a local parameter depending on the parametrization of the curve and $\tau_{\alpha} = \frac{\partial z}{\partial \alpha}/|\frac{\partial z}{\partial \alpha}|$ is the unit tangent vector to the string. The stationary solution of Eq. 2.16 is the MFEP connecting z_a and z_b.

In practice, the differential equation above can be solved by a time-splitting method. Firstly, the string is discretized into $R+1$ images $\{z^0, z^1, ..., z^R\}$ uniformly distributed along the string. Secondly, the discretized string is evolved with a discrete time step Δt according to the mean force $-\bar{F}(z)$. After each step of evolution, we reparametrize the string to enforce equal arc length among the contiguous images.

Algorithm of the string method in collective variables

Let z_n^k be the instantaneous position of the image z^k at the n-th iteration during the string evolution. To update the discretized string at the n-th iteration, we proceed to the following 3 steps:

1. Compute the tensor matrix $M(z_n^k)$ and gradient of the free energy $\nabla F(z_n^k)$, for $k = 1, ..., R - 1$.

2. Move the intermediate images for one time step according to

$$z^{k,*} = z_n^k - \bar{F}(z_n^k)\Delta t \text{ for } k = 1, ..., R - 1, \qquad (2.17)$$

   where $\bar{F}(z) = (M(z)\nabla F(z))^{\perp}$. Let $z^{0,*} = z_a$ and $z^{R,*} = z_b$. Then we end up with a set of new images $\{z^{0,*}, z^{1,*}, ..., z^{R,*}\}$.

3. Interpolate a curve through the images $\{z^{0,*}, ..., z^{R,*}\}$ with a suitable interpolation. Then distribute $R + 1$ new images uniformly along the interpolated curve according to the equal arc length parametrization to obtain the string $\{z_{n+1}^0, z_{n+1}^1, ..., z_{n+1}^R\}$ at the new iteration. Go to step 1 or stop when the string reaches the steady state.

Finally, the discretized string converges to the MFEP connecting z_a and z_b at the steady state. The saddle points and free energy barriers can be obtained from the maximum of the free energy along the MFEP. To further verify the saddle

point indeed describes the transition state, we need to test the committor value distribution at the saddle point. We discuss the concepts of the committor function and isocommittor surface in the next part.

2.3.3 Committor Function and Isocommittor Surface

Consider the molecular dynamics system governed by the Langevin dynamics:

$$
\begin{cases}
\dot{x}_i(t) = v_i(t), \\
\dot{v}_i(t) = -\frac{\partial V(x(t))}{\partial x_i} - \gamma v_i(t) + \sqrt{2\gamma k_B T}\eta_i(t),
\end{cases}
\tag{2.18}
$$

for $i = 1, ..., n$. $x = (x_1, ..., x_n)$ and $v = (v_1, ..., v_n)$ are the positions and velocities of the particles, respectively. γ is the friction coefficient and $\eta_i(t) \in \mathbb{R}^n$ is a white noise with $\langle \eta_i(t), \eta_j(t') \rangle = \delta_{ij}\delta(t - t')$. Assume that the potential energy $V(x)$ has two local minima A and B. The best reaction coordinates to describe the transition between A and B is the committor function $q(x, v)$, which gives the probability that the trajectory solution of Eq. 2.18 initiated at the point (x, v) will reach B first rather than A.

Under the assumption that the collective variables $(\theta_1(x), ..., \theta_N(x))$ are good coordinates to describe the system, we suppose that the committor function $q(x, v)$ can be approximated by a function depending on the collective variables only, i.e.

$$
q(x, v) \approx f(\theta_1(x), ..., \theta_N(x)).
\tag{2.19}
$$

In other words, the committor function can be defined in the collective variable space. Let z_a and z_b be the two local minima on the free energy landscape corresponding to A and B, respectively. The committor function in the collective variable space $f(z)$ describes the probability that the trajectory initiated at z will evolve to z_b first rather than z_a by the steepest descent dynamics, where the mean force $-\nabla F(z)$ is given by Eq. 2.14.

Let $z(\alpha)$, $\alpha \in [0, 1]$ be the MFEP connecting z_a and z_b. At each point along the

MFEP, the isocommittor surface is defined as

$$S(\alpha) = \{z : f(z) = f(z(\alpha))\}, \tag{2.20}$$

on which all the points have the same committor value $f(z(\alpha))$. We are interested in the isocommittor $1/2$ surface, on which the trajectory initiated has equal probability to reach z_a and z_b by the steepest descent dynamics. Thus the isocommittor $1/2$ surface describes the transition region. It is shown in [38] that the isocommittor $1/2$ surface is the isocommittor surface at the saddle point along the MFEP. Suppose $z(\alpha^*)$ is the saddle point along the MFEP, then we have

$$f(z(\alpha)) \approx \begin{cases} 0 & \text{if } \alpha < \alpha^*, \\ 1/2 & \text{if } \alpha = \alpha^*, \\ 1 & \text{if } \alpha > \alpha^*. \end{cases} \tag{2.21}$$

Therefore it is meaningful to determine the saddle point on the free energy landscape, since it is closely related to the transition state and transition region.

If the collective variables are well-chosen, then the saddle point indeed describes the transition state and the isocommittor $1/2$ surface $S(\alpha^*)$ indeed describes the transition region in the original phase space. To further verify the significance of the collective variables, we generate the configurations from the phase space (x, v) which are restricted to $S(\alpha^*)$ with Boltzmann distribution. If the committor values of these configurations are centred around $1/2$, then $S(\alpha^*)$ also corresponds to the isocommittor $1/2$ surface in the phase space (the hypersurface in the original phase space on which the committor function $q(x, v) = 1/2$). The isocommittor $1/2$ surface $S(\alpha^*)$ can be approximated locally by the hyperplane $P(\alpha^*)$, which is tangent to it at the saddle point. So we generate the configurations from the phase space on the hyperplane $P(\alpha^*)$ instead. The configurations x in the phase space restricted to this hyperplane satisfy the following equation:

$$\langle \hat{n}, \theta(x) - z(\alpha^*) \rangle = 0. \tag{2.22}$$

The term $\hat{n}$ is the unit normal vector to the hyperplane given by

$$\hat{n} = \left(M(z(\alpha^*))^{-1} z'(\alpha^*) \right) / \left| M(z(\alpha^*))^{-1} z'(\alpha^*) \right|, \qquad (2.23)$$

where $z'(\alpha^*)$ is the tangent vector to the MFEP at the saddle point. Here we assume the tensor matrix $M(z(\alpha^*))$ is invertible.

In practice, we generate samples of configurations restricted to the hyperplane $P(\alpha^*)$ by adding the following additional potential to the Hamiltonian of the original system:

$$V_{\kappa,\alpha^*} = \frac{\kappa}{2} \left\langle \hat{n}, \theta(x) - z(\alpha^*) \right\rangle^2. \qquad (2.24)$$

The committor function of each sample is computed from sampling trajectories generated from each sample by assigning random initial velocities. The committor value is given by the probability that the trajectory will reach B first rather than A. If the committor values of these samples are centred around $1/2$, then the saddle point indeed describes the transition state and $P(\alpha^*)$ approximates the isocommittor $1/2$ surface, thus describes the transition region.

2.4 The Climbing String Method in Collective Variables

We extend the string method in collective variables to the climbing string method in collective variables focusing on the study of saddle points on the free energy landscape. Suppose the free energy of the system $F(z)$ has a local minimum z_a. The new method allows us to compute the saddle point directly connected to z_a and half of the MFEP connecting z_a and the saddle point.

For the implementation of the new method, an initial string $z(\alpha)$, $\alpha \in [0,1]$ is constructed in the collective variable space with one end point fixed at the local minimum z_a. The other end point is defined by a small perturbation from the local minimum z_a, denoted as z_p. Let $z(\alpha, t)$ be the instantaneous position of the string at

time t during the string evolution. The string is evolved according to the following differential equation:

$$
\begin{cases}
z_t(\alpha, t) = -\bar{F}(z(\alpha)) + \gamma_\alpha \tau_\alpha \text{ for } \alpha \in (0, 1), \\
z_t(1, t) = -\bar{F}(z(1)) + 2 \left\langle \bar{F}(z(1)), \tau_1 \right\rangle \tau_1, \\
z(0, t) = z_a, \ z(1, 0) = z_p,
\end{cases}
\tag{2.25}
$$

where the terms γ_α, τ_α were defined previously in the string method in collective variables, and $\bar{F}(z(\alpha)) = M(z(\alpha))\nabla F(z(\alpha))$. The stationary solution of the differential equation is the string connecting z_a and a point z^* with $M(z^*)\nabla F(z^*) = 0$. If $M(z^*)$ is invertible, then $\nabla F(z^*) = 0$ and z^* is the saddle point. Thus the final point of the string converges to the saddle point if $M(z)$ is an invertible matrix for all z.

In practice, the differential equation 2.25 can be solved using a time-splitting method. Firstly, the string is discretized into $R+1$ images $\{z^0, z^1, ..., z^R\}$ uniformly distributed along the string. The discretized string is evolved using a discrete time step Δt. The first image z^0 is fixed at z_a. The intermediate images $z^1, ..., z^{R-1}$ are moved according to the mean force $-\bar{F}(z)$. The end image z^R is moved according to the second equation in Eq. 2.25, solved using the forward Euler method. After each step of evolution, we reparametrize the string to enforce equal arc length among the contiguous images.

Algorithm of the climbing string method in collective variables

Let z_n^k be the instantaneous position of the image z^k at the n-th iteration during the string evolution. To update the discretized string at the n-th iteration, we proceed to the following 3 steps:

1. Compute the gradient of free energy $\nabla F(z_n^k)$ and the tensor matrix $M(z_n^k)$, for $k = 1, ..., R$.

2. The first image is fixed at z_a, $z^{0,*} = z_a$. The intermediate images are moved

for one time step according to

$$z^{k,*} = z_n^k - \bar{F}(z_n^k)\Delta t, \text{ for } k = 1, ..., R - 1, \tag{2.26}$$

and the last image is moved for one time step according to

$$z^{R,*} = z_n^R - \left[\bar{F}(z_n^R) - 2\left\langle\bar{F}(z_n^R), \tau_1\right\rangle\tau_1\right]\Delta t, \tag{2.27}$$

where $\bar{F}(z) = M(z)\nabla F(z)$. We end up with a set of new images $\{z^{0,*}, ..., z^{R,*}\}$.

3. Interpolate a curve through the images $\{z^{0,*}, ..., z^{R,*}\}$ with a suitable interpolation. Then distribute $R + 1$ new images uniformly along the interpolated curve according to the equal arc length parametrization to obtain the string $\{z_{n+1}^0, z_{n+1}^1, ..., z_{n+1}^R\}$ at the new iteration. Go to step 1 or stop when the string reaches the steady state.

Given $M(z)$ is an invertible matrix for all z, when the string reaches the steady state, the end image z^R converges to the saddle point on the free energy landscape. An invertible matrix $M(z)$ is a compulsory condition for the implementation of the climbing string method in collective variables.

This new method has some advantages over the string method in collective variables. In the new method, we only need one local minimum on free energy landscape. This is important especially when only one local minimum is known in priori. The other advantage is the same as the climbing string method. The saddle point can be more accurately located using the climbing string method when the saddle point is close to one local minimum and very far away from another local minimum.

2.5 The On-the-fly String Method

A simplified and improved version of the string method in collective variables was proposed by Maragliano and Vanden-Eijnden [39], named on-the-fly string method. The new method avoids the computation of mean force at each step of the string

evolution. It has been shown to be more efficient and stable comparing with the original method. For the rest of this chapter, firstly we recall the on-the-fly string method. Secondly, we apply the techniques of 'on-the-fly' computation to modify the climbing string method in collective variables and develop the on-the-fly climbing string method. Finally, we apply the on-the-fly climbing string method to study the conformational change of alanine dipeptide, which is a joint work with my colleague Guo. The transition pathway and transition state are determined, which are consistent with Ref. [38].

Suppose the free energy $F(z)$ of the system has two local minima z_a and z_b. We look for the MFEP connecting z_a and z_b. For the implementation of the on-the-fly string method, an initial string $z(\alpha)$, $\alpha \in [0,1]$ is constructed connecting the two local minima z_a and z_b, where α is for some suitable parametrization such as equal arc length. The string is discretized into $R + 1$ images $\{z^0, z^1, ..., z^R\}$ uniformly distributed along the string. Each image z^k is assigned a molecular dynamics (MD) replica x^k constrained at $\theta(x^k) = z^k$. During the string evolution, the MD replicas are evolved concurrently with the discretized string using restrained molecular dynamics. The evolution of the string is artificially slowed down so that the MD replicas have enough time to equilibrate themselves and provide on-the-fly the data to evolve the string.

Algorithm of the on-the-fly string method

Let z_m^k and x_m^k be the instantaneous position of image z^k and MD replica x^k at the m-th iteration during the string evolution. To update z_m^k and x_m^k at the m-th iteration, we proceed to the following 2 steps:

1. Concerted evolution of the images and the MD replicas for one time step Δt

according to:

$$
\begin{cases}
z^{0,*} = z_a, \\[2mm]
z^{R,*} = z_b, \\[2mm]
z^{k,*} = z_m^k - \Delta t \frac{\kappa}{\gamma_z} \tilde{M}(x_m^k) \left(z_m^k - \theta(x_m^k) \right), \\[2mm]
x_{m+1}^k = \text{ run the restrained molecular dynamics for one time step} \\[2mm]
\Delta t \text{ with the restrained potential } \frac{\kappa}{2}|\theta(x_m^k) - z_m^k|^2,
\end{cases}
\tag{2.28}
$$

for $k = 1, ..., R - 1$, where the (i, j) entry of the tensor matrix $\tilde{M}(x)$ is given by

$$
\tilde{M}_{ij}(x) = \sum_{l=1}^{n} \frac{\partial \theta_i(x)}{\partial x_l} \frac{\partial \theta_j(x)}{\partial x_l}.
\tag{2.29}
$$

We end up with a set of new images $\{z^{0,*}, ..., z^{R,*}\}$.

2. Interpolate a curve through the images $\{z^{0,*}, ..., z^{R,*}\}$ with a suitable interpolation. Then distribute $R + 1$ new images uniformly along the interpolated curve according to the equal arc length parametrization to obtain the string $\{z_{m+1}^0, z_{m+1}^1, ..., z_{m+1}^R\}$ at the new iteration. Go to step 1 or stop when the string reaches the steady state.

In the algorithm above, $\kappa > 0$ should be chosen large so that the MD replica x^k is well constrained at $\theta(x^k) = z^k$. γ_z is chosen large to artificially slow down the string evolution, such that the MD replicas have enough time to equilibrate themselves and provide the data on-the-fly for the string evolution. The string converges to the MFEP connecting the local minima z_a and z_b at the steady state.

2.6   The On-the-fly Climbing String Method

Suppose the free energy $F(z)$ of the system has a local minimum z_a. We look for the saddle points directly connected to z_a. We apply the techniques of 'on-the-fly' computation to modify the climbing string method in collective variables and

develop the on-the-fly climbing string method. For the implementation, an initial string $z(\alpha)$, $\alpha \in [0, 1]$ is constructed with one end point fixed at z_a. The other end point is defined by a small perturbation of z_a, denoted as z_p. The string is discretized into $R + 1$ images $\{z^0, z^1, ..., z^R\}$ uniformly distributed along the string. Each image z^k is assigned an MD replica x^k constrained at $\theta(x^k) = z^k$.

Algorithm of the on-the-fly climbing string method

Let z_m^k and x_m^k be the instantaneous position of the image z^k and the MD replica x^k at the m-th iteration during the string evolution. To update z_m^k and x_m^k at the m-th iteration, we proceed to the following 2 steps:

1. Concerted evolution of the images and the MD replicas for one time step Δt according to:

$$
\begin{cases}
z^{0,*} = z_a, \\
z^{k,*} = z_m^k - \Delta t \frac{\kappa}{\gamma_z} \bar{F}(z_m^k, x_m^k) \text{ for } k = 1, ..., R-1, \\
z^{R,*} = z_m^R - \Delta t \frac{\kappa}{\gamma_z} \left[\bar{F}(z_m^R, x_m^R) - 2 \left\langle \bar{F}(z_m^R, x_m^R), \hat{\tau} \right\rangle \hat{\tau} \right], \\
x_{m+1}^k = \text{run the restrained molecular dynamics for one time step} \\
\Delta t \text{ with the restrained potential } \frac{\kappa}{2} |\theta(x_n^k) - z_n^k|^2, \text{ for } k = 1, ..., R,
\end{cases}
\tag{2.30}
$$

where $\bar{F}(z_m^k, x_m^k) = \tilde{M}(x_m^k) \left(z_m^k - \theta(x_m^k) \right)$, $\hat{\tau} = \frac{z_m^R - z_m^{R-1}}{|z_m^R - z_m^{R-1}|}$ is the unit tangent vector to the string at z_m^R. The matrix $\tilde{M}(x)$ is defined previously in the on-the-fly string method. We end up with a set of new images $\{z^{0,*}, ..., z^{R,*}\}$.

2. Interpolate a curve through the images $\{z^{0,*}, ..., z^{R,*}\}$ with a suitable interpolation. Then distribute $R + 1$ new images uniformly along the interpolated curve according to the equal arc length parametrization to obtain the string $\{z_{m+1}^0, z_{m+1}^1, ..., z_{m+1}^R\}$ at the new iteration. Go to step 1 or stop when the string reaches the steady state.

The string converges to half of the MFEP connecting the saddle point and the local minimum z_a at the steady state.
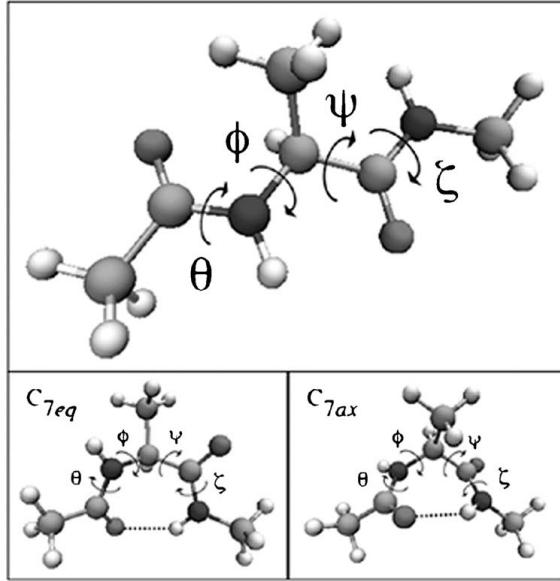
Figure 2.6: Ball-stick presentation of alanine dipeptide and dihedral angles. In the lower panel, two metastable conformers C_{7eq} and C_{7ax} are characterized by the dihedral angles. The picture is from Ref. [38].

2.7 Application to Conformational Change of Alanine Dipeptide

We use the conformational change of alanine dipeptide as a simple example to test the on-the-fly climbing string method. The two metastable conformers C_{7eq} and C_{7ax} are usually characterized by the dihedral angles $(\theta, \phi, \psi, \zeta)$ as shown in Fig. 2.6. The conformational change between C_{7eq} and C_{7ax} is studied using the string method in collective variables by Maragliano, Vanden-Eijnden [38]. In Fig. 2.7, the MFEP is given by the gray curve connecting C_{7eq} (top left) and C_{7ax} (bottom right), using (ϕ, ψ) as the collective variables.

For the implementation of the on-the-fly climbing string method, we start from the conformer C_{7eq}. We look for the saddle point in the collective variable space (ϕ, ψ) directly connected to C_{7eq}. We use $\Delta t = 0.0002, \kappa = 100, \gamma_z = 5000$ in the computation. Our numerical result is shown in Fig. 2.8. An initial string (yellow circles) is constructed with one end point fixed at C_{7eq} and the other end point is
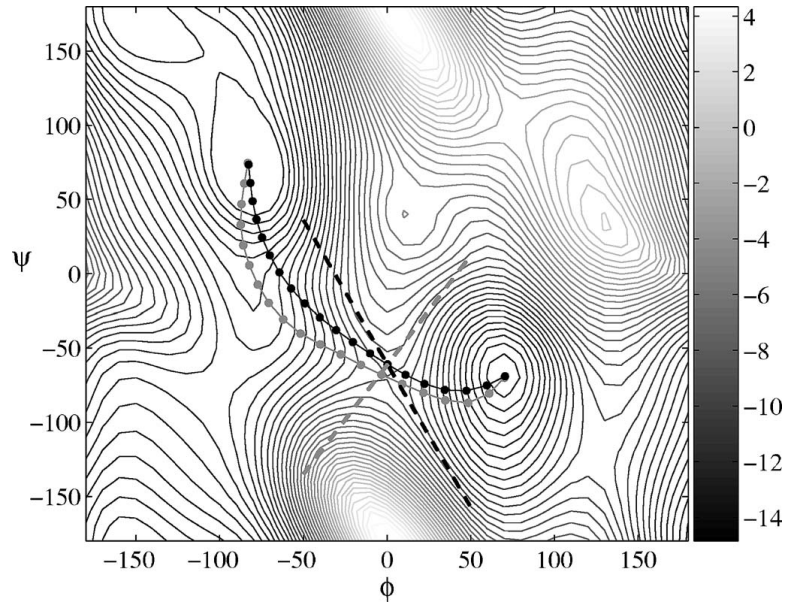
Figure 2.7: Minimum free energy path computed using the string method in collective variables with the collective variables (ϕ, ψ) (grey curve) and $(\phi, \psi, \theta, \zeta)$ (black curve). The latter is the projection in the space (ϕ, ψ). The picture is from Ref. [38].

defined by a small perturbation of C_{7eq} towards bottom right. The string converges to half of the MFEP connecting the local minimum and saddle point (red squares) at the steady state. During the simulation, we allow the starting point of the string to fluctuate around the local minimum C_{7eq}. Our result is consistent with Ref. [38].
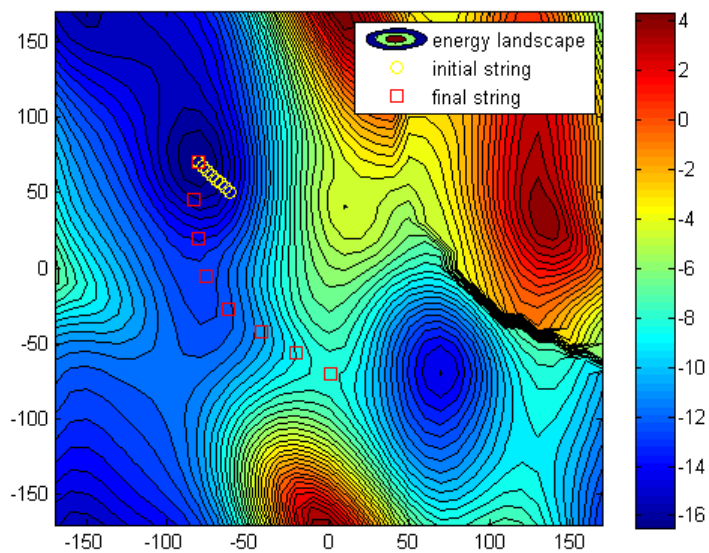
Figure 2.8: Initial string (yellow circles) converges to the MFEP connecting the local minimum and saddle point (red squares) using the on-the-fly climbing string method. During the string evolution, we allow the starting point of the string to fluctuate around the local minimum.

Numerical Study of Vapor Condensation on Hydrophobic Surfaces Patterned with Microstructures

In this chapter, we numerically study the problem of vapor condensation on hydrophobic surfaces patterned with microstructures using a phase field model [34]. The critical nuclei, the activation energy barriers and the minimum energy paths (MEP) are accurately determined using the climbing string method. The effects of pillar height, interpillar spacing, supersaturation level and intrinsic wettability of solid surface on nucleation process are investigated. The critical values of pillar height, interpillar spacing and supersaturation level at which the critical nucleus changes from the Cassie state to the Wenzel state are determined from the phase diagram. Furthermore, the growth of the vapor condensate towards the liquid phase after passing the critical nucleus is computed using the steepest descent dynamics.

In section 3.1, we introduce the phase field model, which uses the density field to model the two-phase fluid on a solid substrate. The potential energy of the system is expressed as a functional of the density field.

In section 3.2, we describe the numerical scheme and the implementation of the
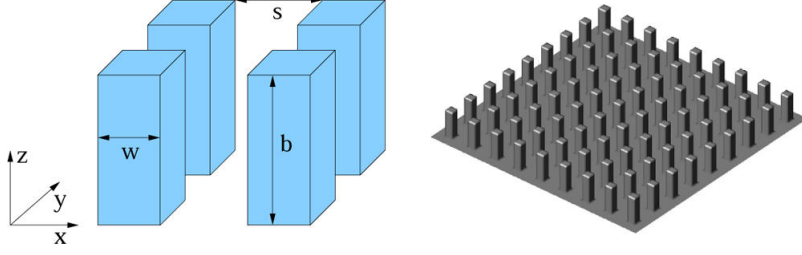
Figure 3.1: Solid substrate with a square lattice of rectangular pillars. The pillar has a square cross section with width w and height b. The interpillar spacing is denoted by s.

climbing string method to search the saddle points, which correspond to the critical nuclei formed during the vapor condensation. At the same time, we determine the MEP connecting the local minimum and the saddle point, which describes the most probable pathway for the formation of the critical nucleus from the vapor phase.

In section 3.3, we present the numerical results of the critical nuclei, energy barriers and MEP. It is observed that the critical nucleus exhibits either the Cassie state or the Wenzel state. The effects of the pillar height, interpillar spacing, supersaturation level and the intrinsic wettability of the solid surface on the nucleation process are reported. The phase diagram of the critical nuclei with respect to the pillar height, interpillar spacing and the supersaturation level are systematically investigated.

3.1 Mathematical Model

The system in our study consists of the two-phase fluid and a solid substrate. The solid surface is patterned with a square lattice of rectangular pillars as shown in Fig. 3.1. The width, height of pillars and interpillar spacing are denoted by w, b and s respectively. The coexistence of the liquid and vapor phases is modelled by a diffuse interface model. In the model, the density of the fluids is represented by a function $\phi(x)$ and the grand potential is given by

$$G(\phi) = \int_\Omega \frac{\kappa}{2} |\nabla \phi(x)|^2 + f(\phi(x)) - \mu \phi(x) dx, \qquad (3.1)$$

where Ω is the physical domain occupied by the fluids. In the above integral, the first term measures the excess free energy density associated with the inhomogeneity of the fluid, function $f(\phi)$ is the energy density for the homogeneous phase, μ is the supersaturation (or chemical potential measured by liquid-vapor coexistence). The function $f(\phi)$ takes the form of a double well potential given by

$$f(\phi) = \frac{\beta}{2}\phi^2(1-\phi)^2. \tag{3.2}$$

The two minima of $f(\phi)$ correspond to the two fluid phases: $\phi = 1$ for the liquid phase and $\phi = 0$ for the vapor phase. The thickness d of the liquid-vapor interface is determined by the parameters κ and β: $d \propto (\kappa/\beta)^{1/2}$. In our study, we use $\kappa = 10^{-4}$ and $\beta = 1$. The system is biased by the supersaturation μ, one of liquid or vapor phase becomes meta-stable or even unstable depending on the value of μ. In particular, the binodal (liquid-vapor coexistence) and spinodal (the boundary of metastability) points for homogeneous bulk phase are given by $\mu = 0$ and $\mu^\pm = \pm\sqrt{3}\beta/18$, respectively. A positive value of μ biases the system towards the liquid phase, and a negative value of μ biases the system towards the vapor phase.

The boundary condition at the solid wall determines the wettability of the solid surface. We apply the Dirichlet boundary condition on the solid wall [6]:

$$\phi = \phi_s. \tag{3.3}$$

Various wettabilities of the solid surface can be realized by changing the value of ϕ_s from 0 to 1, where $\phi_s = 0$ corresponds to a nonwetting surface and $\phi_s = 1$ corresponds to a complete wetting surface. With this boundary condition, we may observe a transition layer between the bulk fluids and the solid surface as shown in Fig. 3.2. The equilibrium contact angle θ is related to ϕ_s (at $\mu = 0$) given by

$$\cos\theta = -1 + 6\phi_s^2 - 4\phi_s^3. \tag{3.4}$$

For example, $\phi_s = 0.4$ corresponds to the equilibrium contact angle $125°$ for a liquid droplet on a flat solid surface. We use periodic conditions in the direction parallel
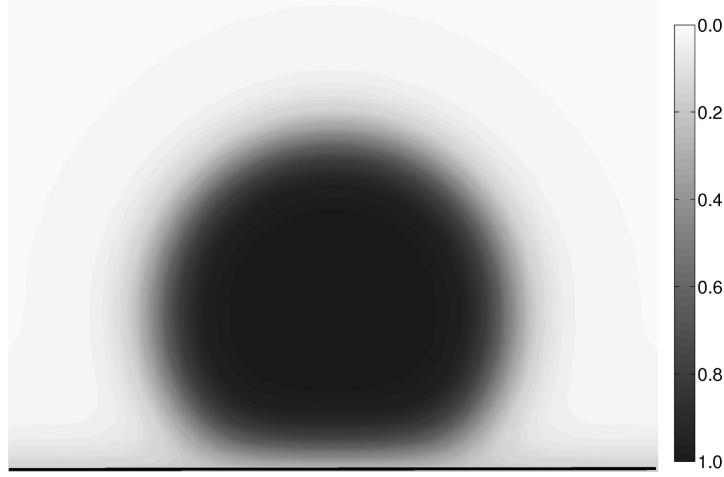
Figure 3.2: The side view of a critical nucleus on a flat solid surface. Supersaturation $\mu = 0.03$, boundary condition $\phi_s = 0.2$. The grey scale is the density of fluid from one (black) to zero (white).

to the solid wall. Since we study the vapor nucleation over the solid surface, we assume the fluids are in the vapor phase in the far field. Therefore we set $\phi = 0$ at the upper boundary of the computational domain. The minima and saddle points of the grand potential correspond to the metastable states and transition states, respectively. These are the critical points of G. They satisfy the Euler-Lagrange equation given by

$$-\frac{\delta G}{\delta \phi} = \kappa \nabla^2 \phi - \beta \phi(\phi - 1)(2\phi - 1) + \mu = 0. \tag{3.5}$$

The minima of the grand potential can be computed by solving the steepest descent dynamics given by

$$\frac{\partial \phi}{\partial t} = \kappa \nabla^2 \phi - \beta \phi(\phi - 1)(2\phi - 1) + \mu, \tag{3.6}$$

with the boundary conditions above and a suitable initial state. We choose supersaturation not too large $0 < \mu < \mu^+$ such that vapor phase is a metastable state. In the vapor phase, the density ϕ is zero almost everywhere except a small deviation near the solid wall due to the boundary condition $\phi = \phi_s$.

The saddle points of the grand potential connected to the vapor phase correspond to the critical nuclei formed during the vapor condensation. We search these saddle
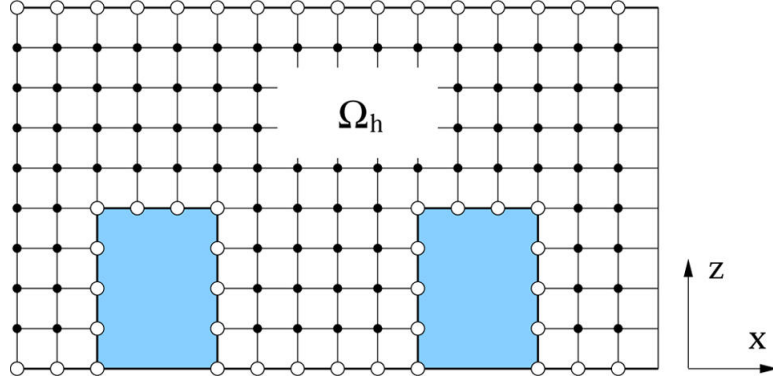
Figure 3.3: Illustration of meshed computational domain. The density field is computed on the black dots. On the open circles, the density field is given by the boundary condition ϕ_s.

points using the climbing string method.

3.2 Numerical Methods

We divide the problem into two steps. Firstly, starting from the vapor phase which is a minimum of the grand potential, we search the saddle points (critical nuclei) connected to the vapor minimum using the climbing string method. It also gives us the MEP connecting the vapor phase and the saddle points, which corresponds to the pathway for the formation of the critical nuclei from the vapor phase. Secondly, after the critical nucleus is computed, the subsequent growth of the vapor condensate towards the liquid phase is computed by solving the steepest descent dynamics given by Eq. 3.6.

The computational domain is discretized using a uniform mesh with equal step size h in x,y,z directions. The mesh grid from a side view is illustrated from Fig. 3.3. The grid points $\{x_i, y_j, z_k\}$ in the interior of the computational domain (black dots) are denoted by Ω_h. Let $\phi_{i,j,k}$ denote the phase field function at the grid point (x_i, y_j, z_k). The integral in the grand potential are approximated using the midpoint numerical quadrature. The spatial derivatives are approximated using centered finite

difference. For example, $\frac{\partial \phi}{\partial x}$ at the midgrid point $(x_{i+1/2}, y_j, z_k)$ is approximated by

$$\frac{\partial \phi}{\partial x} = \frac{1}{h}(\phi_{i+1,j,k} - \phi_{i,j,k}), \tag{3.7}$$

and similarly for other derivatives. After discretization, the grand potential $G(\phi)$ can be approximated by $G_h(\phi_h)$, where ϕ_h is a long vector consisting of all the unknowns $\{\phi_{i,j,k}\}$ for $(x_i, y_j, z_k) \in \Omega_h$. With abuse of notation, we remove the subscript h and simply use G to represent the discretized potential and ϕ to represent the long vector.

For the discretized grand potential $G(\phi)$, we use the climbing string method to search the saddle points around the minimum which corresponds to the vapor phase and the MEP connecting the minimum and the saddle points. This is done by evolving a string φ in the d-dimensional configuration space, where d is the length of vector ϕ. The string φ is a curve in the configuration space which is parametrized by its normalizing arc length α. The string is evolved according to the following fictitious dynamics:

$$\frac{\partial \varphi}{\partial t}(\alpha, t) = -\nabla G(\varphi) + \lambda \hat{\tau}, \quad \text{for } 0 < \alpha < 1, \tag{3.8}$$

with boundary conditions

$$\varphi(\alpha, t) = a, \text{ at } \alpha = 0, \tag{3.9}$$

and

$$\frac{\partial \varphi}{\partial t}(\alpha, t) = -\nabla G(\varphi) + 2 \langle \nabla G, \hat{\tau} \rangle \hat{\tau}, \text{ at } \alpha = 1, \tag{3.10}$$

where $\hat{\tau} = \frac{\partial_\alpha \varphi}{|\partial_\alpha \varphi|}$ is the unit tangent vector to the string, λ is the Lagrangian multiplier associated with the equal arc length parametrization. In the above equations, the potential force $-\nabla G$ is given by Eq. 3.5 after the discretization of the spatial derivatives using the centered finite difference.

The evolution of the two end points are governed by Eq. 3.9 and 3.10. During the string evolution, the initial point of the string $\varphi(0)$ is fixed at the local minimum a (the vapor phase). The final point of the string $\varphi(1)$ will climb uphill towards the saddle point on the energy landscape.

Starting from a suitable initial string, the above equations are solved until the string reaches the steady state. In the computation, the string is discretized into $N + 1$ images denoted by $\{\phi_0^k, \phi_1^k, ..., \phi_N^k\}$, where ϕ_l^k is the image at $\alpha_l = l/N$ for $l = 0, 1, ..., N$ and at the time $t_k = k\Delta t$ with Δt being the time step; ϕ_0^k and ϕ_N^k are the initial image and the end image along the string respectively. After the discretization of the string, the above equations can be solved using a time-splitting scheme as follows:

1. Evolve the images for one time step using forward Euler method according to

$$\begin{cases} \phi_0^* = \phi_0^k, \\ \phi_l^* = \phi_l^k - \nabla G(\phi_l^k)\Delta t, \quad \text{for } l = 1, ..., N-1, \\ \phi_N^* = \phi_N^k - \left(\nabla G(\phi_N^k) - 2\left\langle \nabla G(\phi_N^k), \hat{\tau}_N \right\rangle \hat{\tau}_N\right)\Delta t, \end{cases} \tag{3.11}$$

   where $\hat{\tau}_N = \frac{\phi_N^k - \phi_{N-1}^k}{|\phi_N^k - \phi_{N-1}^k|}$ is the unit tangent vector of the string at the end image ϕ_N^k.

2. Interpolate a curve through the images $\{\phi_0^*, ..., \phi_N^*\}$ with a suitable interpolation, for example the piecewise linear interpolation. Then distribute $N + 1$ new images uniformly along the interpolated curve according to the equal arc length parametrization to obtain the string $\{\phi_0^{k+1}, ..., \phi_N^{k+1}\}$ at the new time step. Go to step 1 or stop when the string reaches the steady state.

At the steady state, the end image of the string ϕ_N converges to the saddle point of the grand potential $G(\phi)$, which corresponds to the critical nucleus formed during the vapor condensation. The string represented by $\{\phi_0, ..., \phi_N\}$ converges to the MEP connecting the minimum and the saddle point. The MEP describes the most probable pathway for the formation of the critical nucleus from the vapor phase. Further growth of the nucleus towards the liquid phase is spontaneous after passing the saddle point. The relaxation dynamics is computed by solving the steepest descent dynamics given in Eq. 3.6, with a perturbed saddle point as the

initial condition. Specifically, the saddle point is perturbed in the unstable direction given by the MEP: $\phi^{init} = \phi_N + \epsilon\hat{\tau}_N$, where ϵ is small and $\hat{\tau}_N = \frac{\phi_N - \phi_{N-1}}{|\phi_N - \phi_{N-1}|}$ is the unit tangent vector to the MEP at the saddle point. In our computation, the steepest descent dynamics is solved using the forward Euler method and the spatial derivative in Eq. 3.6 are discretized using the centered finite difference.

3.3 Results and Discussion

In our simulation, the grid size of the mesh covering the computational domain is h=0.01, the pillar width is fixed at w=0.04, and the parameters in the grand potential is fixed at $\kappa = 10^{-4}$, $\beta = 1$. The string is discretized into $N + 1 = 11$ images, including the two end points. Unless otherwise specified, the boundary condition over the solid wall is fixed at $\phi_s = 0.3$. Other parameters like the pillar height b, interpillar spacing s and supersaturation level μ are specified later during the discussion.

To construct the initial string, we make a small perturbation on the minima of the grand potential (the vapor phase) and then connect the minima and this perturbed state with a straight string. Specifically, we increase the density of one particular grid point by 0.01 while keeping the density unchanged at other grid points. The grid point where the density is increased plays a role as a nucleation seed. It is chosen either near the top of the pillar or near the bottom of the groove. The former choice makes the condensate preferentially converges to the Cassie state, whereas the latter choice makes it preferentially converges to the Wenzel state. On a complex energy landscape, many different saddle points connected to the given minima may coexist. The saddle point computed using the climbing string method strongly depends on the choice of the initial perturbation. It is possible that some saddle points (especially those with high energy barrier) cannot be found using this procedure due to the lack of knowledge about the saddle point.

To illustrate the diffuse interface model, firstly we compute the critical nucleus

for the heterogeneous nucleation on the flat solid wall using the climbing string method. In Fig. 3.2, it is observed that a fluid bulk is formed on the flat solid surface. There exists a boundary layer between the liquid bulk and the bottom solid surface due to the Dirichlet boundary condition on the solid wall; this is similar to the transition layer between the liquid phase and the vapor phase. The width of boundary/transition layer depends on the parameters κ and β in the integral of the grand potential: $d \propto (\kappa/\beta)^{1/2}$. The energy barrier at the critical nucleus is 7.66×10^{-5} for heterogeneous nucleation. We also compute the critical nucleus for the homogeneous nucleation using climbing string method. A spherical critical nucleus is formed, where the energy barrier is 8.21×10^{-5}. We see that the presence of the solid surface lowers the activation energy barrier, thus enhances the nucleation process.

Typical nucleation scenario

For nucleation over the pillared surface, typical nucleation scenarios are shown in Fig. 3.4. The images in each row are a snapshot along the MEP: one before the formation of critical nucleus, the critical nucleus (second image), the subsequent growth of vapor condensate towards the liquid phase after passing the saddle point (the last two images). We make several observations from the numerical results. In case of narrow interpillar spacing (case a and b), the nucleation starts near the top of the pillars. The critical nucleus formed is in the Cassie state, where the droplet sits on the top of the pillars with air trapped in the grooves. In case of wide interpillar spacing (case c,d and e), the nucleations starts at the bottom of the groove. The critical nucleus formed is in the Wenzel state and the grooves are filled with liquid. Moreover, it is observed that the critical nucleus can be also formed on top of a single pillar (not shown), especially when interpillar spacing is wide. However, the energy barrier of this type of nucleation is usually large due to the small contact area between the critical nucleus and the pillars.

The second observation we make from Fig. 3.4 is that at some intermediate interpillar spacings (case c), the nucleation starts at the bottom of the groove, but
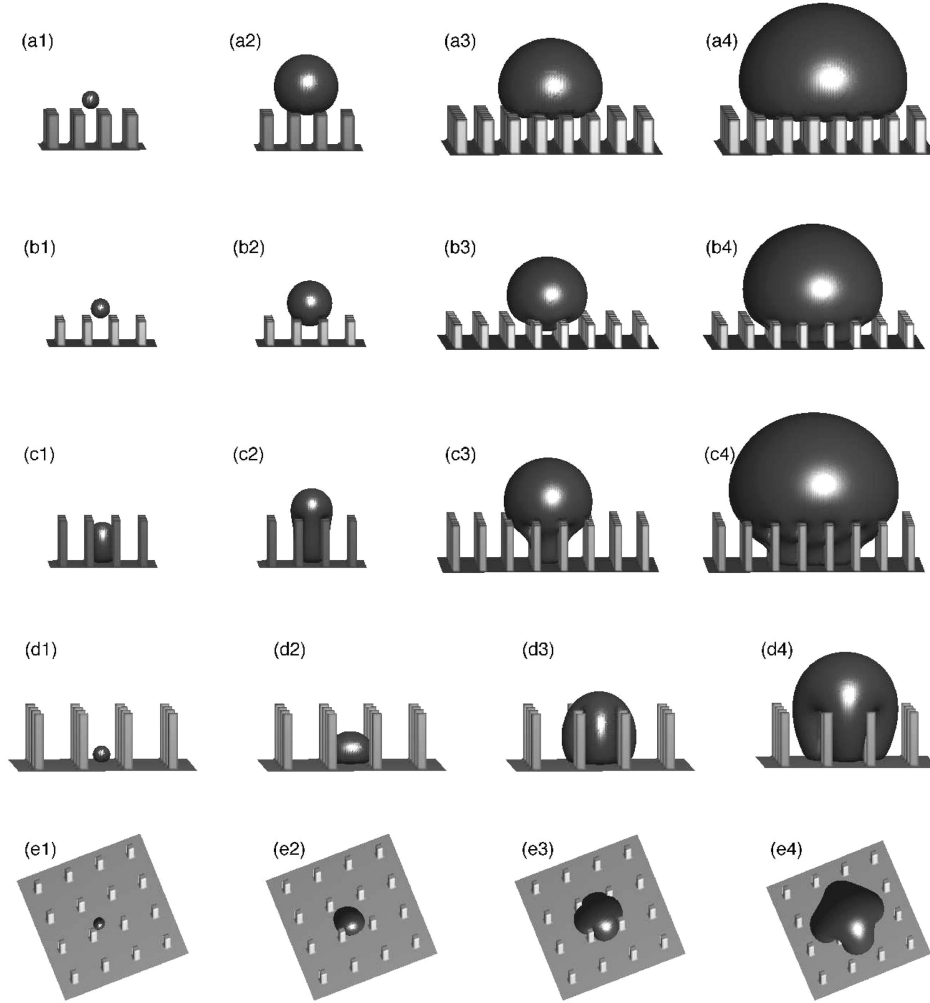
Figure 3.4: Snapshot along the MEP for the formation and subsequent growth of critical nucleus. The four images in each row represent one MEP. Images labelled by a2,b2,c3,d2 and e2 are the critical nuclei. The supersaturation level $\mu = 0.03$. The interpillar spacing and height of pillars are (a) s=0.05, b=0.12; (b) s=0.09, b=0.12; (c) s=0.10, b=0.24; (d) s=0.15, b=0.24; (e) s=0.19, b=0.24, from top to bottom respectively. The droplet is represented by isosurface of $\phi = 0.5$. The images in different rows are not of the same scale.

the nucleus grows all the way up to the top of the pillars. The critical nucleus has features of both the Cassie and Wenzel states. On one hand, a liquid droplet is formed on the top of the pillars similar to the Cassie state. On the other hand, the grooves are filled with liquid similar to the Wenzel state. It is interesting to note that when the interpillar spacing is further increase by 0.01, which is just one grid size, the critical nucleus suddenly changes to a much smaller droplet and fall completely into the groove (not shown, but similar to case d). When the interpillar spacing becomes even wider, the nucleation starts near the bottom. The critical nucleus becomes asymmetric, which touches only one pillar (case e).

The subsequent growth of the vapor condensate after passing the saddle point is shown in the last two columns in Fig. 3.4. In case of very narrow interpillar spacing (case a), the critical nucleus initiated at the Cassie state will still be in the Cassie state when it grows further. The critical nucleus initiated at the Cassie state may evolve to the Wenzel state, when the interpillar spacing is not narrow enough (case b). During its growth after passing the saddle point, the liquid droplet gradually fills in the grooves and the Wenzel state is formed. In case of wide interpillar spacing (case c,d and e), the critical nucleus initiated at the Wenzel state will still be in the Wenzel state as it grows further. The Cassie-to-Wenzel transition is observed in the relaxation stage when the interpillar spacing is relatively wide (but still narrow so that the critical nucleus is in the Cassie state). But the Wenzel-to-Cassie transition is never observed in our computation. An activation energy is needed for a liquid droplet in the Wenzel state to evolve to the Cassie state, since the Wenzel state is more preferred energetically due to the contact with the solid wall.

The grand potential associated with Fig. 3.4 is shown in Fig. 3.5. The maxima along each curve correspond to the saddle points of the grand potential (i.e. critical nuclei). For each curve, the MEP from the minima to the saddle is computed using the climbing string method; the path after passing the saddle point is computed by solving the steepest descent dynamics given by Eq. 3.6 and then reparametrized by the normalized arc length α. Notice that the points on the right end do not
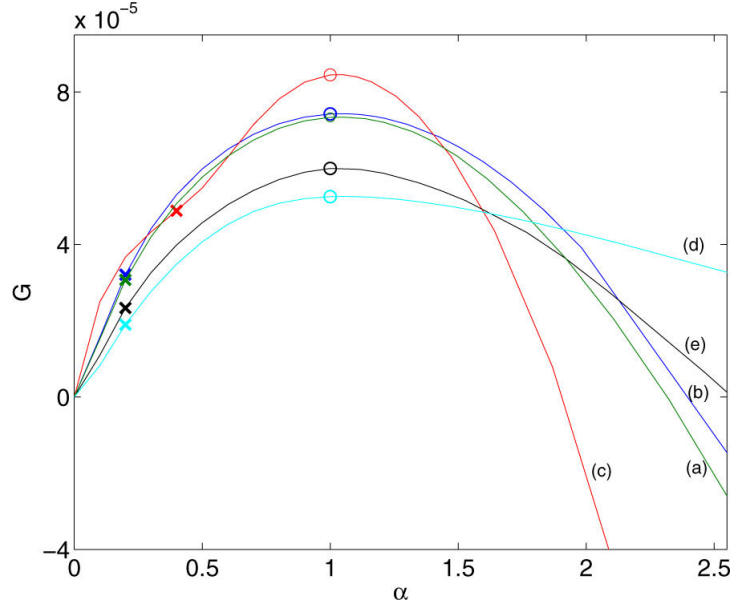
Figure 3.5: (Shift) potential along MEPs in Fig. 3.4. The points marked by cross correspond to the images on the first column. The points marked by open circle correspond to the second column (critical nuclei). The critical nuclei has the highest grand potential along MEP.

correspond to the minima. The grand potential will further decrease, as the system continues to evolve towards the liquid phase.

Phase diagram on s-b plane and energy barrier

The phase diagram of the critical nucleus on the plane of the interpillar spacing s and the pillar height b is shown in Fig. 3.6. At the fixed height, the activation energy barrier increases in region I (circles) and III (squares) and decrease in region II (triangles). In region I and III, the critical nucleus is in the Cassie state and the Wenzel state respectively. In region II, the critical nucleus has features of both the Cassie and Wenzel states. Typical configurations of the three states are shown in the lower panel of Fig. 3.6. From the phase diagram, we observe that the type of critical nucleus formed is more sensitive to the interpillar spacing s and less sensitive to the pillar height b. In particular, the critical nucleus always exhibits the Cassie state for narrow interpillar spacing $s = 0.03, 0.04$ and the Wenzel state for wide interpillar spacing $s = 0.11, 0.12$.

The energy barrier for nucleation are shown in Fig. 3.7. In the upper panel, the energy barrier is plotted against the interpillar spacing s, at fixed pillar height $b = 0.07$ (left) and 0.12 (right), respectively. The activation energy barrier increases with s in the regions indicated by circles (Cassie state) and squares (Wenzel state). This is due to the decrease of the contact area between the critical nucleus and the solid wall. In the intermediate region indicated by triangles (region II), the energy barrier decreases with s. This is due to the relaxation of the confinement of the critical nucleus by the pillars. We also observed that different type of critical nuclei may coexist at certain value of the interpillar spacing. For example, at b=0.12 and s=0.07, we obtained two critical nuclei, one in the Cassie state and the other in the Wenzel state. The former case is obtained from an initial perturbation near the top of the pillar; while the latter case is obtained from the initial perturbation near the bottom of the groove. The Cassie-type critical nuclei is more preferred energetically. In practice, we adopt the critical nucleus with a lower activation energy barrier.

As shown in the upper panel of Fig. 3.7, we also compute the energy barrier for the heterogeneous nucleation on a flat solid surface with the same boundary condition (the dotted line). A comparison of the activation energy barriers reveals that the use of the microstructures increases the activation energy barrier and thus inhibits the nucleation process when the interpillar spacing is small; in contrast, the use of the microstructures with large interpillar spacing lowers the activation energy barrier and thus enhances the vapor condensation on the solid surface.

In the lower panel of Fig. 3.7, the energy barrier is plotted against the pillar height b, at fixed interpillar spacing $s = 0.07$ (left) and 0.12 (right), respectively. Two typical profiles are shown. In the case of $s = 0.07$, the critical nucleus is in the Wenzel state (region II) when b is small. The energy barrier increases with b. When b becomes large ($b = 0.11$), the critical nucleus becomes the Cassie-type and the further increment of b has no effects on the energy barrier. In contrast, in the case of $s = 0.12$, the critical nucleus is always in the Wenzel state (region III). The energy barrier decreases with b, due to the increasing contact area between the
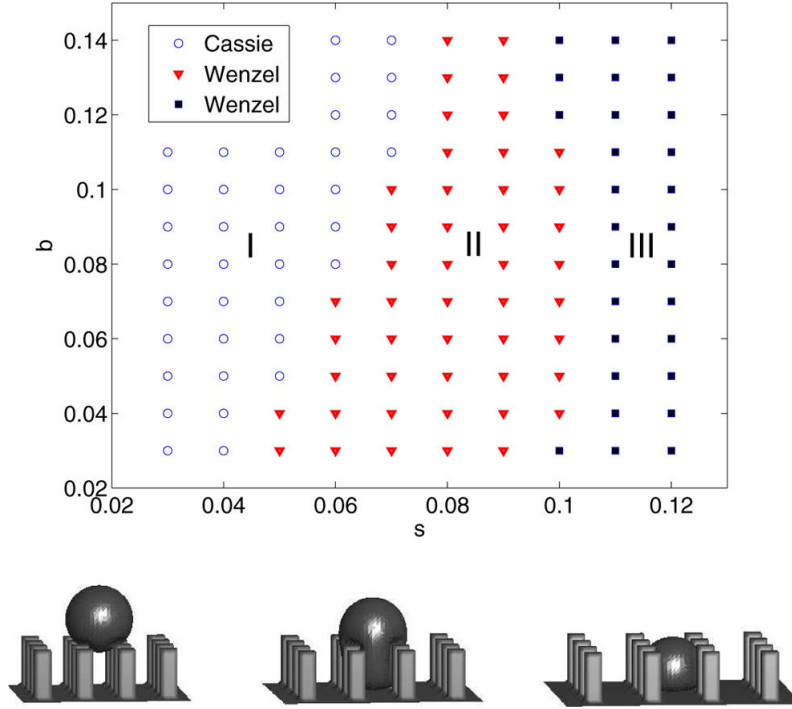
Figure 3.6: Phase diagram of the critical nucleus on the plane of interpillar spacing s and pillar height b. The plane is divided into 3 regions according to the mononiticity of the energy barrier: for fixed b the energy barrier increases in regions I and III, and decreases in region II. Typical configuration of the critical nucleus are shown in the panel below for b=0.12 and s=0.06,0.08,0.10 (from left to right). The supersaturation $\mu = 0.04$.

critical nucleus and the pillars. When the pillars reach certain height, the groove can completely accommodate the critical nucleus, the energy barrier reaches a plateau and further increment of the pillar height has no effects on the energy barrier.

Phase diagram on the $\mu - s$ plane

From Fig. 3.6, we observe there exists a critical value for interpillar spacing at which the critical nucleus changes from the Cassie state to the Wenzel state. It is obvious that the critical interpillar spacing depends on the size of the critical nucleus, which in turn depends on the supersaturation level μ. To quantify the relation between the critical interpillar spacing and size of critical nucleus, we plot the phase diagram of the critical nucleus on the plane of the interpillar spacing s and the supersaturation level μ. The numerical result is shown in Fig. 3.8.
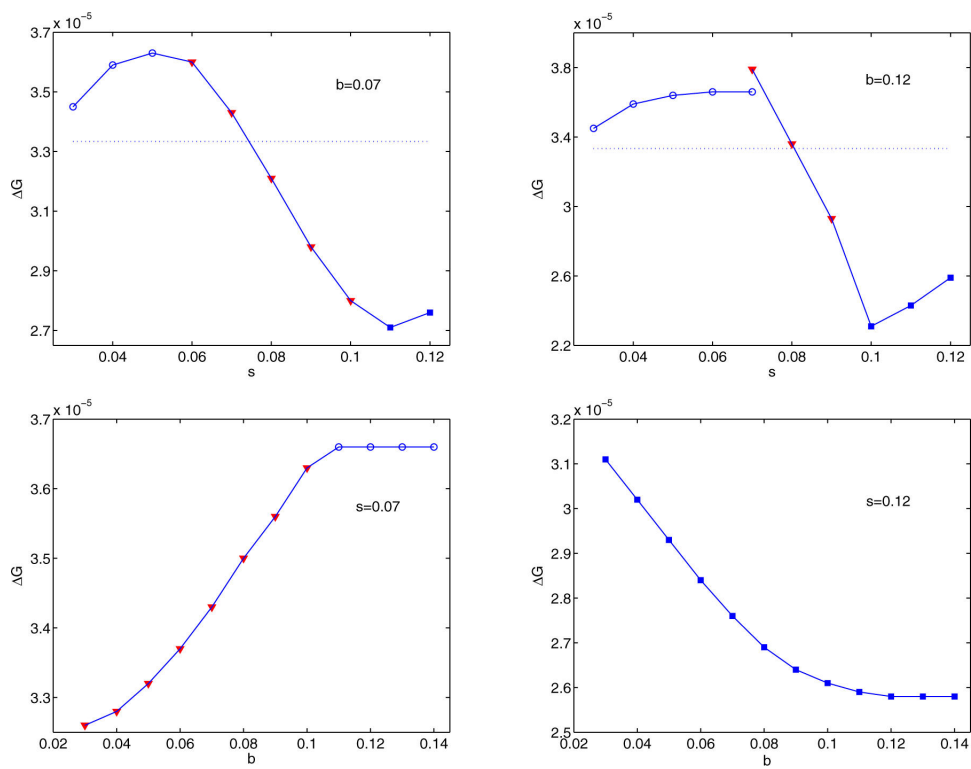
Figure 3.7: In the panel above, we plot energy barrier versus interpillar spacing s while keep the height b constant. In the panel below, we plot energy barrier versus height b while keep the interpillar spacing s constant.
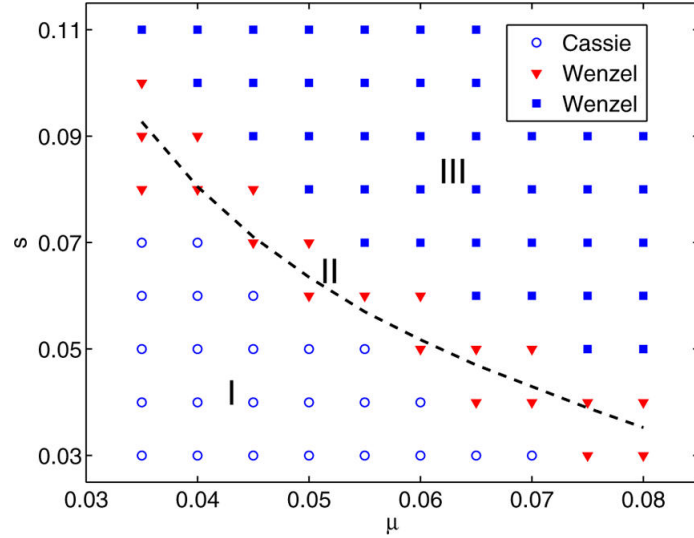
Figure 3.8: Phase diagram of critical nucleus on the interpillar spacing s and super-saturation level μ. The pillar height b is fixed at 0.14. The phase diagram is divided into 3 regions according to the monotonicity of the energy. For fixed μ, the energy increases in region I (open circles) and region III (square) and decreases in region II (inverted triangle). The typical configuration of critical nucleus for each region is shown in the lower panel of Fig. 3.6. The dashed line shows the radius of critical nucleus (s-axis) in homogeneous nucleation with respect to μ.

In the computation, the pillar height is fixed at $b = 0.14$. It is seen that the critical interpillar spacing decreases with the supersaturation level μ (the region of triangles). We also compute the critical radius R_c for the homogeneous nucleation with different supersaturation level μ using the climbing string method. In Fig. 3.8, R_c is plotted against μ (dashed line). It is seen that the critical interpillar spacing follows closely to the critical radii for the homogeneous nucleation. Moreover, the critical radius R_c is inversely proportional to μ: $R_c \sim 1/\mu$. The curve agrees well with the classical nucleation theory using the notion of surface tension, except for large μ ($\mu \gtrsim 0.06$) where the critical nucleus is so small that the description of the interface using notion of surface tension fails.

Next the effects of the energy barrier with respect to supersaturation level μ is investigated, while the pillar height and interpillar spacing are fixed at $b = 0.14$ and $s = 0.06$, respectively. In Fig. 3.9, the activation energy barrier decreases with the supersaturation level μ, regardless the type of the critical nucleus. The log-log plot
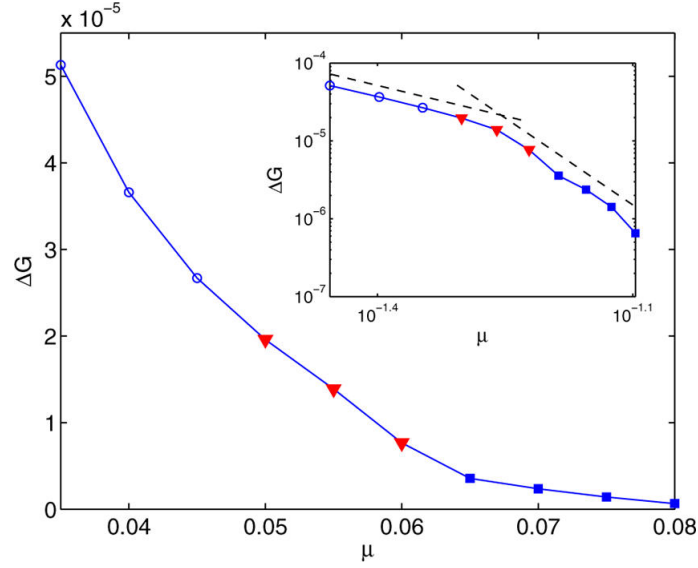
Figure 3.9: The activation energy barrier plotted against the supersaturation level μ. The pillar height and interpillar spacing are fixed at $b = 0.14$ and $s = 0.06$, respectively. The inset is a log-log plot of data. The symbols used have the same meaning as given in Fig. 3.6, Cassie state in region I (open circles), Wenzel state in region II (inverted triangle) and Wenzel state in region III (square).

of ΔG against μ shown in the inset of the figure, indicates the decreasing rate of ΔG is different for the two types of critical nucleus: $\Delta G \propto \mu^{-2.8}$ for the Cassie-type and $\Delta G \propto \mu^{-7}$ for the Wenzel-type.

Effect of surface wettability

The relation between energy barrier ΔG and interpillar spacing s with different surface wettability ϕ_s are investigated. In phase field model, ϕ_s is given as the boundary condition, representing the density field at the solid wall. In Fig. 3.10, the energy barrier and the wetting states of the critical nuclei versus the interpillar spacing are shown for different values of ϕ_s. The general trends of energy barrier and critical nucleus with different ϕ_s are similar. Moreover, the surface wettability plays a similar role as the supersaturation level. The critical interpillar spacing decreases with ϕ_s. The critical interpillar spacing occurs at $s \approx 0.17$ for $\phi_s = 0.1$ and $s \approx 0.13$ for $\phi_s = 0.3$.
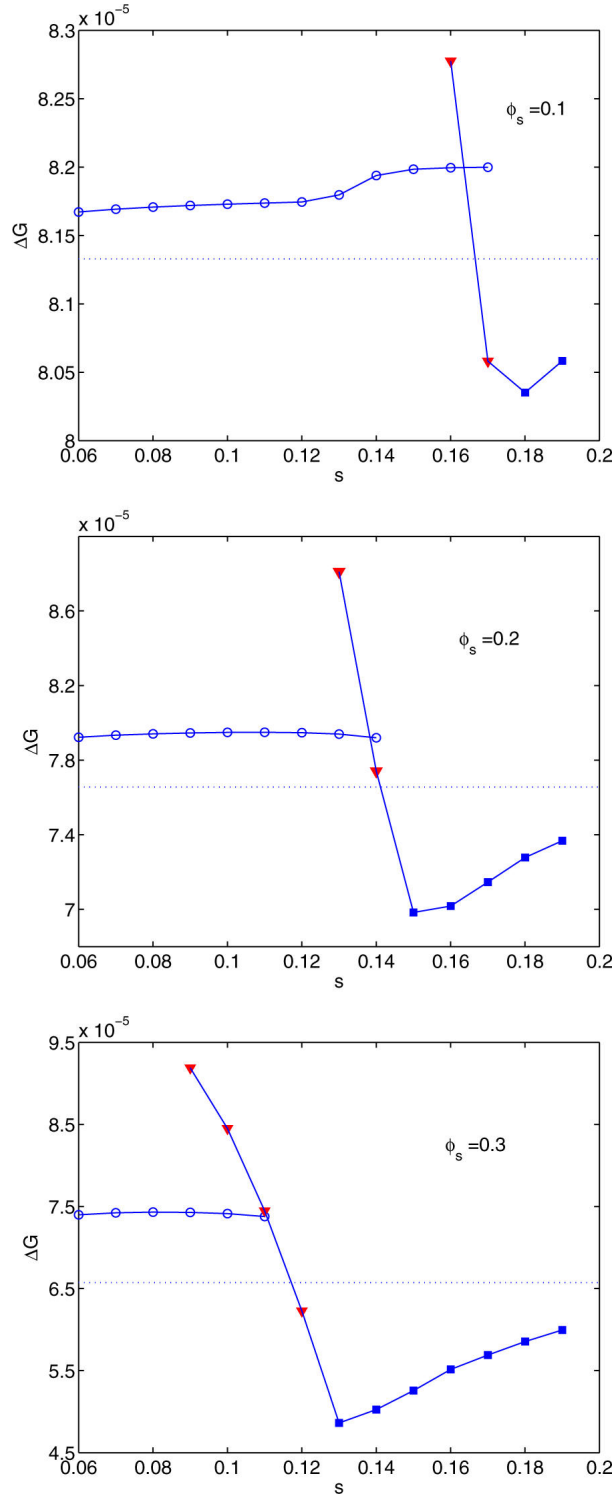
Figure 3.10: The activation energy barrier ΔG against interpillar spacing s with different surface wettability $\phi_s = 0.1, 0.2, 0.3$, respectively. The pillar height and supersaturation level are fixed at $b = 0.24$ and $\mu = 0.03$ respectively. Different symbols are used according to the monotonicity of energy barrier when interpillar spacing s increases. The typical configuration of critical nucleus marked by open circle, inverted triangle and square are shown in the lower panel of Fig. 3.6.

3.4   Conclusion

In this chapter, we numerically study the vapor condensation on hydrophobic surfaces patterned with different pillar structures using a phase field model. The critical nuclei, transition pathways and energy barriers of the nucleation process are accurately determined using the climbing string method. Two nucleation scenarios are observed. In case of high pillar, narrow interpillar spacing, low wettability of the surface and low supersaturation level, the critical nucleus prefers the suspended Cassie state; otherwise, it prefers the impaled Wenzel state. A comparison of the energy barrier with that on a flat surface with the same material reveals that the nucleation is inhibited in the former case and enhanced in the latter case. The critical values of pillar height, interpillar spacing and supersaturation level at which the critical nucleus transit from the Cassie state to the Wenzel state is identified from the phase diagram. It is seen that the critical value of interpillar spacing follows closely to the critical radii in the homogeneous nucleation. The growth of the vapor condensate after the saddle point is computed using the steepest descent dynamics. It is observed that in case of short pillar or wide interpillar spacing, the vapor condensate initially in the Cassie state may evolve to the Wenzel state during the relaxation after passing through the critical nucleus.

In our study, firstly we use Dirichlet boundary condition on the solid substrate. One may also use other types of boundary conditions, such as the Neumann boundary condition. Secondly, the solid substrate is patterned with rectangular pillars. One may also consider other structures of the solid substrate, for example the solid substrate patterned with nails. These are possible factors which may affect the free energy barrier and the type of the critical nucleus in the nucleation process.

Chapter 4

Numerical Study of Wenzel-to-Cassie Transition on a Grooved Solid Surface

In this chapter, we numerically study the Wenzel-to-Cassie transition of the liquid droplet on a grooved solid surface on the free energy landscape, in which the mean force is computed using a molecular dynamics model. On such a surface, the liquid droplet may exhibit either the suspended Cassie state or the impaled Wenzel state. In the former case, the liquid droplet resides above the groove with air trapped inside the groove. While in the latter case, the liquid droplet penetrates the groove and gets trapped. Under specific structures of the groove, both the Cassie state and the Wenzel state may coexist as metastable states. Therefore, the Wenzel-to-Cassie transition becomes a rare event.

In our study, the system is modelled by molecular dynamics, where the particles interact via Lennard-Jones potential. We choose the coarse-grained density of fluid particles as the collective variables and study the phase transition on the free energy landscape mapped in the collective variable space. The transition states, free energy barriers and MFEP are determined using the on-the-fly climbing string method.

In section 4.1, we describe the molecular dynamics simulations to model the liquid droplet on the grooved solid surface. The molecular dynamics of the system
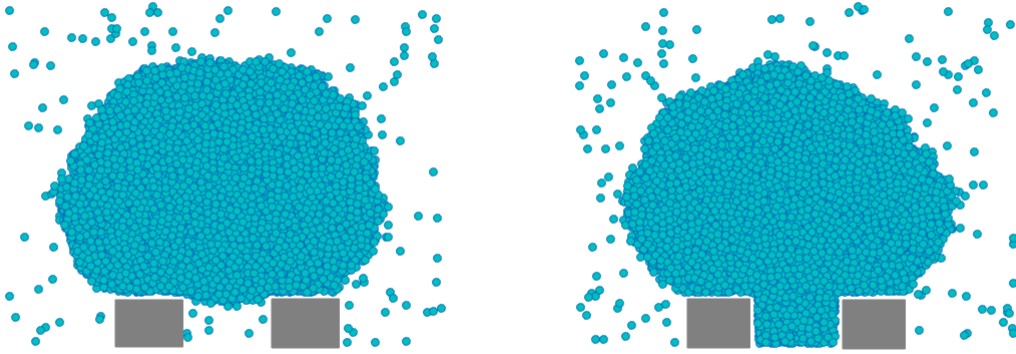
Figure 4.1: Cassie state (left) and Wenzel state (right)

is governed by the Langevin dynamics under NVT ensemble, where the number of particles, volume and temperature are maintained constant. Under specific structures of the groove, we get both the Wenzel state and the Cassie state as metastable states.

In section 4.2, firstly we explain in details, the mathematical formulation of the coarse-grained density of fluid particles as the collective variables. Secondly, we describe the implementation of the on-the-fly climbing string method in studying the transition mechanism for the Wenzel-to-Cassie transition.

In section 4.3, we present the numerical results of the transition states, free energy barriers and MFEP connecting the Wenzel state and the transition state. The configurations of the corresponding molecular dynamics (MD) replicas along the MFEP are also presented. Once the saddle point is identified, we compute the committor value distribution at the saddle point to verify that the saddle point indeed describes the transition state.

4.1　Mathematical Model

In our study, the system consists of an infinitely long cylindrical liquid droplet on the solid surface patterned with an infinitely long rectangular groove. The system is

modelled by molecular dynamics. The liquid droplet may exhibit either the Cassie state or Wenzel state on the grooved surface as shown in Fig. 4.1. It depends on whether the liquid particles penetrate the groove. The computational domain is a rectangular box with $0 < x < 8$ and $0 < y, z < 114$. The solid substrate is at the bottom of the computational domain, patterned with a single groove with width s and height b, confined by two solid steps of width w as shown in Fig. 4.2. The groove is infinitely long in the x direction (the direction into the page). In our computation, we use $s = 12$, $b = 9$ and $w = 10$. Fluid particles are placed in the computational domain with periodic boundary conditions in the x and y directions. The boundary condition on the solid substrate is given by the interactions between the fluid particles and the solid particles. A simple repulsive force is applied at the upper boundary of the domain, as we assume the liquid droplet stays on the solid substrate far away from the top.

The interactions between the fluid particles are of Lennard-Jones (LJ) type. The pairwise shifted LJ potential is given by

$$V_{ff}(r_{ff}) = \begin{cases} 4\epsilon_{ff}\left[\left(\frac{\sigma_{ff}}{r_{ff}}\right)^{12} - \left(\frac{\sigma_{ff}}{r_{ff}}\right)^6\right] & \text{if } r_{ff} < r_c, \\ 0 & \text{otherwise,} \end{cases} \tag{4.1}$$

where $r_c = 2.5\sigma_{ff}$ is the cut-off radius, ϵ_{ff} is the depth of the potential well, σ_{ff} is the distance for zero potential, r_{ff} is the distance between the two fluid particles. In our simulations, we use $\epsilon_{ff} = 1$, $\sigma_{ff} = 1$. The interaction between the fluid particles and the solid particles is also of LJ type given by

$$V_{fs}(r_{fs}) = 4\epsilon_{fs}\left[\left(\frac{\sigma_{fs}}{r_{fs}}\right)^{12} - \left(\frac{\sigma_{fs}}{r_{fs}}\right)^6\right]. \tag{4.2}$$

We use the parameters given in [52], $\sigma_{fs} = 0.921\sigma_{ff}$, $\epsilon_{fs} = 0.25$. The parameter ϵ_{fs} is closely related to the hydrophobicity of the solid surface. $\epsilon_{fs} = 0.25$ corresponds to the equilibrium contact angle for the liquid droplet on the flat solid surface $126° \pm 5°$.

The potential exerted on the fluid particle by the grooved solid surface can be coarse-grained computed to enhance the computational efficiency. The method was

proposed by Wu, Borhan and Fichthorn [62]. With the assumption that the solid particles on the grooved surface are closely packed, the distribution of the solid particles can be described by a uniform particle density ρ_s locally. The coarse-grained potentials between fluid particles and the grooved solid surface can be expressed in terms of ρ_s. We use $\rho_s = \sqrt{2}/(1.2\sigma_{fs}/\sqrt{2})^3$ given in [52]. The coarse-grained potential between the fluid particles and the grooved solid surface consists of two parts: the interactions of the fluid particles with the bottom solid surface and with the solid steps of the groove.

In the former case, the potential energy of the fluid particle at position (y_f, z_f) with respect to the bottom solid surface is given by

$$u^{base}(z_f) = 4\pi\epsilon_{fs}\sigma_{fs}^3\rho_s \left[\frac{\sigma_{fs}^9}{45z_f^9} - \frac{\sigma_{fs}^3}{6z_f^3} \right].$$

In the latter case, suppose the solid step is centred at y_0 with width W, height H and base at $z = 0$, the potential energy of the fluid particle at position (y_f, z_f) with respect to this solid step is given by

$$u^{step}(y_f, z_f) = 4\epsilon_{fs}\rho_s \int_{z^-}^{z^+} \int_{y^-}^{y^+} \int_{-\infty}^{\infty} \left[\frac{\sigma_{fs}^{12}}{(x^2 + y^2 + z^2)^6} - \frac{\sigma_{fs}^6}{(x^2 + y^2 + z^2)^3} \right] dxdydz,$$

where $y^{\pm} = y_0 \pm 0.5W - y_f$, $z^- = -z_f$, $z^+ = H - z_f$. For simplicity, let $(y_1, z_1) = (y^+, z^+)$ and $(y_2, z_2) = (y^-, z^-)$. After integration, we have

$$u^{step}(y_f, z_f) = 4\epsilon_{fs}\rho_s\sigma_{fs}^6 \sum_{j=1}^{2} \sum_{k=1}^{2} (-1)^{j+k} \times \left[\sigma_{fs}^6 u_{rep}(y_j, z_k) - u_{att}(y_j, z_k) \right], \quad (4.3)$$

where

$$u_{att}(a, b) = \frac{-\pi(2a^4 + a^2b^2 + 2b^4)}{24a^3b^3\sqrt{a^2 + b^2}}, \quad (4.4)$$

and

$$\begin{aligned} u_{rep}(a, b) &= \frac{-\pi(a^2+b^2)^{-\frac{7}{2}}}{11520a^9b^9} \times [128(a^{16} + b^{16}) + 448(a^{14}b^2 + a^2b^{14}) \\ &+ 560(a^{12}b^4 + a^4b^{12}) + 280(a^{10}b^6 + a^6b^{10}) + 35a^8b^8]. \end{aligned} \quad (4.5)$$

Equations 4.4 and 4.5 exhibit singularities at $a = 0$ or $b = 0$. It happens when the fluid particle resides near the boundaries of the solid step. In the case when

both a and b are close to zero, a strong repulsive force is exerted on the fluid particle to push it away from the solid step. In case of only one of a or b is close to zero, asymptotic approximations of equations 4.4 and 4.5 are derived to avoid large numerical discrepancy given in [62]. Since the equations are symmetric with respect to a and b, we just write down the case when only a is small. For small $\epsilon > 0$, in case of $|a| < \epsilon$:

$$u_{att}(a, b) \approx -\pi\text{sgn}(b)\left(\frac{1}{12a^3} + \frac{3a}{32b^4}\right) + \mathcal{O}(\epsilon^2), \tag{4.6}$$

and

$$u_{rep}(a, b) \approx -\pi\text{sgn}(b)\left(\frac{1}{90a^9} + \frac{63a}{2560b^{10}}\right) + \mathcal{O}(\epsilon^2), \tag{4.7}$$

where $\text{sgn}(x) = \begin{cases} 1 & \text{if } x \geq 0, \\ -1 & \text{if } x < 0. \end{cases}$

Then the coarse-grained potential U_s between the fluid particle and the grooved solid surface is given by

$$U_s(y_f, z_f) = u^{step}(y_f, z_f) + u^{base}(z_f). \tag{4.8}$$

In addition, as we assume that the liquid droplet is far from the upper boundary of the domain, the boundary condition at the upper boundary is given by a simple repulsive potential:

$$U_t(d) = \frac{1}{d^{12}},$$

where d is the distance of the fluid particle to the upper boundary of the domain.

So far, we have finished describing all the potentials involved in the molecular dynamics system. Next, we describe the Langevin dynamics under NVT ensemble, where the number of fluid particles, volume and temperature of the system are maintained constant. Consider the system consisting of n fluid particles. Let $x = (\mathbf{x_1}, ..., \mathbf{x_n})$ and $v = (\mathbf{v_1}, ..., \mathbf{v_n})$ be the positions and velocities of the particles respectively, where $\mathbf{x_i}, \mathbf{v_i} \in \mathbb{R}^3$. The temperature of the system is given by

$$T = \frac{1}{3nk_B}\sum_{k=1}^{n}|\mathbf{v_k}|^2, \tag{4.9}$$
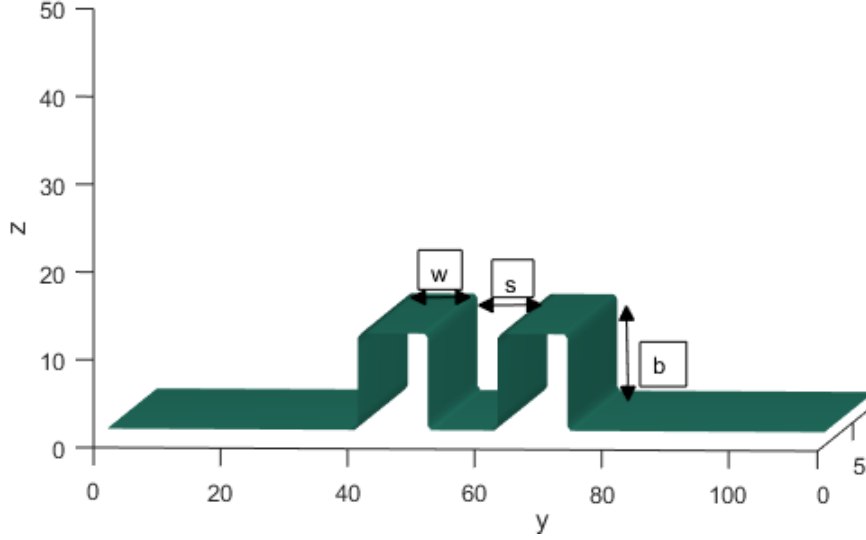
Figure 4.2: Solid surface patterned with a single groove with width s=12 and height b=9. The groove is confined by two steps with width w=10. The computational domain is of size $8 \times 114 \times 114$. In the figure, the x-axis is oriented into the page.

where k_B is the Boltzmann constant. The initial velocities are generated using independent standard normal random variables followed by the velocity rescaling. We proceed to the following 3 steps:

1. Generate vectors $w = (\mathbf{w_1}, , ..., \mathbf{w_n})$, where $\mathbf{w_i} \in \mathbb{R}^3$ for $i = 1, ..., n$. w are n independent vectors of standard normal random variables.

2. Compute the temperature associated with w, $\hat{T} = \frac{1}{3nk_B} \sum_{k=1}^{n} |\mathbf{w_k}|^2$.

3. Rescale the velocities with respect to the given temperature T by $\mathbf{v_i} = \mathbf{w_i}\sqrt{T/\hat{T}}$, for $i = 1, ...n$.

The Langevin dynamics is introduced to maintain the temperature at T during the molecular dynamics simulation, given by

$$\begin{cases} \dot{\mathbf{x}}_\mathbf{i}(t) = \mathbf{v_i}(t), \\ \dot{\mathbf{v}}_\mathbf{i}(t) = -\nabla_{\mathbf{x_i}} V(x) - \gamma\mathbf{v_i}(t) + \sqrt{2\gamma k_B T}\eta_i(t), \end{cases} \quad (4.10)$$

where $-\nabla_{\mathbf{x_i}} V(x)$ is the potential force , γ is the friction coefficient, $\eta_i(t) \in \mathbb{R}^3$ is a vector of standard normal random variables. In the computation, we use the parameters $\gamma = 1$, $k_B T = 0.7$. To solve the Langevin dynamics numerically, we use the second order numerical scheme proposed by Vanden-Eijnden, Ciccotti [57]. Let $x^k = (\mathbf{x_1^k}, ..., \mathbf{x_n^k})$, $v^k = (\mathbf{v_1^k}, ..., \mathbf{v_n^k})$ be the positions and velocities of the particles at the k-th time step during the molecular dynamics simulation, the numerical scheme with a discrete time step Δt is given by

$$
\begin{cases}
\mathbf{x_i^{k+1}} = \mathbf{x_i^k} + \Delta t \mathbf{v_i^k} + A_i^k, \\
\mathbf{v_i^{k+1}} = \mathbf{v_i^k} - \frac{\Delta t}{2} \left(\nabla_{\mathbf{x_i^k}} V(x^k) + \nabla_{\mathbf{x_i^{k+1}}} V(x^{k+1}) \right) - \Delta t \gamma \mathbf{v_i^k} + \sqrt{2\gamma k_B T \Delta t} \xi_i^k - \gamma A_i^k,
\end{cases}
$$
$$(4.11)$$

where $A_i^k = \frac{\Delta t^2}{2}(-\nabla_{\mathbf{x_i^k}} V(x^k) - \gamma \mathbf{v_i^k}) + \sqrt{2\gamma k_B T} \Delta t^{\frac{3}{2}} \left(\frac{1}{2}\xi_i^k + \frac{1}{2\sqrt{3}}\eta_i^k \right)$, ξ_i^k and η_i^k are $2n$ independent vectors of standard normal random variables.

To simulate the liquid droplet on the grooved solid surface, firstly we place 10000 fluid particles at a simple cubic lattice site into a $8 \times 36 \times 36$ rectangular prism. Then we place this rectangular prism right above the groove as shown in Fig. 4.3 (left). The system is allowed to equilibrate itself according to the Langevin dynamics given in Eq. 4.10. At the steady state, the liquid droplet exhibits the suspended Cassie state as shown in Fig. 4.3 (right). The Wenzel state can be obtained using a different initial configuration. At the beginning, let the fluid particles penetrate the groove and get trapped between the two solid steps, see Fig. 4.4 (left). The system evolves to the Wenzel state at the steady state as shown in Fig. 4.4 (right).

4.2 Numerical Methods

In this section, firstly we give a detailed mathematical formulation for the collective variables. Secondly, we prove that the tensor matrix $M(z)$ involved in our problem is non-singular. Note that an invertible $M(z)$ is a compulsory condition for the implementation of the on-the-fly climbing string method. Finally, we describe the
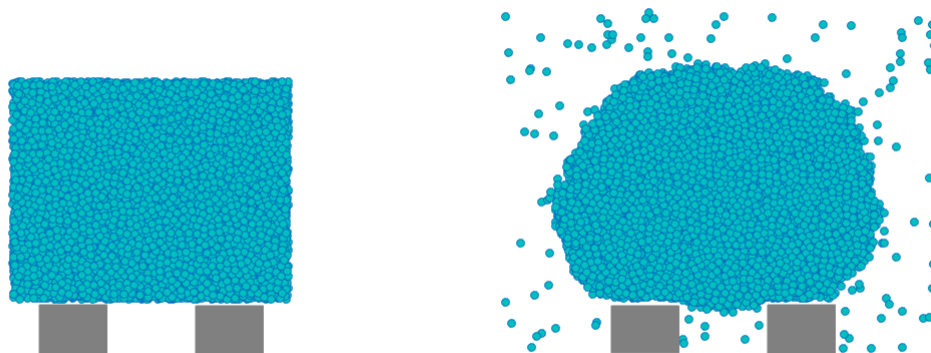
Figure 4.3: Initial configuration of the molecular dynamics system (left) evolves to the Cassie state (right) at the steady state. The system is simulated in three dimensional space, the picture shows a projection onto the y, z plane.
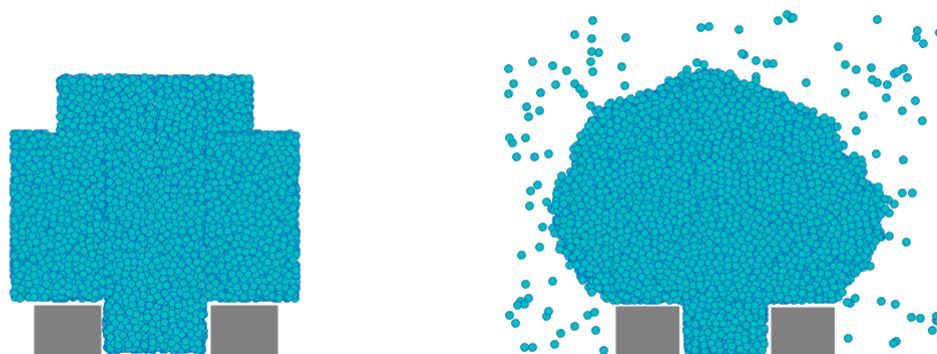
Figure 4.4: Initial configuration of the molecular dynamics system (left) evolves to the Wenzel state (right) at the steady state. The system is simulated in three dimensional space, the picture shows a projection onto the y, z plane.
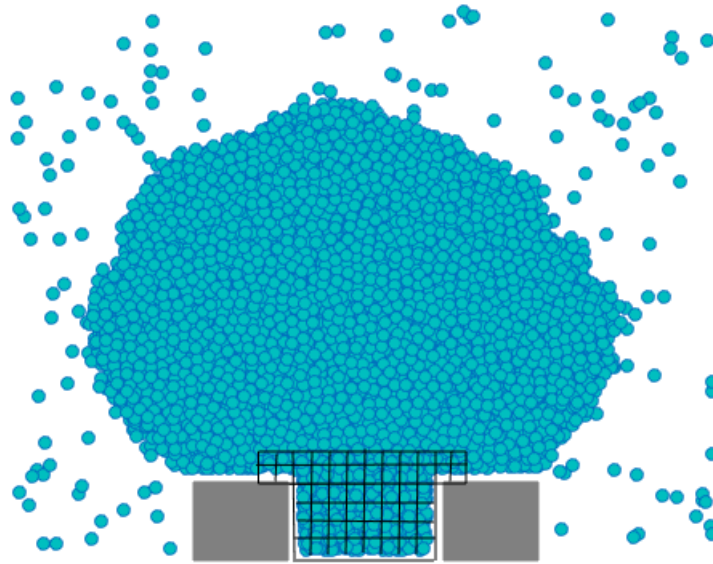
Figure 4.5: The region containing the groove is partitioned into N small bins $B_1, ..., B_N$, each of size $8 \times 2 \times 2$. We introduce N collective variables $\theta_1(x), ..., \theta_N(x)$ as functions of x. Each collective variable $\theta_k(x)$ represents the number of fluid particles in the bin B_k.

implementation of the on-the-fly climbing string method in studying the Wenzel-to-Cassie transition.

4.2.1 Collective Variables and Restrained Potential

We choose the coarse-grained density of fluid particles as the collective variables. Firstly, a region is chosen from the computational domain, which contains the groove. Then the region is partitioned into N small bins $B_1, ..., B_N$, each of size $8 \times 2 \times 2$ as shown in Fig. 4.5. We introduce N collective variables $\theta(x) = (\theta_1(x), ..., \theta_N(x))$, where $x = (\mathbf{x_1}, ..., \mathbf{x_n})$ are the positions of the fluid particles. Each collective variable $\theta_i(x)$ represents the number of fluid particles in the bin B_i. Mathematically, $\theta_i(x)$ is given by

$$\theta_i(x) = \theta_i(\mathbf{x_1}, ..., \mathbf{x_n}) \tag{4.12}$$

$$= \int_{B_i} \sum_{k=1}^{n} \delta(\mathbf{x_k} - y) dy, \tag{4.13}$$

where $\delta(\cdot)$ is the Dirac delta function defined in the three dimensional space. The gradient of the collective variable $\theta_i(x)$ to $\mathbf{x_j}$ is computed using integration by parts as follows:

$$
\begin{aligned}
\nabla_{\mathbf{x_j}} \theta_i(x) &= \nabla_{\mathbf{x_j}} \int_{B_i} \sum_{k=1}^{n} \delta(\mathbf{x_k} - y) dy \\
&= \nabla_{\mathbf{x_j}} \int_{B_i} \delta(\mathbf{x_j} - y) dy \\
&= \int_{B_i} \nabla_{\mathbf{x_j}} \delta(\mathbf{x_j} - y) dy \\
&= -\int_{B_i} \nabla_y \delta(\mathbf{x_j} - y) dy \\
&= -\int_{\Gamma_i} \delta(\mathbf{x_j} - y) \hat{n} d\sigma \\
&= -\delta(d(\mathbf{x_j}, \Gamma_i)) \hat{n},
\end{aligned}
\tag{4.14}
$$

where Γ_i denotes the boundary of the bin B_i, $\hat{n}$ is the unit outward normal vector to the boundary Γ_i, $d(\mathbf{x_j}, \Gamma_i) = \min_{y \in \Gamma_i} |\mathbf{x_j} - y|$ is the distance from $\mathbf{x_j}$ to the boundary Γ_i. In the last step of Eq. 4.14, the Dirac delta function $\delta(\cdot)$ is defined in the one dimensional space. Next, let $x^* = \underset{y \in \Gamma_i}{\operatorname{argmin}} |\mathbf{x_j} - y|$, then we have

$$\nabla_{\mathbf{x_j}} \theta_i(x) = -\delta(|\mathbf{x_j} - x^*|) \hat{n}. \tag{4.15}$$

The term $\nabla_{\mathbf{x_j}} \theta_i(x)$ is used in the restrained molecular dynamics in the on-the-fly climbing string method. The restrained molecular dynamics constrains the system at $\theta_i(x) = z_i$, where $\theta_i(x)$ is the current value of the collective variable and z_i is the target value. It is realized by adding the following restrained potential to the Hamiltonian of the original system given by

$$V_{res}(x) = \frac{\kappa}{2} \sum_{i=1}^{N} (\theta_i(x) - z_i)^2 . \tag{4.16}$$

The gradient of the restrained potential to $\mathbf{x_j}$ is given by

$$\nabla_{\mathbf{x_j}} V_{res}(x) = \kappa \sum_{i=1}^{N} (\theta_i(x) - z_i) \nabla_{\mathbf{x_j}} \theta_i(x). \tag{4.17}$$

Based on the computation above, we notice that the particle lying on the boundary of the bin experiences a force of infinite magnitude, which cannot be realized in the computer simulation. Therefore, we approximate the Dirac delta function in Eq. 4.15 using a smooth function given by

$$\delta(|\mathbf{x_j} - x^*|) \approx \begin{cases} \frac{4}{0.444} \exp\left(\frac{-1}{1-16|\mathbf{x_j}-x^*|^2}\right), & \text{if } |\mathbf{x_j} - x^*| \leq 0.25, \\ 0, & \text{otherwise.} \end{cases} \tag{4.18}$$

Then the term $\nabla_{\mathbf{x_j}} \theta_i(x)$ is approximated by

$$\nabla_{\mathbf{x_j}} \theta_i(x) \approx \begin{cases} -\hat{n} \left[\frac{4}{0.444} \exp\left(\frac{-1}{1-16|\mathbf{x_j}-x^*|^2}\right) \right], & \text{if } |\mathbf{x_j} - x^*| \leq 0.25, \\ 0, & \text{otherwise.} \end{cases} \tag{4.19}$$

Based on the approximation above, note that the particles within distance 0.25 to the boundary of the bin experience the force from the restrained potential. We illustrate the effects of the restrained potential force $-\nabla_{\mathbf{x_j}} V_{res}(x)$ in Fig. 4.6. Consider the particles lying near the boundary of the bin B_i with the target collective variable z_i. If $\theta_i(x) > z_i$, then the restrained potential force drives the particles near the boundary away from the bin (upper panel); otherwise, the restrained potential force drives the particles near the boundary into the bin (lower panel).

The Langevin dynamics equipped with the restrained potential is given by

$$
\begin{cases}
\dot{\mathbf{x}}_\mathbf{i}(t) = \mathbf{v}_\mathbf{i}(\mathbf{t}), \\
\dot{\mathbf{v}}_\mathbf{i}(t) = -\nabla_{\mathbf{x}_\mathbf{i}}V(x) - \gamma\mathbf{v}_\mathbf{i}(t) + \sqrt{2\gamma k_B T}\eta_i(t) - \kappa\sum_{j=1}^{N}(\theta_j(x(t)) - z_j)\nabla_{\mathbf{x}_\mathbf{i}}\theta_j(x),
\end{cases}
\tag{4.20}
$$

where $k_B T = 0.7, \gamma = 1$ and $\kappa = 0.25$. We use this restrained molecular dynamics to evolve the MD replicas during the implementation of the on-the-fly climbing string method.

4.2.2 Property of the Tensor Matrix M(z)

Recall the tensor matrix $M(z)$ given in [38], the (i, j) entry of $M(z)$ is given by

$$
M_{ij}(z) = \frac{1}{T}\int_0^T \sum_{k=1}^{n} \frac{\partial\theta_i(x(t))}{\partial x_k}\frac{\partial\theta_j(x(t))}{\partial x_k}dt.
\tag{4.21}
$$

In our problem, based on the collective variables defined in the previous part, the (i, j) entry of $M(z)$ is given by

$$
M_{ij}(z) = \frac{1}{T}\int_0^T \sum_{k=1}^{n} \langle\nabla_{\mathbf{x}_\mathbf{k}}\theta_i(x(t)), \nabla_{\mathbf{x}_\mathbf{k}}\theta_j(x(t))\rangle\,dt,
\tag{4.22}
$$

where the dynamics of $x(t)$ is governed by the restrained molecular dynamics given in Eq. 4.20 with target value z. Note that for the implementation of the on-the-fly climbing string method, we require $M(z)$ be a non-singular matrix for all z.

In the previous section, the collective variables are defined as the number of fluid particles in each small bin. During the Wenzel-to-Cassie transition, the fluid particles move out of the groove. It is possible that at some intermediate configuration between the Wenzel state and the Cassie state, some bins are empty, i.e. $\theta_i(x) = 0$ for some $i = 1, ..., N$. Suppose there exist a bin B_k such that $\theta_k(x(t)) \equiv 0$ for $t \in [0, T]$, then the corresponding k-th row and k-th column of the tensor matrix $M(z)$ are zeros. Then $M(z)$ becomes a singular matrix. It contradicts to our original assumption that $M(z)$ should be a non-singular matrix.

However, we notice that the empty bins actually do not participate in the reaction. In other words, the collective variables with value zeros are irrelevant to the transition, thus can be safely removed. At the same time, the zero rows and columns of the tensor matrix $M(z)$ are removed correspondingly. Let $\hat{M}(z)$ be the resulting square matrix after removing the zero rows and columns from the matrix $M(z)$. It is suffice to show that $\hat{M}(z)$ is non-singular.

Theorem 4.1. *Consider the tensor matrix $M(z)$ defined in Eq. 4.22. For $i = 1, ..., N$, if $\theta_i(x(t)) \equiv 0$ for all $t \in [0, T]$, then we remove the i-th column and i-th row from the matrix $M(z)$. Let $\hat{M}$ be the resulting square matrix. Then $\hat{M}$ is invertible.*

Proof. It is known that an irreducible diagonal dominant matrix is invertible. Therefore it is suffice to show that the matrix $\hat{M}$ satisfies the following 3 conditions:

1. $\hat{M}$ is diagonal dominant.

2. There exist a row i of $\hat{M}$, such that strict diagonal dominance holds, i.e. $|\hat{M}_{ii}| > \sum_{j \neq j} |\hat{M}_{ij}|$.

3. $\hat{M}$ is irreducible.

For condition 1, it is suffice to show that $|\hat{M}_{ii}| \geq \sum_{i \neq j} |\hat{M}_{ij}|$ for all $i = 1, ..., N$. Suppose at some time $t \in [0, T]$ during the molecular dynamics simulation, the particle with coordinate $\mathbf{x_k}$ is near the boundary shared by the bins B_i and B_j, then we must have $\nabla_{\mathbf{x_k}} \theta_i(x) = -\nabla_{\mathbf{x_k}} \theta_j(x)$. And it leads to the following two properties: (1) $\nabla_{\mathbf{x_k}} \theta_i(x) + \nabla_{\mathbf{x_k}} \theta_j(x) = 0$, (2) $\langle \nabla_{\mathbf{x_k}} \theta_i(x), \nabla_{\mathbf{x_k}} \theta_j(x) \rangle \leq 0$. The latter implies $\hat{M}_{ij} \leq 0$ if $i \neq j$. Let $Z(t)$ be the set of particles lying only near the boundary of the bin B_i at the time $t \in [0, T]$. Then the summation of the i-th row of the matrix $\hat{M}$ is given by

$$
\begin{aligned}
\sum_{j=1}^{N} \hat{M}_{ij} &= \tfrac{1}{T} \int_0^T \sum_{k=1}^n \left\langle \nabla_{\mathbf{x_k}} \theta_i(x(t)), \sum_{j=1}^{N} \nabla_{\mathbf{x_k}} \theta_j(x(t)) \right\rangle dt \\
&= \tfrac{1}{T} \int_0^T \sum_{k \in Z(t)} |\nabla_{\mathbf{x_k}} \theta_i(x(t))|^2 dt \geq 0.
\end{aligned}
\tag{4.23}
$$

Since $\hat{M}_{ij} \leq 0$ if $i \neq j$, then we have

$$\sum_{j=1}^{N} \hat{M}_{ij} = |\hat{M}_{ii}| - \sum_{j \neq i} |\hat{M}_{ij}| \geq 0. \tag{4.24}$$

Therefore $\hat{M}$ is diagonal dominant.

For condition 2, consider the small bin on the top left corner in Fig. 4.5. The particles on the top left corner of the bin are not near the boundaries of other bins. So the set $Z(t)$ defined in condition 1 is not empty. Therefore there exists some row i such that $\sum_{j=1}^{N} \hat{M}_{ij} > 0$. Since $\hat{M}_{ij} \leq 0$ if $i \neq j$, we have $|\hat{M}_{ii}| > \sum_{j \neq i} |\hat{M}_{ij}|$. So in the row i of the matrix $\hat{M}$, strict diagonal dominance holds.

For condition 3, firstly we assume that at any intermediate configuration between the Wenzel state and the Cassie state, all the non-empty bins are connected. In other words, for any two bins B_i and B_j with non-zero collective variables, we are always able to find a sequence of bins $B_{k,0}, B_{k,1}, ..., B_{k,M}$ with $B_i = B_{k,0}$ and $B_j = B_{k,M}$, such that the consecutive bins $B_{k,l}$ and $B_{k,l+1}$ are next to each other geometrically and $\theta_{k,l}(x(t)) \not\equiv 0$ for $t \in [0, T]$ and $l = 0, ..., M$. Thus by definition of the matrix $\hat{M}$, it is a connected matrix.

$\square$

4.2.3   Implementation of the On-the-fly Climbing String Method

In this part, we describe the implementation of the on-the-fly climbing string method in studying the Wenzel-to-Cassie transition of the liquid droplet on the grooved solid surface. We start with the molecular configuration of the Wenzel state x_w, and at the same time compute the corresponding collective variables $\theta(x_w)$ (see Fig. 4.7). Starting from the collective variable configuration of the Wenzel state $\theta(x_w)$, we use the on-the-fly climbing string method to compute the saddle point on the free energy landscape, which corresponds to the transition state for the Wenzel-to-Cassie transition.
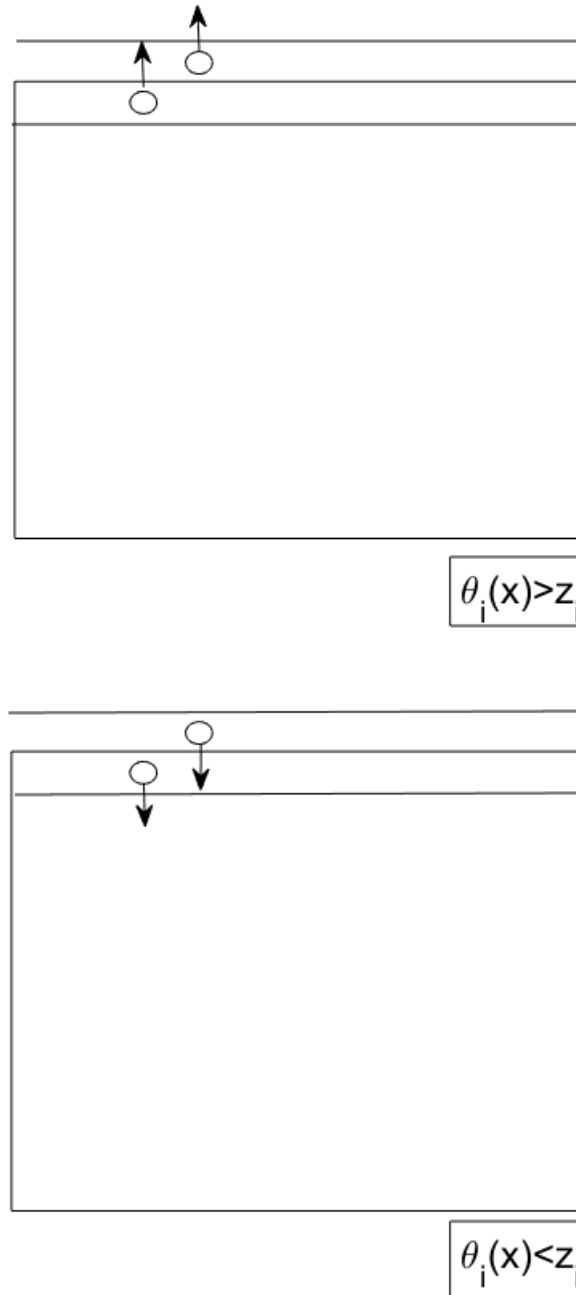
Figure 4.6: Consider the particles residing near the boundary of the bin B_i with the target collective variable z_i. The particles experience the restrained potential force $-\nabla_{\mathbf{x_j}} V_{res}(x)$ given by Eq. 4.17. Let $\theta_i(x)$ be the current value of the collective variable. In the panel above, when $\theta_i(x) > z_i$, the restrained potential force will drive the particle away from the bin. While in the panel below, when $\theta_i(x) < z_i$, the restrained potential force will drive the particles into the bin.
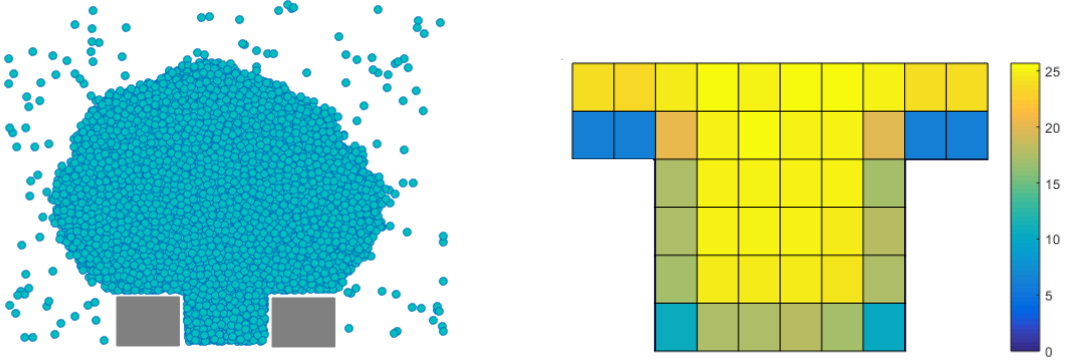
Figure 4.7: Molecular configuration of the Wenzel state (left) and the corresponding collective variables (right). The density of fluid particles near the solid substrate (blue and green) is smaller than the homogeneous liquid phase (yellow).

For the implementation of the on-the-fly climbing string method, an initial string $z(\alpha)$, $\alpha \in [0, 1]$ is constructed in the collective variable space, parametrized by its normalized arc length α. The initial point of the string is fixed at the Wenzel state, i.e. $z(0) = \theta(x_w)$. For the construction of the intermediate points and the final point along the initial string, we assume the dewetting process starts at the bottom right corner of the groove. A vapor cavity is initially formed and grows. A schematic presentation of the points along the initial string is shown in Fig. 4.8. The collective variables at the bottom right corner of the domain turn blue gradually, which corresponds to the formation and growth of the vapor cavity in the molecular dynamics system.

In the computation, the string is discretized into $R + 1$ images $\{z^0, z^1, ..., z^R\}$ uniformly distributed along the string, where z^m is the image at $\alpha = m/R$ for $m = 0, ..., R$. Along the discretized string, we assign each image z^m an MD replica x^m. Initially, we set $x^m = x_w$ for all $m = 0, 1, ..., R$. It is obvious that the MD replica x^m is not well constrained at $\theta(x^m) = z^m$ for $m = 1, ..., R$. In order to make the MD replicas constrained at the corresponding images, we run the restrained molecular dynamics given in Eq. 4.20 for 2×10^4 steps with a discrete time step $\Delta t = 0.004$. For example in Fig. 4.9, it is observed that the MD replica x^R is well constrained
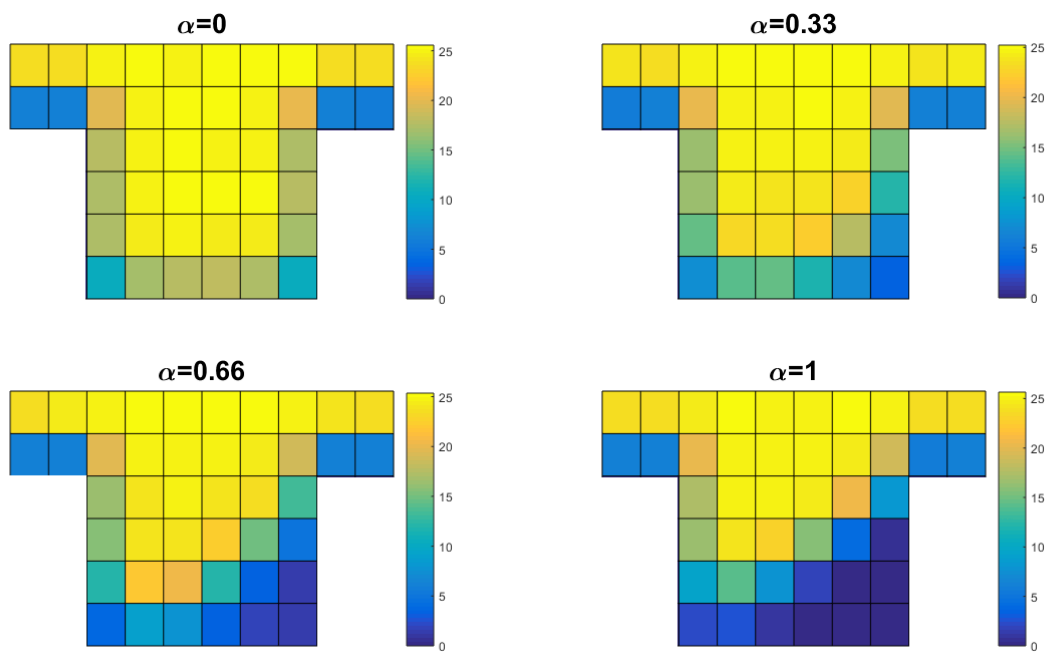
Figure 4.8: Points along the initial string $z(\alpha)$. The values of collective variables decrease gradually at the bottom right corner of the domain. When $\alpha = 1$, the bottom right corner of the groove turns deep blue corresponding to the vapor cavity formed in the molecular dynamics system.
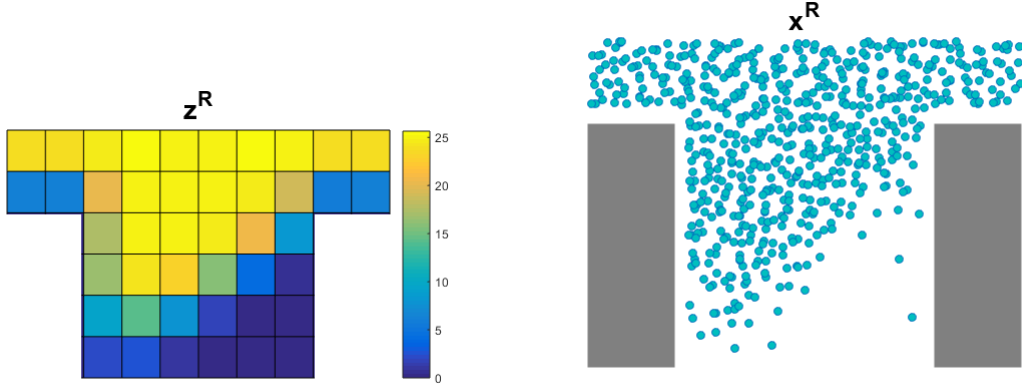
Figure 4.9: The end image z^R on the initial string and its corresponding MD replica x^R. The deep blue region at the bottom right corner (left) corresponds to the vapor cavity in the molecular dynamics system (right). The MD replica x^R is well constrained at $\theta(x^R) = z^R$.

at the image z^R.

Let z_k^m and x_k^m be the instantaneous position of the image z^m and the MD replica x^m at the k-th iteration during the string evolution. We update the discretized string with a discrete time step $\Delta t = 0.004$ using the on-the-fly climbing string method according to the following 3 steps:

1. Concerted evolution of the discretized string and the corresponding MD replicas at the k-th iteration by

$$
\begin{cases}
z^{m,\star} = z_k^m - \frac{\kappa \Delta t}{\gamma_z} \bar{F}(z_k^m, x_k^m) \text{ for } m = 0, 1, ..., R-1, \\
z^{R,\star} = z_k^R - \frac{\kappa \Delta t}{\gamma_z} \left[\bar{F}(z_k^R, x_k^R) - 2 \left\langle \bar{F}(z_k^R, x_k^R), \hat{\tau} \right\rangle \hat{\tau} \right], \\
x_{k+1}^m = \text{starting from } x_k^m, \text{ run the restrained molecular dynamics given} \\
\qquad \text{in Eq. 4.20 for one time step } \Delta t \text{ with } z = z^{m,*} \text{ for } m = 0, 1, ..., R,
\end{cases}
$$
(4.25)

where $\bar{F}(z_k^m, x_k^m) = M(x_k^m) \left(z_k^m - \theta(x_k^m) \right)$, and the (i, j) entry of the matrix $M(x)$ is given by $\sum_{l=1}^n \left\langle \nabla_{\mathbf{x_l}} \theta_i(x), \nabla_{\mathbf{x_l}} \theta_j(x) \right\rangle$, $\gamma_z = 1000$ and $\kappa = 0.25$. $\hat{\tau} = \frac{z_k^R - z_k^{R-1}}{|z_k^R - z_k^{R-1}|}$ is the unit tangent vector to the string at the end image z_k^R.

2. Interpolate a curve through the images $\{z^{0,*}, ..., z^{R,*}\}$ using linear interpolation. Then distribute $R + 1$ new images uniformly along the interpolated curve according to the equal arc length parametrization to obtain the string $\{z_{k+1}^0, z_{k+1}^1, ..., z_{k+1}^R\}$ at the new iteration.

3. Go to step 1 or stop when the string reaches the steady state.

The string converges to the MFEP connecting the Wenzel state and the saddle point at the steady state. Note that the parameter γ_z influences the evolution of the string. When γ_z is small, the string converges to the MFEP faster but the string evolution becomes more noisy. Note that the value $\gamma_z = 1000$ is not optimized for efficiency in our study.

According to Eq. 4.25, the evolution of the end image z^R depends on the tangent of the string at the end point $\hat{\tau}$. We assume that the transition occurs only at the liquid-vapor interface. Based on this assumption, we define the tangent $\hat{\tau}$ only at the liquid-vapor interface. The bins corresponding to the liquid-vapor interface are identified with the following criteria. Firstly consider the image z^m in the entry-wise form $z^m = \left(z_{(1)}^m, ..., z_{(N)}^m \right)$, where $z_{(k)}^m$ is the k-th entry of image z^m corresponding to the collective variable in the bin B_k. If (a) $z_{(k)}^R \geq 2.0$ and (b) $z_{(k)}^R \leq \frac{2}{3} z_{(k)}^0$, then B_k and its adjacent bins are regarded as being at the liquid-vapor interface. For example, at the saddle point along the MFEP (z^R in Fig. 4.12), the tangent $\hat{\tau}$ is given by Fig. 4.10.

4.3 Results and Discussion

In our study, the string is discretized into 13 images $z^0, z^1, ..., z^{12}$ (R=12). The string is evolved with the a discrete time step $\Delta t = 0.004$. We use $\gamma_z = 500$ before 1.5×10^6 iterations and $\gamma_z = 1000$ afterwards. Let z_n^R be the instantaneous position of the end image z^R at the n-th iteration during the string evolution. The evolution
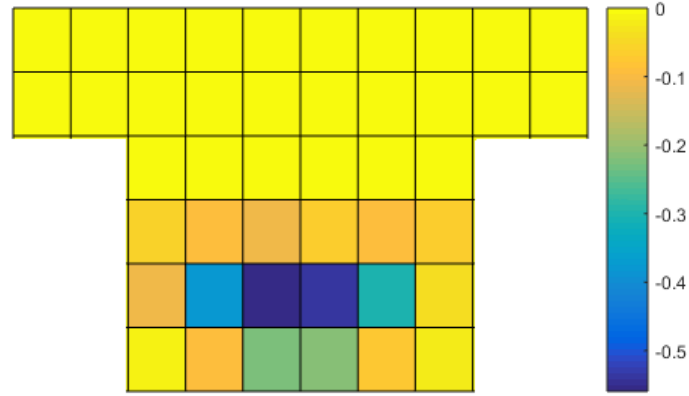
Figure 4.10: The tangent $\hat{\tau}$ at the saddle point along the MFEP. The entry of the tangent is set to be zero if the corresponding bin is not at the vapor-liquid interface.
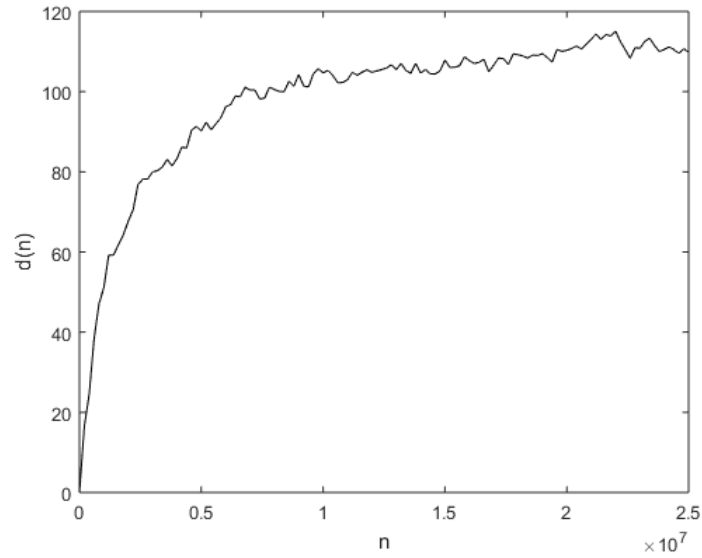
Figure 4.11: Distance $d(n)$ of the end image z_n^R from its initial condition z_0^R during the string evolution. The distance $d(n)$ becomes almost steady after $n = 1 \times 10^7$ iterations. We use $\gamma_z = 500$ before $n = 1.5 \times 10^6$ iterations and $\gamma_z = 1000$ afterwards.
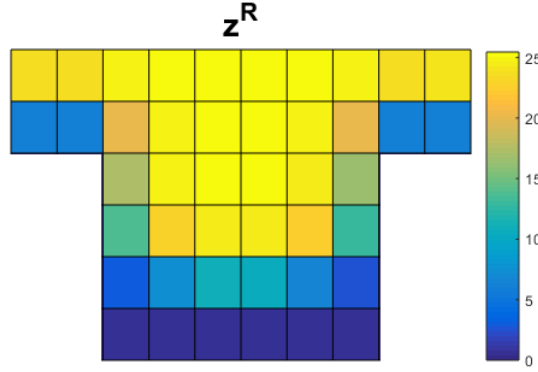
Figure 4.12: The configuration of the saddle point.

of the end image z^R is monitored by its distance from the initial condition given by

$$d(n) = |z_n^R - z_0^R|_1, \tag{4.26}$$

where $|\cdot|_1$ denotes the L1 norm. In Fig. 4.11, $d(n)$ becomes almost steady at $n = 1 \times 10^7$ iterations. We observe the fluctuations in the evolution of the end image. The dynamics of the string evolution is governed by a stochastic differential equation. Hence, the fluctuation of the end image may be caused by the stochastic process in the equation. We conclude that the end image converges to the saddle point, which corresponds to the transition state. The configuration of the saddle point is shown in Fig. 4.12. At the transition state, the liquid droplet is completely detached from the bottom solid surface and a symmetric liquid meniscus is formed inside the groove. The MFEP connecting the saddle point and the Wenzel state is shown in Fig 4.13, and the configurations of the corresponding MD replicas are shown in Fig. 4.14. The MFEP shows that the dewetting process starts from the two bottom corners of the groove followed by the complete detachment of the liquid phase from the bottom solid surface.

The free energy along the MFEP is computed using thermodynamics integration given by

$$F(z(\alpha)) - F(z(0)) = \sum_{i=1}^{N} \int_0^\alpha \frac{\partial F(z_i(\alpha'))}{\partial z_i(\alpha')} \frac{dz_i(\alpha')}{d\alpha'} d\alpha'. \tag{4.27}$$

The term $\frac{\partial F(z)}{\partial z_i}$ is approximated using a time-averaging approach [38] given by

$$\frac{\partial F(z)}{\partial z_i} = \lim_{T \to \infty} \frac{1}{T} \int_0^T \kappa \left[\theta_i(x(t)) - z_i \right] dt. \tag{4.28}$$

The dynamics of $x(t)$ in 4.28 is governed by the restrained molecular dynamics given in Eq. 4.20. To approximate 4.28, we run the restrained molecular dynamics at the target value z for $\hat{N} = 3 \times 10^5$ steps with a discrete time step $\Delta t = 0.002$. And the approximation is given by

$$\frac{\partial F(z)}{\partial z_i} \approx \frac{1}{\hat{N}} \sum_{k=1}^{\hat{N}} \kappa \left[\theta_i(x(t_k)) - z_i \right], \tag{4.29}$$

where $t_k = k\Delta t$. Then we use the trapezoidal rule to approximate the integral 4.27 with $\alpha' = 0, \frac{1}{R}, \frac{2}{R}, ..., 1$. The free energy profile along the MFEP is shown in Fig. 4.15. It is seen that the free energy increases progressively for $0 \leq \alpha \leq 0.66$ and remains almost constant for $\alpha \geq 0.75$. At the saddle point, the free energy attains the maximum.

Finally, in order to verify the saddle point indeed describes the transition state, we generate configurations from the transition state ensemble. By definition, the transition state ensemble is the ensemble of points in the phase space (x, v) which are restricted to the isocommittor $1/2$ surface with Boltzmann distribution. If the committor values of these configurations are centred around $1/2$, then the saddle point indeed describes the transition state.

As discussed in chapter 2, the isocommittor $1/2$ surface can be locally approximated by the hyperplane P, which is tangent to it at the saddle point. The configurations x in the original phase space restricted to the hyperplane P satisfy the following equation:

$$\left\langle \tilde{n}, \theta(x) - z^R \right\rangle = 0, \tag{4.30}$$

where $\tilde{n}$ is the unit normal vector to the hyperplane P given by

$$\tilde{n} = \frac{M(z^R)^{-1}\hat{\tau}}{|M(z^R)^{-1}\hat{\tau}|}. \tag{4.31}$$

The tensor matrix $M(z^R)$ given by Eq. 4.22 is a well-conditioned matrix with condition number 245 as shown in Fig. 4.16. Thus we can compute $M(z^R)^{-1}$ directly. Together with the tangent vector of the string at the end image $\hat{\tau}$, we determine the unit normal vector $\tilde{n}$ as shown in Fig. 4.17. To generate samples of configurations from the hyperplane P, we add the following additional potential to the Hamiltonian of the original system:

$$V_\kappa = \frac{\kappa}{2}(\langle \tilde{n}, \theta(x) - z^R \rangle)^2, \tag{4.32}$$

where the constant κ is chosen large enough to make sure that the samples are well constrained on the hyperplane P. We generate 66 samples from the hyperplane P. And from each sample, we generate 66 different trajectories by assigning random initial velocities. The committor value is given by the probability that the trajectory will evolve to the Cassie state first rather than the Wenzel state. In Fig. 4.18, we show some samples from the transition state ensemble and their committor values. The committor value distribution of the samples is centred around 0.4 as shown in Fig. 4.19. Thus the hyperplane P is very closed to the isocommittor $1/2$ surface. So we conclude that the saddle point indeed describes the transition state.

In Ref. [46], the wetting transition was studied using the phase field model. Our result agrees well with the result in Ref. [46] qualitatively. At the transition state, partial infiltration of liquid occurs and the liquid starts to touch the bottom. In Ref. [24], the wetting transition was studied using the molecular dynamics model on the free energy landscape. The system is modelled under NPT ensemble, where the number of particles, the pressure of the system and the temperature remain constant. At the transition state, it was observed that a vapor cavity is formed at one corner of the groove, which is different from our observation. This may be due to the different ensembles used in the molecular dynamics simulations.

4.4   Conclusion

In this chapter, we study the Wenzel-to-Cassie transition of a liquid droplet on a grooved solid surface. The system is modelled by molecular dynamics, where the particles interact with each other via Lennard-Jones potential. We choose the coarse-grained density of fluid particles as the collective variables, and study the phase transition on the free energy landscape mapped in the collective variable space. We give a detailed mathematical formulation for the collective variables. The formulation provides a way to study the molecular dynamics system using the local density of the particles, which can also be applied to study other similar problems. The saddle point, free energy barrier and MFEP are determined using the on-the-fly climbing string method. From the saddle point, we determine the transition state. At the transition state, the liquid droplet is completely detached from the bottom solid surface and a symmetric liquid meniscus is formed inside the groove. Moreover, the MFEP connecting the Wenzel state and the transition state shows that the dewetting process starts at the two bottom corners of the groove.

In our study, the groove is partitioned into cells, in which the local density of the particles is measured and further considered as the collective variables. The size of the cell should be chosen wisely. If the cell is large, then the number of cells in the groove is few. It results in a low resolution of the local density field. If the cell is small, then the cell contains too few particles which cannot be used to describe the local density.

Moreover, the committor distribution at the saddle point is centred around 0.4, which is not exactly 0.5. It is acceptable since the committor function is very sensitive near the transition state. If the atomistic configuration is perturbed slightly away from the exact transition ensemble, the committor function will either increase to 1 or decrease to 0 very fast. This is because the atomistic configuration goes into the basin of the attraction of one local minimum after small perturbation.
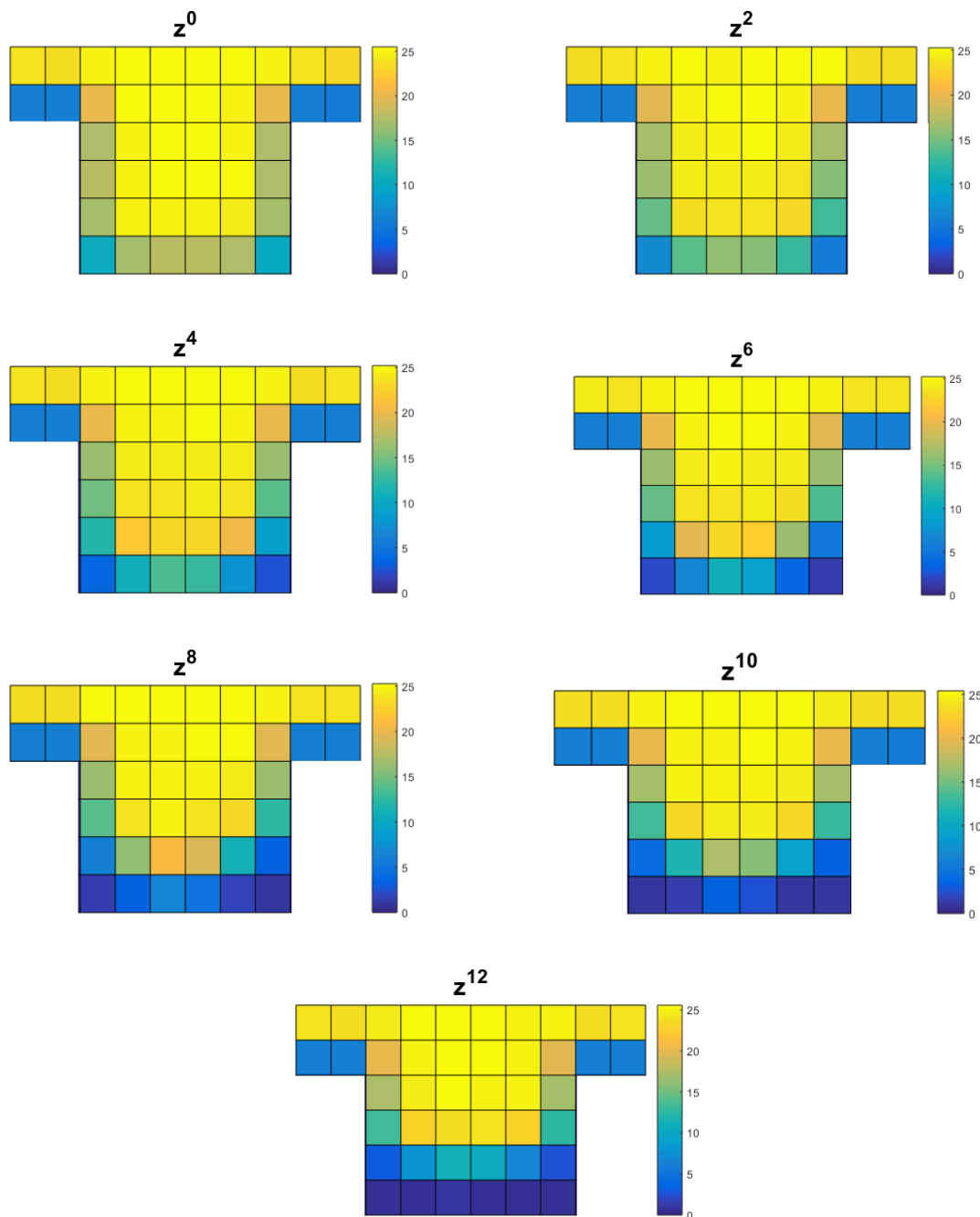
Figure 4.13: Images along the MFEP connecting the Wenzel state and the saddle point. z^{12} is the saddle point corresponding to the transition state.
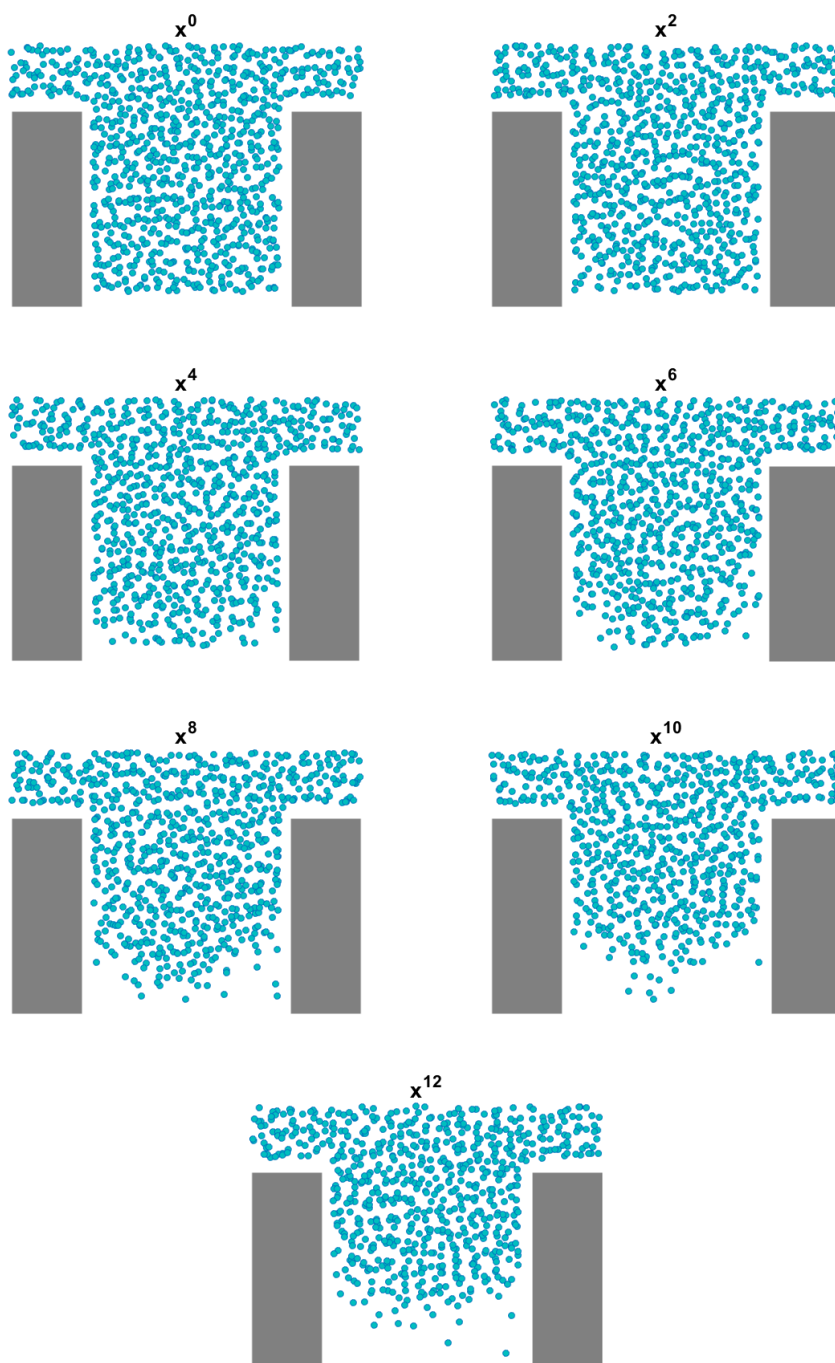
Figure 4.14: The configurations of the corresponding MD replicas with respect to the images in Fig. 4.13. It is seen that the Wenzel-to-Cassie transition starts from the two bottom corners of the groove. At the transition state, the liquid droplet is completely detached from the bottom solid surface. Furthermore, a symmetric liquid meniscus is formed inside the groove.
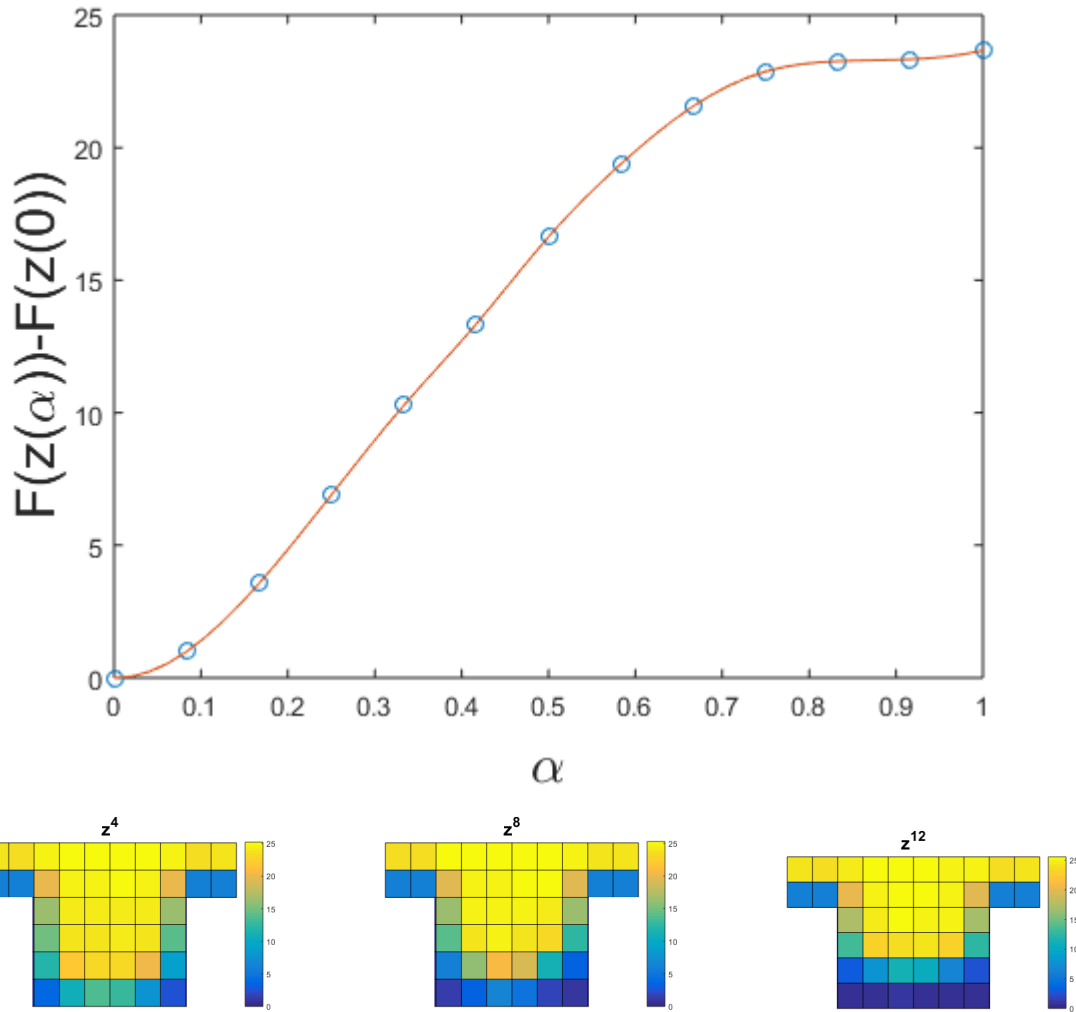
Figure 4.15: Free energy profile along the MFEP connecting the Wenzel state and the transition state. The free energy increases for $0 \leq \alpha \leq 0.66$ and remains almost constant for $0.75 \leq \alpha \leq 1$. $\alpha = 0$ corresponds to the Wenzel state and $\alpha = 1$ corresponds to transition state. In the lower panel, the images correspond to $\alpha = 0.33, 0.66, 1.0$, respectively.
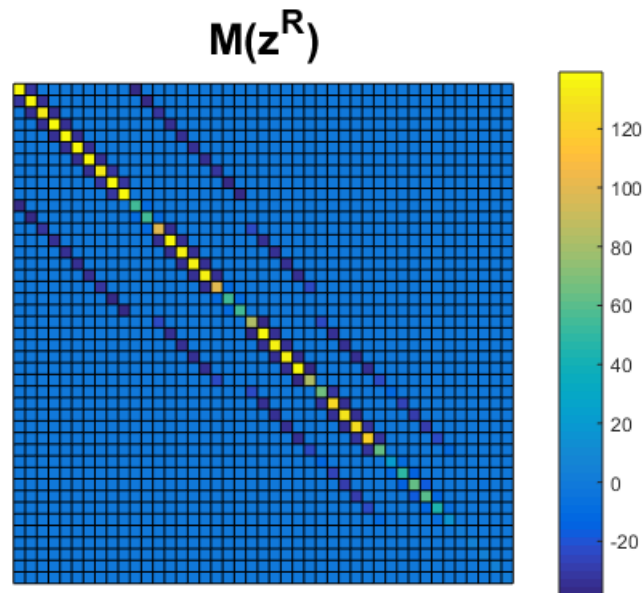
Figure 4.16: Tensor matrix M at the saddle point z^R. The diagonals are all positive. Negative entries are observed on off diagonals. The condition number of $M(z^R)$ is approximately 245, thus $M(z^R)$ is well-conditioned.
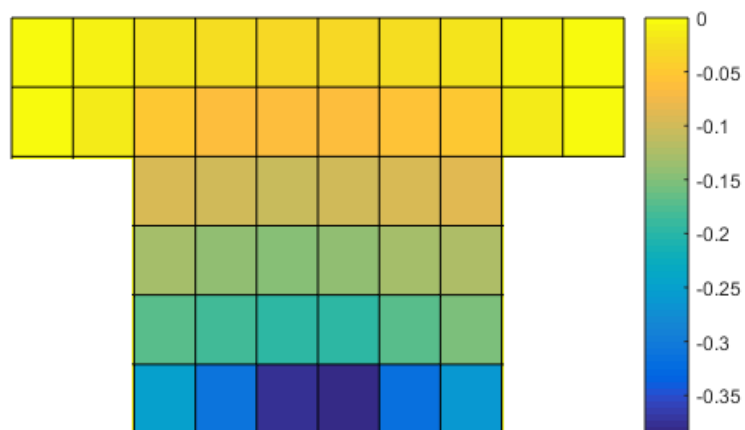
Figure 4.17: The unit normal vector $\tilde{n}$ to the hyperplane P at the saddle point z^R.
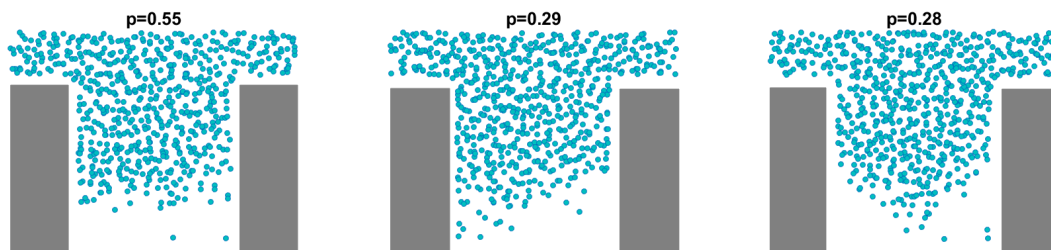
Figure 4.18: The molecular dynamics configurations from the transition state ensemble. The committor value p is the probability that the trajectory initiated from each sample by assigning random initial velocities, will evolve to the Cassie state first rather than the Wenzel state.
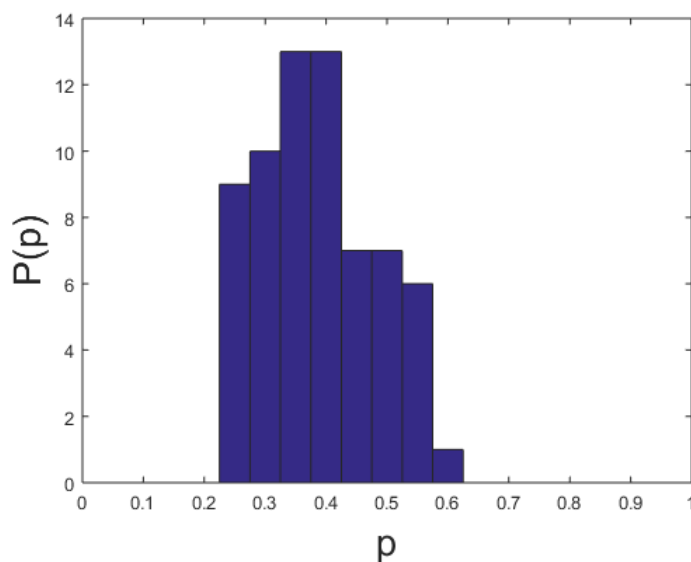
Figure 4.19: Committor value distribution on the hyperplane P at the saddle point z^R. The distribution is centred around 0.4.

Chapter 5

Numerical Study of Isotropic-Nematic Phase Transition in Hard Spherocylinder System

In this chapter, we numerically study the isotropic-nematic phase transition in the hard spherocylinder system on the free energy landscape, in which the mean force is computed using a molecular dynamics model. A spherocylinder consists of a central cylinder part with diameter D and length L capped with two hemispheres at the two ends. In our study, $L = 2, D = 1$. The term 'hard' refers to the pairwise potential between two spherocylinders given by

$$U(r) = \begin{cases} \infty \text{ if } r > D, \\ 0 \quad \text{otherwise.} \end{cases} \tag{5.1}$$

where r is the distance between the two line segments which represent the axes of the central cylinder portion of the two spherocylinders.

In our study, the system is modelled by molecular dynamics under the isothermal-isobaric ensemble, where the number of spherocylinders, pressure and temperature of the system remain constant. In the case of low pressure, the spherocylinders prefer random distributions and orientations, which leads to the isotropic phase;

otherwise, the spherocylinders prefer alignments with each other, which leads to the nematic phase. Under specific pressure, the isotropic phase and the nematic phase may coexist as metastable states. Thus the isotropic-nematic phase transition in the hard spherocylinder system is a rare event.

The isotropic phase and nematic phase can be characterized by an order parameter, which measures the nematic ordering of the system, i.e. the alignments of spherocylinders with respect to the nematic direction. We choose the order parameter as the collective variable and study the phase transition on the free energy landscape mapped in the collective variable space. The transition states, free energy barriers and minimum free energy paths (MFEP) are determined using the on-the-fly string method. Moreover, we investigate the effect of an external aligning field on the isotropic-nematic phase transition.

In subsection 5.1.1, we describe the molecular dynamics of the hard spherocylinders. The dynamics are of two kinds: the translational motion and the orientational motion. When collision occurs between two spherocylinders, their translational and angular velocities are updated according to the law of conservation of total energy and momentum.

In subsection 5.1.2, we describe the molecular dynamics simulations under the isothermal-isobaric ensemble. We modify the integration scheme proposed by Bussi, Zykova-Timan and Parrinello [25], in order to apply it to the hard spherocylinder system. In our study, the pressure of the system is maintained at $P = 6.0 k_B T$, in which the isotropic phase and nematic phase coexist as metastable states.

In section 5.2, firstly we introduce an order parameter which measures the average alignment of spherocylinders with respect to the nematic direction. Secondly, we describe the implementation of the on-the-fly string method in studying the transition mechanism for the isotropic-nematic phase transition. At last, we describe the hard spherocylinder system under the effects of an external aligning field.

In section 5.3, we present the numerical results of the transition state, free energy

barriers and MFEP for the isotropic-nematic phase transition in the hard sphero-cylinder system. The configurations of the corresponding molecular dynamics (MD) replicas along the MFEP are also presented. Furthermore, a comparison of the free energy barriers between the systems with and without the external aligning field reveals that the external aligning field lowers the free energy barrier, thus enhances the isotropic-nematic phase transition.

5.1 Mathematical Model

5.1.1 Molecular Dynamics of the Hard Spherocylinders

The system may exhibit either the isotropic phase or the nematic phase as shown in Fig. 5.1. A spherocylinder is characterized by the center $q \in \mathbb{R}^3$ and the unit vector $u \in \mathbb{R}^3$ representing the central axis. The motion of the spherocylinder is of two kinds: the translational motion of the center and the rotation of the central axis about the center. Let $p, \omega \in \mathbb{R}^3$ denote the translational velocities and angular velocities, respectively. When no collision occurs, the spherocylinders move freely according to the following dynamics:

$$\begin{cases} \dot{q}(t) = p(t), \\ \dot{u}(t) = \omega(t) \times u(t), \end{cases} \tag{5.2}$$

where the length of the vector u is always kept at 1. According to the differential equation above, the unit vector u rotates in the plane perpendicular to the angular velocities ω. The forward Euler scheme with a discrete time step Δt is applied to solve Eq. 5.2 numerically [1]:

$$q = q + \Delta t \times p,$$

$$\Omega = \Delta t |\omega|,$$

$$\Omega_{\cos} = \cos(\Omega),$$

$$\Omega_{\sin} = \sin(\Omega),$$
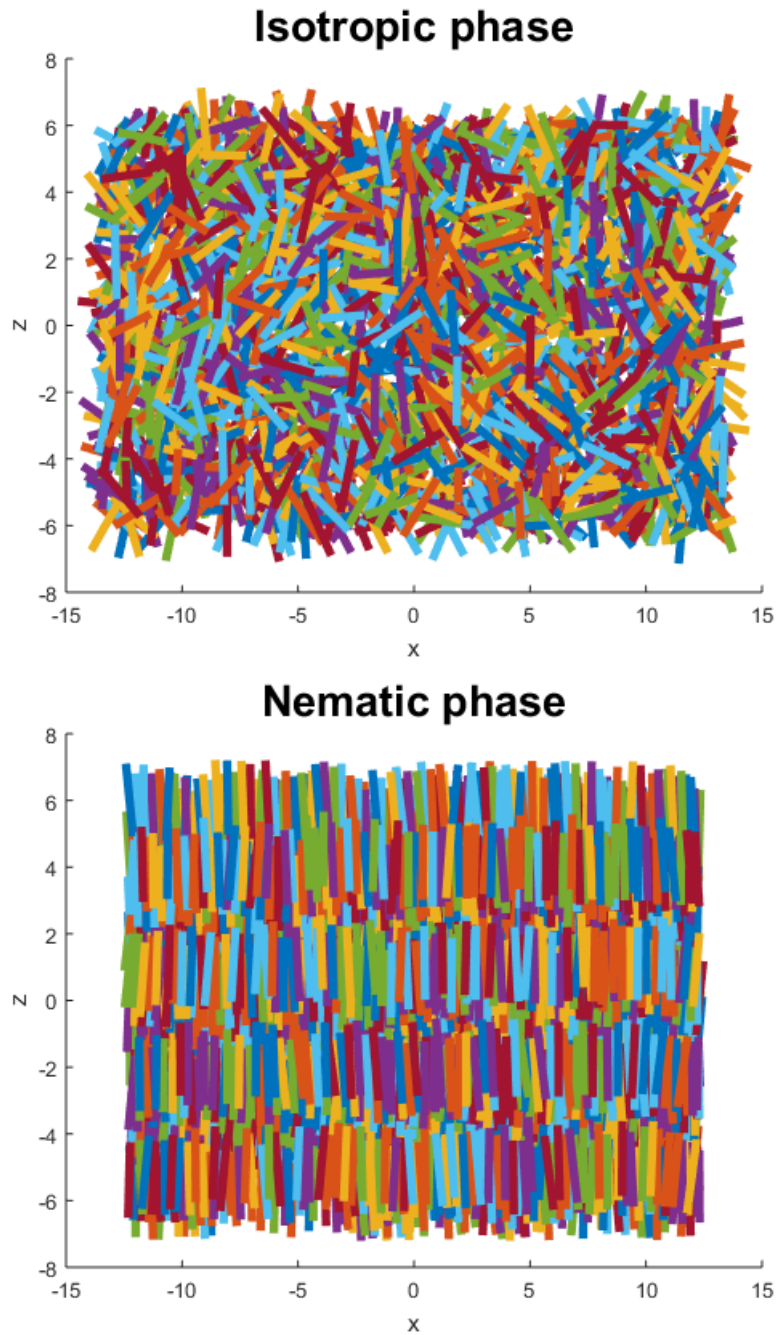
Figure 5.1: Isotropic phase and nematic phase of the hard spherocylinder system with $D = 1$ and $L = 2$. The isotropic phase is shown at the top with volume $V = 8800$ and the nematic phase is shown at the bottom with volume $V = 7500$.
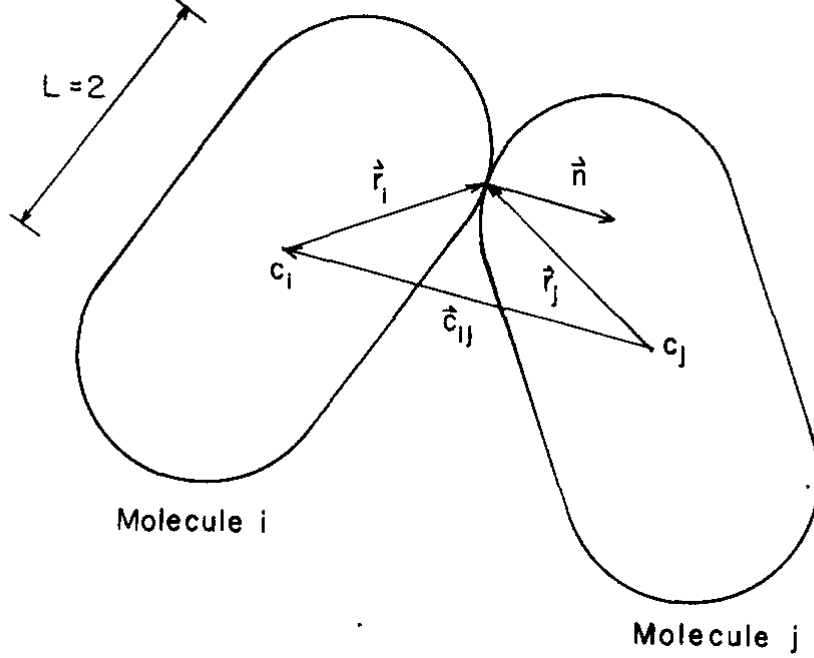
Figure 5.2: The collision between two spherocylinders i and j. The two spherocylinders has centers c_i and c_j. The vectors from the center to the contact point are given by $\vec{r}_i$ and $\vec{r}_j$. The normal vector to the surface of the spherocylinders at the contact point is given by $\vec{n}$. The picture is taken from Ref. [44].

$$u_1 = \Omega_{\cos} u_1 + \Omega_{\sin} \left(\omega_2 \times u_3 - \omega_3 \times u_2 \right) / |\omega|,$$

$$u_2 = \Omega_{\cos} u_2 + \Omega_{\sin} \left(\omega_3 \times u_1 - \omega_1 \times u_3 \right) / |\omega|,$$

$$u_3 = \Omega_{\cos} u_3 + \Omega_{\sin} \left(\omega_1 \times u_2 - \omega_2 \times u_1 \right) / |\omega|. \tag{5.3}$$

When collision occurs between two spherocylinders, the translational and angular velocities are updated. We recall the collision dynamics proposed in [44], which guarantees the conservation of total energy and momentum. Suppose the collision occurs between the two spherocylinders i and j as shown in Fig. 5.2. The spherocylinders have centers c_i and c_j, unit vectors u_i and u_j representing the central axes, translational velocities p_i and p_j, angular velocities ω_i and ω_j. Let P be the coordinate of the contact point. Let $\vec{r}_i$ and $\vec{r}_j$ be the vectors from the center of each spherocylinder to P, i.e. $\vec{r}_i = P - c_i$ and $\vec{r}_j = P - c_j$. Let $\vec{n}$ be the unit

outward normal vector to the surface of the spherocylinder i at the contact point P. For simplicity, we consider the sphercylinder as a linear rotor with the moment of inertia $I = \frac{1}{12}L^2$. Let p_i', p_j', ω_i' and ω_j' be post-collision translational and angular velocities. The translational and angular velocities are updated according to the following equations:

$$
\begin{cases}
p_i' = p_i + \Delta p, \\
p_j' = p_j - \Delta p, \\
\omega_i' = \omega_i + \vec{r}_i \times \Delta p/I, \\
\omega_j' = \omega_j - \vec{r}_j \times \Delta p/I,
\end{cases}
\tag{5.4}
$$

where Δp is the collision impulse given by

$$
\Delta p = \frac{\langle -g_{ij}, \vec{n} \rangle \, \vec{n}}{1 + \left(|\vec{r}_i \times \vec{n}|^2 + |\vec{r}_j \times \vec{n}|^2 \right)/2I},
\tag{5.5}
$$

where $g_{ij} = p_i - p_j + \omega_i \times \vec{r}_i - \omega_j \times \vec{r}_j$ is the relative velocity between the spherocylinders i and j, $<,>$ denotes the inner product. We assume all the spherocylinders are of unit mass.

In the molecular dynamics simulations, the spherocylinders move a distance with a discrete time step. Therefore when collision occurs, the two spherocylinders meet each other and overlap. We should update the translational and angular velocities only when the instant collision occurs between any two spherocylinders. In other words, we need to put a criterion to identify the instant when the two spherocylinders overlap for the first time. Note that when the collision occurs between two spherocylinders i and j, the relative velocity g_{ij} and the outward normal vector $\vec{n}$ should satisfy $\langle g_{ij}, \vec{n} \rangle > 0$. After the instant collision, the velocities changes directions, which leads to $\langle g_{ij}', \vec{n} \rangle < 0$, where g_{ij}' is the relative velocities between the spherocylinders i and j after collision. Thus the criteria to identify the instant collision are

1. When two spherocylinders overlap each other, i.e. $r < D$,

2. $\langle g_{ij}, \vec{n} \rangle > 0$,

where r is the shortest distance between the two line segments which represent the axes of the central cylinder portion of the two spherocylinders i and j.

5.1.2 Isothermal-Isobaric Ensemble

For the molecular dynamics simulation under isothermal-isobaric ensemble, we refer to the integration scheme [25], which was originally proposed to study the Lennard-Jones system. We modify the integration scheme slightly, in order to apply it to the hard spherocylinder system.

At the beginning, we place n spherocylinders into a rectangular box of size $s \times s \times b$ with periodic boundary conditions. The system is subjected to an external pressure P_{ext}. During the simulation, the height of the rectangular box b is fixed. We adjust the side length s of the rectangular box in order to control the volume. Let $q = (\mathbf{q_1}, ..., \mathbf{q_n})$ and $u = (\mathbf{u_1}, ..., \mathbf{u_n})$ be the centers and the unit vectors representing the central axes of the spherocylinders. Let $p = (\mathbf{p_1}, ..., \mathbf{p_n})$ and $\omega = (\boldsymbol{\omega_1}, ..., \boldsymbol{\omega_n})$ be the translational and angular velocities. All the vectors are of dimension three: $\mathbf{q_i}, \mathbf{u_i}, \mathbf{p_i}, \boldsymbol{\omega_i} \in \mathbb{R}^3$ for $i = 1, ..., n$. Firstly, we consider the center-of-mass coordinate $\mathbf{q_{cm}}$ and $\mathbf{p_{cm}}$, and the centers $r = (\mathbf{r_1}, ..., \mathbf{r_n})$, the translational velocities $\pi = (\boldsymbol{\pi_1}, ..., \boldsymbol{\pi_n})$ relative to $\mathbf{q_{cm}}$ and $\mathbf{p_{cm}}$:

$$
\begin{cases}
\mathbf{q_{cm}} = \frac{1}{n} \sum_{i=1}^{n} \mathbf{q_i}, \\
\mathbf{p_{cm}} = \frac{1}{n} \sum_{i=1}^{n} \mathbf{p_i}, \\
\mathbf{r_i} = \mathbf{q_i} - \mathbf{q_{cm}}, \text{ for } i = 1, ..., n, \\
\boldsymbol{\pi_i} = \mathbf{p_i} - \mathbf{p_{cm}}, \text{ for } i = 1, ...n.
\end{cases}
\tag{5.6}
$$

The flow diagram of integration scheme for molecular dynamics simulation of hard spherocylinder system under isothermal-isobaric ensemble with a discrete time step Δt is given below. Let η be the velocity of the barostat, P_{int} be the internal pressure and P_{ext} be the external pressure, V be the volume of the rectangular box. Other variables in the scheme are discussed later.

Integration scheme of molecular dynamics in hard spherocylinder system under isothermal-isobaric ensemble

1. Propagate the thermostat for half time step $\Delta t/2$ according to

$$
\begin{cases}
\boldsymbol{\pi_i}(t + \Delta t/2) = c\boldsymbol{\pi_i}(t) + \sqrt{\frac{1-c^2}{\beta}}\zeta_i(t), \\
\boldsymbol{\omega_i}(t + \Delta t/2) = c\boldsymbol{\omega_i}(t) + \sqrt{\frac{(1-c^2)I}{\beta}}\hat{\zeta}_i(t),
\end{cases}
\tag{5.7}
$$

for $i = 1, ..., n$. For every N_p time steps, we propagate the barostat velocity η for half time step $\Delta t/2$ according to

$$
\eta(t + \Delta t/2) = c\eta(t) + \sqrt{\frac{1-c^2}{\beta W}}\bar{\zeta}(t).
\tag{5.8}
$$

2. Detect instant collisions and compute post-collision velocities by Eq. 5.4. Let $\boldsymbol{\pi_i^*}$ and $\boldsymbol{\omega_i^*}$ denote the post-collision velocities. If no collision occurs, then $\boldsymbol{\pi_i^*} = \boldsymbol{\pi_i}$ and $\boldsymbol{\omega_i^*} = \boldsymbol{\omega_i}$.

   For every N_p time steps, we compute the internal pressure P_{int} according to 5.12 and propagate the barostat velocity η for half time step $\Delta t/2$ according to

$$
\eta(t + \Delta t/2) = \eta(t) + \frac{3[V(P_{\text{int}} - P_{\text{ext}}) + 2\beta^{-1}]}{W}\frac{\Delta t}{2}.
\tag{5.9}
$$

3. Propagate positions $\mathbf{r_i}$ and orientations $\mathbf{u_i}$ for one time step Δt using the updated velocities $\boldsymbol{\pi_i^*}$ and $\boldsymbol{\omega_i^*}$ according to Eq. 5.3.

   Consider the entry-wise form $\boldsymbol{r_i} = (r_{i1}, r_{i2}, r_{i3})$ and $\boldsymbol{\pi_i} = (\pi_{i1}, \pi_{i2}, \pi_{i3})$. For every N_p time steps, we update the positions and translational velocities of the spherocylinders, and at the same time update the volume of the system for one time step Δt according to

$$
\begin{cases}
r_{ik}(t + \Delta t) = e^{\eta\Delta t}r_{ik}(t), \\
\pi_{ik}(t + \Delta t) = e^{-\eta\Delta t}\pi_{ik}(t), \\
V(t + \Delta t) = e^{2\eta\Delta t}V(t), \\
s(t + \Delta t) = e^{\eta\Delta t}s(t),
\end{cases}
\tag{5.10}
$$

for $k = 1, 2; i = 1, ..., n$.

4. Repeat step 2

5. Repeat step 1

In the integration scheme above, $c = e^{-\gamma \Delta t/2}$, γ is the friction coefficient, $\beta = \frac{1}{k_B T}$ is the inverse of temperature, W is the mass of the barostat. $\zeta_i(t)$, $\hat{\zeta}_i(t)$ are $2n$ independent vectors of standard normal random variables and $\bar{\zeta}(t) \in \mathbb{R}$ is a standard normal random variable. Furthermore, we introduce two parameters, the relaxation time of thermostat and barostat denoted by τ_T and τ_P, respectively. We use the parameters given in [25], $\tau_T = 0.2$ and $\tau_P = 0.5$. The variables in the integration scheme depending on these two parameters are the barostat mass $W = n\beta^{-1}\tau_P^2$ and the friction coefficient $\gamma = (2\tau_T)^{-1}$.

According to the virial equation [44], the internal pressure of the hard spherocylinder system is given by

$$P_{\text{int}} = \frac{1}{\beta}\frac{n}{V} + \frac{1}{3V}\left\langle \sum_{i<j}^{n} \vec{F}_{ij} \cdot \vec{c}_{ij} \right\rangle, \tag{5.11}$$

where $\vec{F}_{ij}$ is the force on the i-th spherocylinder exerted by the j-th spherocylinder, $\vec{c}_{ij} = \mathbf{r_i} - \mathbf{r_j}$ is their relative position, $\langle...\rangle$ indicating the equilibrium ensemble average. However, in the hard spherocylinder system, the pairwise force cannot be measured directly. Instead, we can measure the change of momentum for the i-th spherocylinder. The force then can be computed as the rate of change of momentum. Thus the internal pressure P_{int} [17] is given by

$$P_{\text{int}} = \frac{1}{\beta}\frac{n}{V} + \frac{1}{3VT_{ob}} \sum_{collision} \Delta\vec{p}_{ij} \cdot \vec{c}_{ij}, \tag{5.12}$$

where $\Delta\vec{p}_{ij}$ is the collision impulse given by Eq. 5.5 and T_{ob} is the total observation time for the change of momentum. In the integration scheme above, the term N_p is related to T_{ob} with $T_{ob} = N_p \times \Delta t$. In other words, we compute the internal pressure P_{int} for every N_p time steps and update the barostat velocity and volume of the system during the simulation.

In our study, we fixed the temperature $k_B T = 1.0$ and the pressure $P_{\text{ext}} = 6.0$. We place a total number of 2304 hard spherocylinders in the rectangular box. The height of the rectangular box is fixed at $b = 12.2$ during the simulation. We are able to get the coexistence of the isotropic phase and the nematic phase as shown in Fig. 5.1.

Next, we present some numerical results of the molecular dynamics simulations such as the minimum distance between the hard spherocylinders, internal pressure, temperature and volume of the system. Two different sets of parameters $N_p = 200, \Delta t = 0.005$ and $N_p = 1000, \Delta t = 0.001$ are used. As we discussed earlier, the spherocylinders overlap with each other when instant collision occurs. The minimum distance between any two spherocylinders should be greater or equal to the diameter of the spherocylinder ($D = 1$) theoretically. In Fig. 5.3, the minimum distance between overlapping spherocylinders is plotted against the number of steps, where each step represents a total number of N_p time steps. With a smaller discrete time step Δt, the minimum distance between the spherocylinders is closer to 1, which leads to the higher accuracy. In Fig. 5.6, it is observed that the volume $V \approx 8800$ for isotropic phase and $V \approx 7500$ for nematic phase. There is a small deviation of the volume V by using two different sets of parameters, which is considered not important in our study. It is also observed that the kinetic temperature fluctuates around $k_B T = 1.0$ and the internal pressure fluctuates around $P_{\text{int}} = 6.0$ as shown in Fig. 5.4 and Fig. 5.5. The internal pressure P_{int} is computed by Eq. 5.12. And the kinetic temperature is defined as

$$k_B T = \frac{1}{6n} \sum_{i=1}^{n} \left[|\boldsymbol{\pi_i}|^2 + I |\boldsymbol{\omega_i}|^2 \right]. \tag{5.13}$$

The dynamics of the pressure, temperature, volume are quite similar by using the two different sets of parameters Δt and N_p. So we choose the larger time step $\Delta t = 0.005$ and $N_p = 200$ to achieve better efficiency in the sacrifice of the higher accuracy.
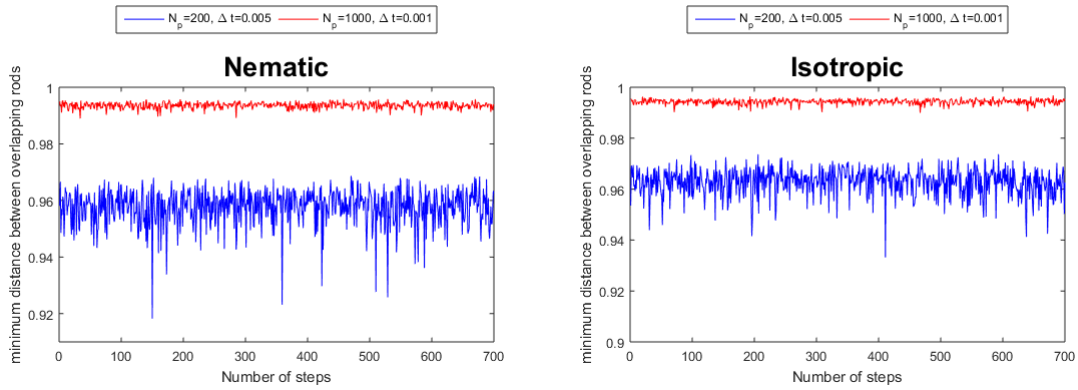
Figure 5.3: The minimum distance between the overlapping spherocylinders are plotted against the number of steps, each step represents a total number of N_p time steps. When $\Delta t = 0.001$, the minimum distance between overlapping spherocylinders is around 0.995. When the discrete time step Δt is increased to 0.005, the minimum distance decreases to around 0.96. The accuracy of the model decreases when a larger discrete time step is used.
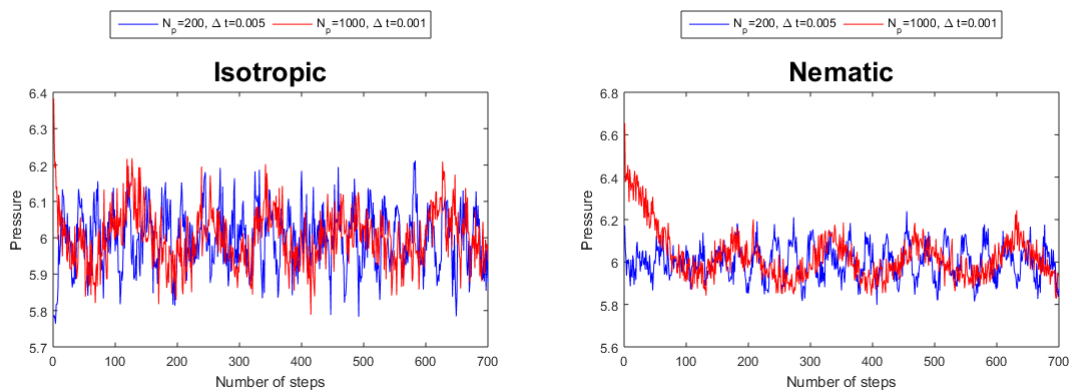
Figure 5.4: Dynamics of the internal pressure during the simulation. Each step represents a total number of N_p time steps. The pressure fluctuates around 6.0.
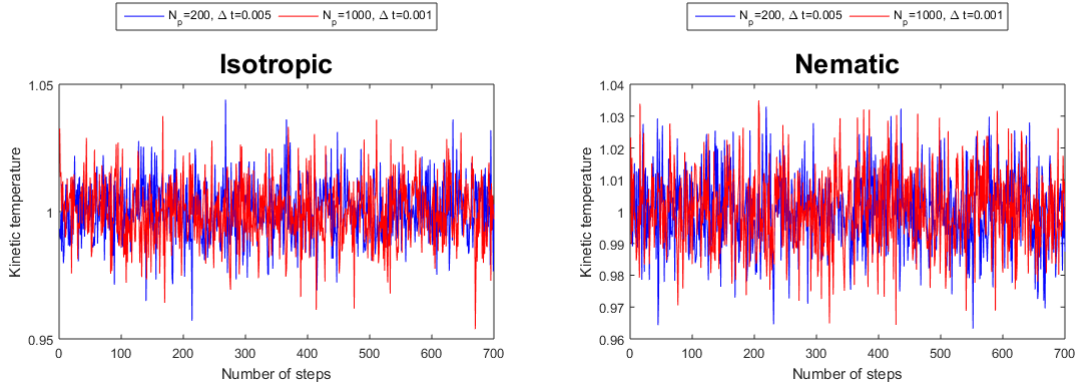
Figure 5.5: Dynamics of the kinetic temperature during the simulation. Each step represents a total number of N_p time steps. The kinetic temperature fluctuates around 1.0.
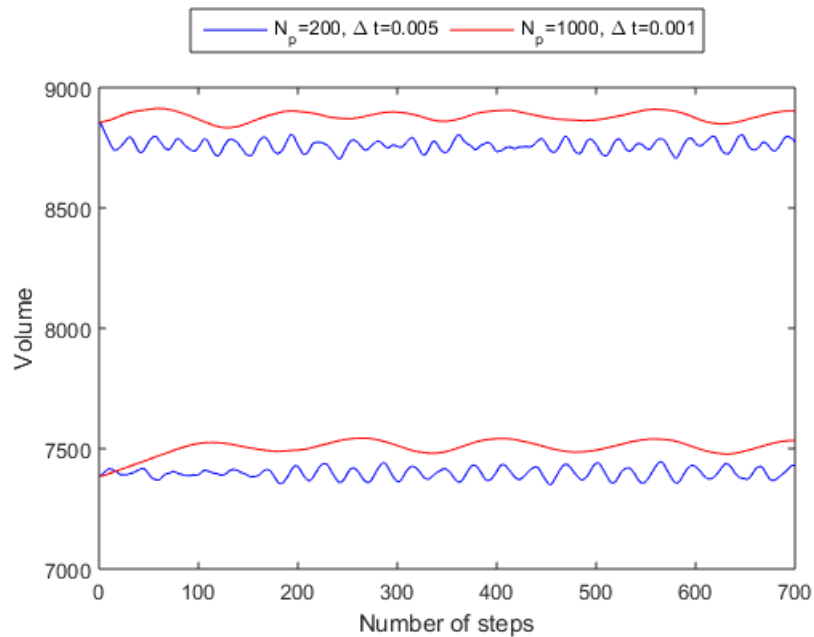
Figure 5.6: Dynamics of the volumes of the system corresponding to isotropic phase (curves at the top) and nematic phase (curves at the bottom) during the simulation, using different sets of parameters N_p and Δt. There is a small deviation using two different sets of parameters. In general, the volume of the isotropic phase is larger than the nematic phase.

5.2   Numerical Method

5.2.1   Orientational Order Parameters

The isotropic phase and the nematic phase can be characterized by an order parameter, which measures the nematic ordering of the system, i.e. the alignment of the spherocylinders in a common direction, the nematic direction $\hat{n}$. Usually, the order parameter S is defined as

$$S = \frac{3}{2} \int_0^\pi \cos^2 \theta g(\theta) \sin(\theta) d\theta - \frac{1}{2}, \tag{5.14}$$

where θ is the angle between the central axis of the spherocylinder and the nematic direction. $g(\theta)$ is the equilibrium orientation distribution function. In practice, the nematic direction is not known beforehand. Thus the orientation distribution $g(\theta)$ cannot be measured directly. Instead, the nematic direction is associated with the following 3 by 3 matrix Q, whose (i,j) entry is given by

$$Q_{ij} = \frac{1}{n} \left(\sum_{k=1}^n \frac{3}{2} u_{ki} u_{kj} \right) - \frac{1}{2} \delta_{ij}, \tag{5.15}$$

where n is the total number of spherocylinders, the vector $\mathbf{u_k} = (u_{k1}, u_{k2}, u_{k3})$ is the unit vector representing the central axis of the k-th spherocylinder. The nematic direction is given by the eigenvector associated with the largest eigenvalue of the matrix Q.

In our study, we make a strong assumption by fixing the nematic direction $\hat{n} = (0, 0, 1)^T$ in advance. We define a new order parameter $\hat{S}$, which measures the average alignment of spherocylinders in the nematic direction given by

$$\hat{S} = \frac{1}{n} \sum_{k=1}^n | \langle \mathbf{u_k}, \hat{n} \rangle |. \tag{5.16}$$

Based on this choice of order parameter, the nematic phase in our study refers to the system in which all the spherocylinders are aligned in the direction $(0, 0, 1)^T$. The study of the hard spherocylinder system using the usual order parameter S by Eq. 5.14 will be postponed to the future.

5.2.2 Collective Variables and Restrained Potential

The rectangular box containing the spherocylinders is partitioned into N small bins $B_1, ..., B_N$, each of size $l \times l \times b$ as shown in Fig. 5.7. We introduce N collective variables $\theta(q, u) = (\theta_1(q, u), ..., \theta_N(q, u))$, where $q = (\mathbf{q_1}, ..., \mathbf{q_n})$ and $u = (\mathbf{u_1}, ..., \mathbf{u_n})$ are the centers and unit vectors representing the central axes of the spherocylinders, respectively. The collective variable $\theta_i(q, u)$ measures the average alignment of spherocylinders in the bin B_i with respect to the nematic direction $\hat{n} = (0, 0, 1)^T$ given by

$$\theta_i(q, u) = \frac{1}{n_i} \sum_{\mathbf{q_j} \in B_i} |\langle \mathbf{u_j}, \hat{n} \rangle|, \tag{5.17}$$

where n_i is the number of spherocylinders in the bin B_i. The collective variable $\theta_i(q, u)$ ranges from 0 to 1. In the nematic phase where all the spherocylinders are aligned in the nematic direction, the collective variables are close to 1. While in the isotropic phase where the spherocylinders are randomly distributed and oriented, the collective variables are close to 0.5. In Fig. 5.7, we use a molecular configuration to illustrate the collective variables. A clear isotropic-nematic interface is observed in the molecular configuration (upper panel). The spherocylinders are randomly oriented at the top and bottom over the x, y plane and well aligned in the middle. In the collective variable configuration, it is shown by the green region ($\theta \approx 0.5$) and the yellow region ($\theta \approx 1$) (lower panel) correspondingly.

For the implementation of the on-the-fly string method, we use the restrained molecular dynamics which constrains the system at $\theta(q, u) = z$, where $\theta(q, u)$ is the current value of the collective variables and z is the target value. It is realized by adding the following restrained potential to the Hamiltonian of the original system given by

$$V_{res}(q, u) = \frac{\kappa}{2} \sum_{i=1}^{N} (\theta_i(q, u) - z_i)^2. \tag{5.18}$$

In the computation, we use $\kappa = 10^4$. The gradient of the restrained potential to $\mathbf{u_j}$

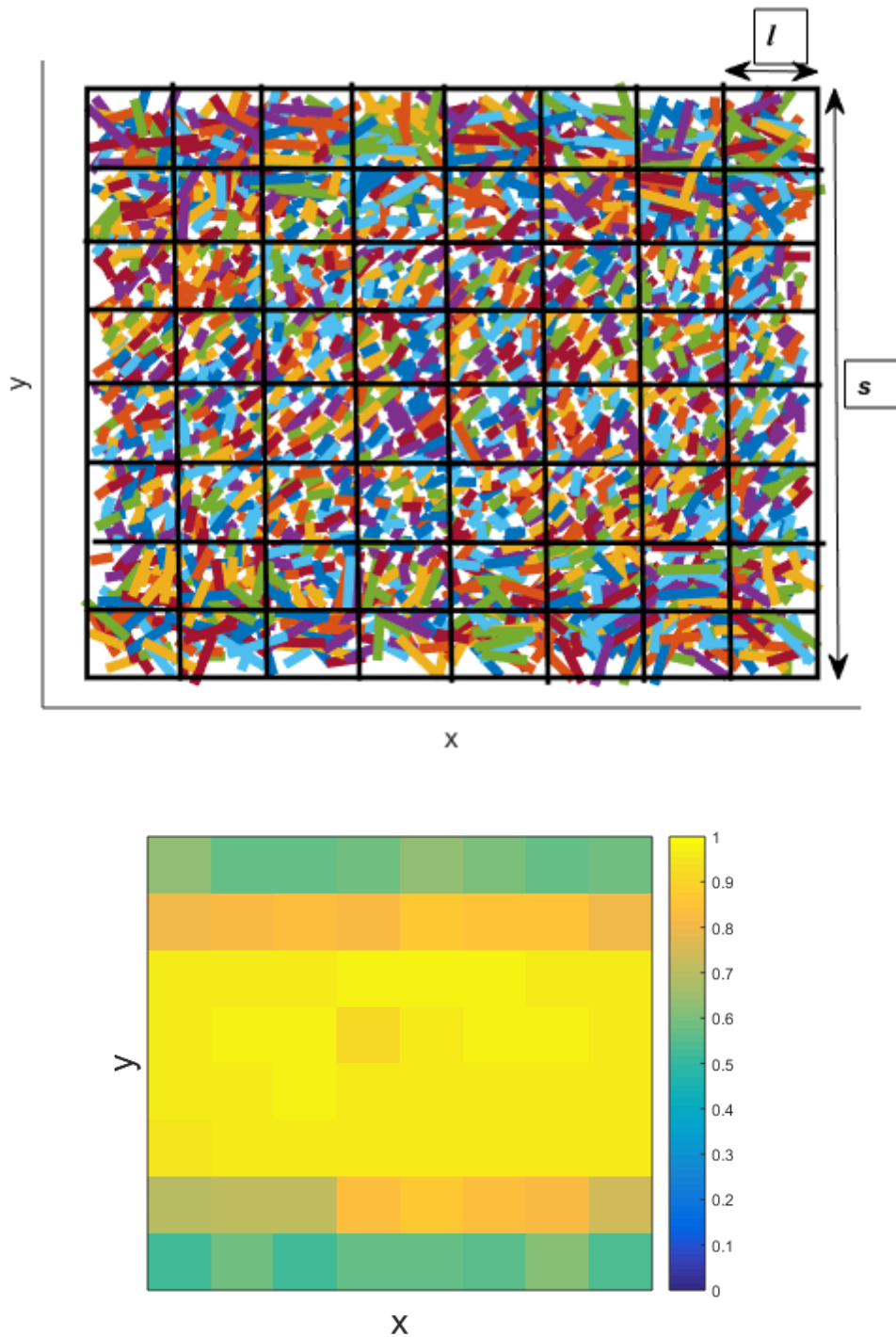Figure 5.7: The partition of the rectangular box into 8 by 8 small bins each of size $l \times l \times b$, where $l = s/8$. The configuration of the collective variables are shown in the lower panel. In the green region, the collective variables are close to 0.5 corresponding to the isotropic phase. In the yellow region, the collective variables are close to 1.0 corresponding to the nematic phase.

is given by

$$
\begin{aligned}
\nabla_{\mathbf{u_j}} V_{res}(q, u) &= \kappa \sum_{i=1}^{N} \left(\theta_i(q, u) - z_i \right) \nabla_{\mathbf{u_j}} \theta_i(q, u) \\
&= \kappa \sum_{i=1}^{N} [\left(\theta_i(q, u) - z_i \right) \hat{n} \times \mathrm{sgn}(\langle \hat{n}, \mathbf{u_j} \rangle) \times \tfrac{1}{n_i} \times I_{B_i}(\mathbf{q_j})],
\end{aligned}
\tag{5.19}
$$

where $I_{B_i}(\mathbf{q_j}) = \begin{cases} 1, & \text{if } \mathbf{q_j} \in B_i, \\ 0, & \text{otherwise.} \end{cases}$

To implement this restrained potential force in the simulation, firstly we recall the integration scheme of molecular dynamics under isothermal-isobaric ensemble discussed in subsection 5.1.2. The restrained potential force $-\nabla_{\mathbf{u_j}} V_{res}(q, u)$ is applied in step 2 and 4. After updating the post-collision velocities $\boldsymbol{\pi}_j^*$ and $\boldsymbol{\omega}_j^*$, we propagate the angular velocity $\boldsymbol{\omega}_j^*$ for half time step $\Delta t/2$ according to

$$
\boldsymbol{\omega}_j(t + \Delta t/2) = \boldsymbol{\omega}_j^* - \left(\mathbf{u_j} \times \nabla_{\mathbf{u_j}} V_{res}(q, u) \right) \frac{\Delta t}{2}.
\tag{5.20}
$$

5.2.3 Implementation of the On-the-fly String Method

For the implementation of the on-the-fly string method, an initial string $z(\alpha)$, $\alpha \in [0, 1]$ is constructed in the collective variable space, connecting the isotropic phase and the nematic phase. The string $z(\alpha)$ is parametrized by its normalized arc length α. As discussed previously, let $z(0) \equiv 0.5$ for the isotropic phase and $z(1) \equiv 1.0$ for the nematic phase. For the construction of the intermediate points along the initial string, we make the following assumptions. During the isotropic-nematic phase transition, a nematic nucleus is formed and grows. After the critical nucleus is formed, the entire system will evolve to the nematic phase. We assume the alignment of the spherocylinders starts at the center of the x, y plane and the nematic nucleus formed at the center of the x, y plane is spherical-like. In the collective variable space, this is described by the increments of the collective variables starting at the center followed by the expansion towards the entire collective variable space. A schematic presentation of the intermediate points along the initial string is shown in Fig. 5.8.
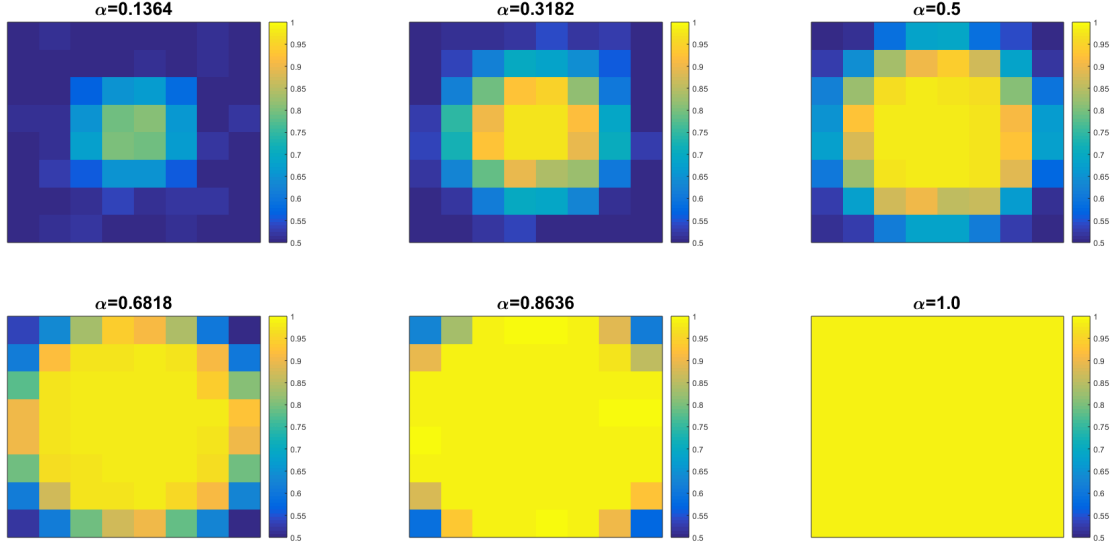
Figure 5.8: The intermediate points along the initial string. The increment of the collective variables starts at the center followed by the expansion to the entire domain.

In the computation, the string is discretized into $R+1$ images $\{z^0, z^1, ..., z^R\}$ uniformly distributed along the string, where z^m is the image at $\alpha = m/R$ for $m = 0, ...R$. We use $R = 22$ in practice. Each image z^m is assigned an MD replica (q^m, u^m). With abuse of notation, let $(q^m, u^m) = x^m$. Let x_{iso} be the molecular configuration of the isotropic phase. At the beginning, we set $x^m = x_{iso}$ for all $m = 0, 1, ..., R$. It is obvious that x^m is not well constrained at $\theta(x^m) = z^m$ for $m = 1, ..., R$. In order to make the MD replicas constrained at the corresponding images, we run the restrained molecular dynamics mentioned in subsection 5.2.2 for 20000 time steps with a discrete time step $\Delta t = 0.005$. For example in Fig. 5.9, the MD replica x^9 is well constrained at the image z^9, i.e. $\theta(x^9) = z^9$.

Let z_k^m and x_k^m be the instantaneous position of the image z^m and the corresponding MD replica x^m at the k-th iteration during the string evolution. We update the discretized string with a discrete time step $\Delta t = 0.005$ using the on-the-fly string method according to the following 3 steps:
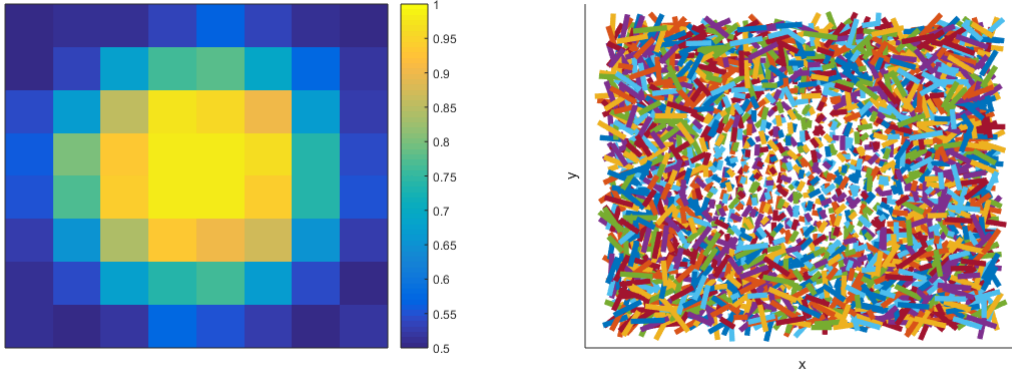
Figure 5.9: Configuration of the image z^9 (left) and the corresponding MD replica x^9 (right) along the initial string. It is shown that the MD replica x^9 is well constrained at $\theta(x^9) = z^9$.

1. Concerted evolution of the discretized string and the corresponding MD replicas at the k-th iteration by

$$
\begin{cases}
z^{m,*} = z_k^m - \frac{\kappa}{\gamma_z} \bar{F}(z_k^m, x_k^m)\Delta t \text{ for } m = 0, 1, ..., R, \\
x_{k+1}^m = \text{starting from } x_k^m, \text{ run the restrained molecular dynamics} \\
\text{discussed in subsection 5.2.2 for one time step } \Delta t \text{ for } m = 0, 1, ..., R,
\end{cases}
$$
(5.21)

   where $\bar{F}(z_k^m, x_k^m) = M(x_k^m)\left(z_k^m - \theta(x_k^m)\right)$, M is the tensor matrix given by Eq. 5.22, $\gamma_z = 500$ and $\kappa = 10^4$. We get a new set of images $\{z^{0,*}, ..., z^{R,*}\}$.

2. Interpolate a curve through the images $\{z^{0,*}, ..., z^{R,*}\}$ using linear interpolation. Then distribute $R + 1$ new images uniformly along the interpolated curve according to the equal arc length parametrization to obtain the string $\{z_{k+1}^0, z_{k+1}^1, ..., z_{k+1}^R\}$ at the new iteration.

3. Go to step 1 or stop when the string reaches the steady state.

In the step 1, the (i, j) th entry of the tensor matrix M is given by

$$
\begin{aligned}
M_{ij} &= \sum_{l=1}^{n} \langle \nabla_{\mathbf{u_l}} \theta_i(q, u), \nabla_{\mathbf{u_l}} \theta_j(q, u) \rangle \\
&= \sum_{l=1}^{n} \frac{1}{n_i n_j} I_{B_i}(\mathbf{q_l}) I_{B_j}(\mathbf{q_l}) \\
&= \begin{cases} \frac{1}{n_i} & \text{if } i = j, \\ 0 & \text{if } i \neq j. \end{cases}
\end{aligned} \tag{5.22}
$$

Note that the tensor matrix M depends on the number of spherocylinders in each small bin. Since all the bins are of the same size, so we assume $n_i = n_j$ for all $i \neq j$. Under this assumption, the tensor matrix M becomes a multiple of identity matrix I. We simply take $M = I$ in our simulation.

The string converges to the MFEP connecting the isotropic phase and the nematic phase when it reaches the steady state, which corresponds to the most probable transition pathway for the isotropic-nematic phase transition. The free energy profile is computed along the MFEP by thermodynamic integration. The saddle point can be identified from the maximum of the free energy along the MFEP. From the saddle point, we can determine the transition state. At last, we test the committor value distribution at the saddle point and its neighbouring images along the MFEP.

5.2.4   System with an External Aligning Field

An external aligning field influences the isotropic-nematic phase transition in the hard spherocylinder system. The external aligning field in our study makes the system prefer the nematic phase rather than the isotropic phase. It can be realized by adding the following additional potential U_{ext} to the Hamiltonian of the original system given by

$$
U_{ext}(u) = \frac{\beta}{2} \sum_{i=1}^{n} \left(|\langle \hat{n}, \mathbf{u_i} \rangle| - 1 \right)^2, \tag{5.23}
$$

where $\beta > 0$ describes the strength of the external aligning field. The gradient of this additional potential to the unit vector $\mathbf{u_j}$ is given by

$$\nabla_{\mathbf{u_j}} U_{ext} = \beta(|\langle \hat{n}, \mathbf{u_j} \rangle| - 1) \times \text{sgn}(\langle \hat{n}, \mathbf{u_j} \rangle)\hat{n}. \tag{5.24}$$

To implement the additional potential, firstly we recall the integration scheme of the molecular dynamics under the isothermal-isobaric ensemble discussed in subsection 5.1.2. We apply the potential force $-\nabla_{\mathbf{u_j}} U_{ext}$ in step 2 and 4. After updating the post-collision velocities $\boldsymbol{\pi}_j^*$ and $\boldsymbol{\omega}_j^*$, we propagate the angular velocities $\boldsymbol{\omega}_j^*$ for half time step $\Delta t/2$ according to

$$\boldsymbol{\omega}_j(t + \Delta t/2) = \boldsymbol{\omega}_j^* - \left(\mathbf{u_j} \times \nabla_{\mathbf{u_j}} U_{ext}\right)\frac{\Delta t}{2}. \tag{5.25}$$

5.3 Results and Discussion

In the computation, the string is discretized into 23 images $z^0, z^1, ..., z^{22}$ uniformly distributed along the string. The string is evolved according to Eq. 5.21 with a discrete time step $\Delta t = 0.005$. Let z_n^k be the instantaneous position of image z^k at the n-th iteration. The evolution of the string is monitored by the distance $D(n)$ between the string and its initial condition given by

$$D(n) = \sum_{k=0}^{22} |z_n^k - z_0^k|_1. \tag{5.26}$$

Firstly, we determine the MFEP for the isotropic-nematic phase transition under the effect of external aligning field with $\beta = 0.8$. Then we use this MFEP as the initial string to implement the on-the-fly string method for the system without the external aligning field, i.e. $\beta = 0$. The strings finally reach the steady state in both cases as shown in Fig. 5.10.

The string converges to the MFEP at the steady state, which corresponds to the most probable transition path for the isotropic-nematic phase transition. The images along the MFEP for the system without the external aligning field ($\beta = 0$)
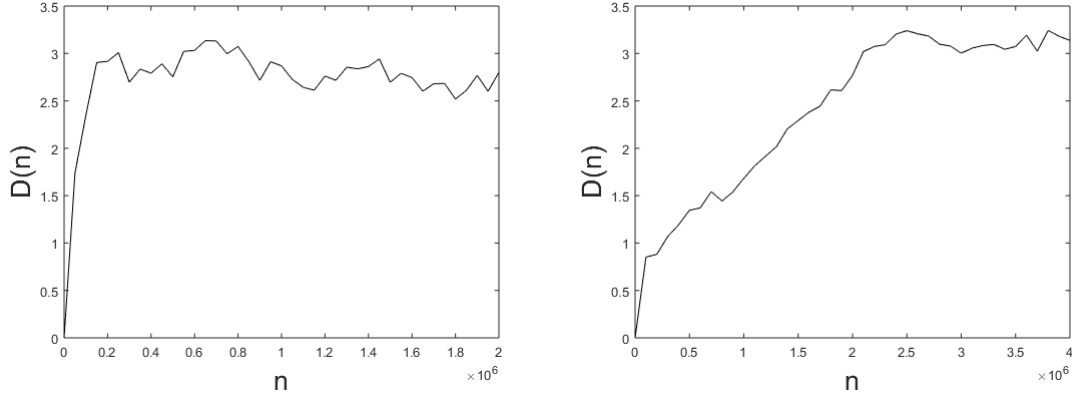
Figure 5.10: Distance $D(n)$ of the string from its initial condition during the string evolution. The system without the external aligning field ($\beta = 0$) on the left and with the external aligning field ($\beta = 0.8$) on the right. The string reaches the steady state in both cases.

are shown in Fig. 5.11. The corresponding MD replicas along the MFEP are shown in Fig. 5.12. It is observed that the alignment of the spherocylinders starts in the middle region along the y-axis, and a rectangular nematic nucleus is formed. This is different from our original assumption that the nematic nucleus is spherical like. It looks like that the nematic nucleus becomes more stable when connected at the periodic boundaries.

The free energy profile along the MFEP is shown in Fig. 5.17. In case of $\beta = 0$ (curve marked by circles), the free energy attains the maximum somewhere between the images z^7 and z^8. So we conclude that the saddle point is between z^7 and z^8. The corresponding MD replicas x^7 and x^8 are shown in Fig. 5.13. From x^7 to x^8, the spherocylinders rearrange themselves such that a multilayer structure is formed. We also present the volumes of the corresponding MD replicas along the MFEP in Fig. 5.14. A sudden decrease of the volume occurs at the transition state. In other words, the compression of the volume and the formation of the critical nucleus with a multilayer structure happen simultaneously.

For the system with the external aligning field ($\beta = 0.8$), the MFEP is almost the same as shown in Fig. 5.15 except that the starting image has collective variables close to 0.6. At the transition state, the critical nucleus also has a multilayer

structure as shown in Fig. 5.16. Furthermore, the external aligning field lowers the free energy barrier for the isotropic-nematic phase transition, see Fig. 5.17. In other words, the nucleation process during the isotropic-nematic phase transition is enhanced by the external aligning field.

For the system without the external aligning field ($\beta = 0$), to further verify the transition state is located between z^7 and z^8 along the MFEP, we generate configurations from the phase space (q, u) restricted to the isocommittor surfaces at the images z^6, z^7, z^8 and z^9. As discussed in chapter 2, the isocommittor surface can be approximated locally by the hyperplane $P(\alpha_s)$ tangent to the isocommittor surface at the given point $z(\alpha_s)$. The equation for the hyperplane $P(\alpha_s)$ is given by

$$\langle \tilde{n}, \theta(q, u) - z(\alpha_s) \rangle = 0, \tag{5.27}$$

where $\tilde{n}$ is the unit normal vector to the hyperplane $P(\alpha_s)$ given by $\tilde{n} = \frac{M(z(\alpha_s))^{-1} \tau_{\alpha_s}}{|M(z(\alpha_s))^{-1} \tau_{\alpha_s}|}$. Since we assume $M(z) \equiv I$, the unit normal vector $\tilde{n} = \tau_{\alpha_s}/|\tau_{\alpha_s}|$, where τ_{α_s} is the tangent vector of the string at the point $z(\alpha_s)$.

To generate the samples of configurations from the hyperplane $P(\alpha_s)$ in practice, we add the following restrained potential to the Hamiltonian of the original system:

$$V_{\kappa,\alpha_s}(q, u) = \frac{\kappa}{2} \langle \tilde{n}, \theta(q, u) - z(\alpha_s) \rangle^2, \tag{5.28}$$

where κ is chosen large to make sure the samples are well constrained on the hyperplane. We generate 30 samples from the hyperplane $P(\alpha_s)$. And from each sample, we generate 30 different trajectories by assigning random initial velocities. The committor value is given by the probability that the trajectory will evolve to the nematic phase first rather than the isotropic phase. It is observed that the committor functions are almost zero for the images z^6 and z^7 and almost one for the images z^8 and z^9. It is also observed that almost all the samples on the hyperplane at z^8 and z^9 consist of a nematic nucleus with a multilayer structure. Thus, we conclude that the formation of a multilayer structure is a crucial step to form the critical nucleus for the isotropic-nematic phase transition.

However, we cannot determine the isocommittor 1/2 surface. This may be due to the limitation of the order parameter used in the problem. The order parameter $\hat{S}$ in our study is defined under the assumption of a prescribed nematic direction. But in reality, the nematic direction of the system is usually unknown. Thus the usual definition of the order parameter S given by Eq. 5.14 should be a better choice for the collective variables.

5.4 Conclusion

We numerically study the isotropic-nematic phase transition in the hard spherocylinder system using the on-the-fly string method. The hard spherocylinder system is modelled by molecular dynamics, where the spherocylinders interact with each other via collisions. We introduce an order parameter to characterize the isotropic and nematic phase of the hard spherocylinder system. The order parameter is chosen as the collective variable and the phase transition is studied on the free energy landscape in the collective variable space. The transition states, free energy barriers and MFEP are determined using the on-the-fly string method. It is seen that at the transition state, the critical nematic nucleus has a multilayer structure. Furthermore, the external aligning field lowers the free energy barrier, thus enhances the nucleation process during the isotropic-nematic phase transition.

However, our formulation of the problem has several drawbacks. Firstly, the model is studied in an extended two dimensional space which is not in the real three dimensional space. Secondly, the orientational order parameter is defined under the assumption of a prescribed nematic direction which is usually unknown. The problem becomes more complicated, but closer to the reality if we take these drawbacks into account. It is worth for further studies since it is very closely related to the colloidal materials in nature. There are two questions yet to be answered: (1) how layer structure is formed during the phase transition and (2) impacts of the shape of the simulation box on the structure of the critical nematic nucleus in the

Figure 5.11: The images along the MFEP for the system without the external aligning field, i.e. $\beta = 0$. According to the free energy profile along the MFEP in Fig. 5.17, the saddle point is between z^7 and z^8.

real three dimensional space. To tackle these two problems, one possible way is to choose the global order parameter S given by Eq. 5.14 and the flexible simulation box as the collective variables. To observe how the layer structure is formed, we need to study the system with a large number of particles. The problem becomes quite challenging.
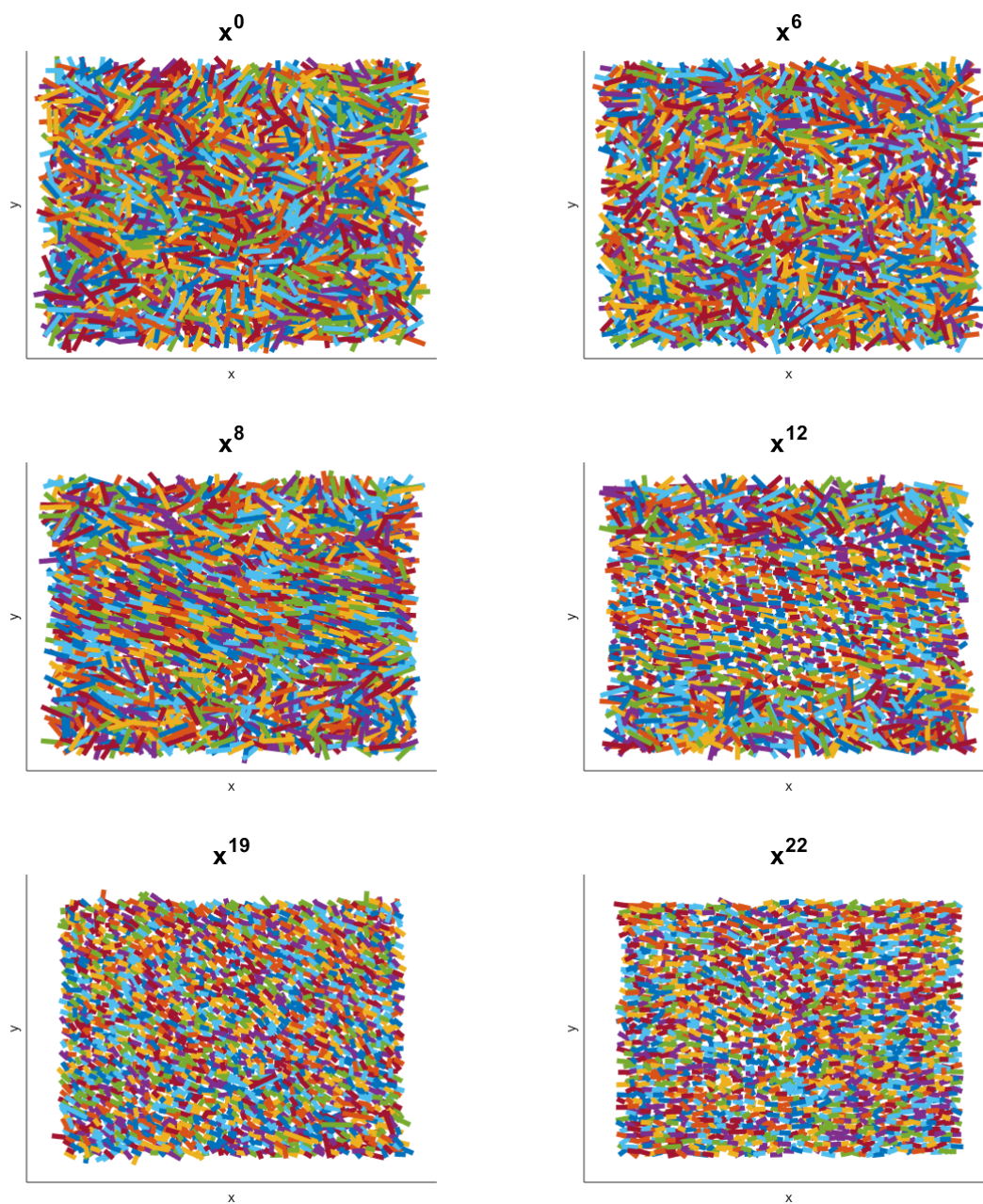
Figure 5.12: MD replicas corresponding to the images along the MFEP in Fig. 5.11

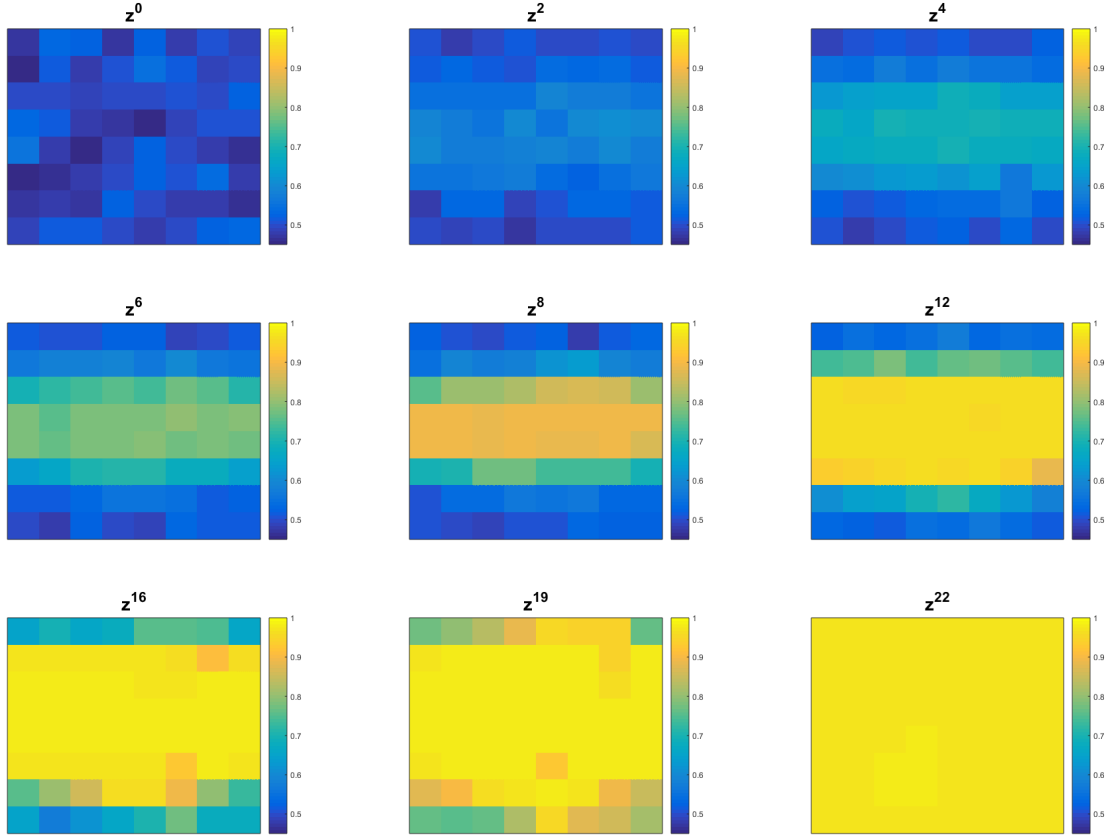Figure 5.13: The side view of the MD replicas x^7 and x^8 along the MFEP for the system without the external aligning field, i.e. $\beta = 0$. According to the free energy profile along the MFEP in Fig. 5.17 (marked by open circles), the transition state corresponds to the critical nucleus with a multilayer structure.
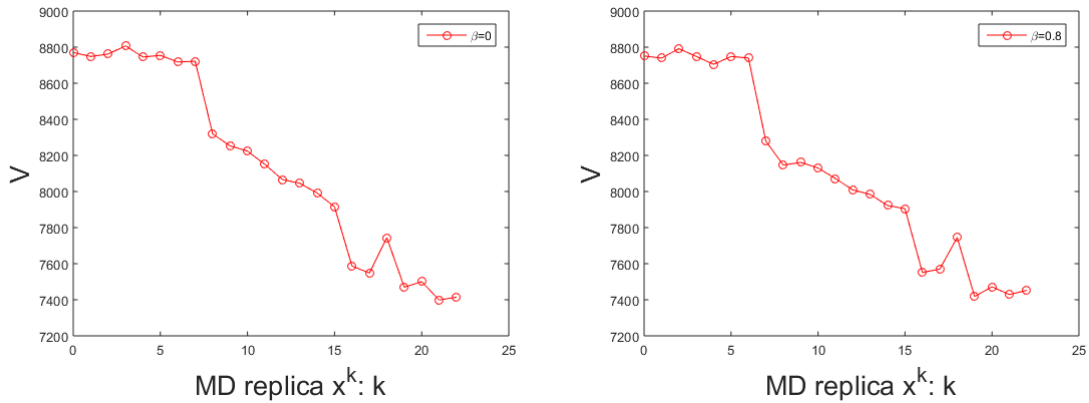
Figure 5.14: The volume V of the MD replicas along the MFEP for the system without the external aligning field $\beta = 0$ (left) and with the external aligning field $\beta = 0.8$ (right). $V \approx 8800$ at the isotropic phase and $V \approx 7400$ at the nematic phase. The volume V has a decreasing trend along the MFEP. There is a sudden decrease of the volume V at x^8 for $\beta = 0$ and at x^7 for $\beta = 0.8$, which corresponds to the transition state in each case.
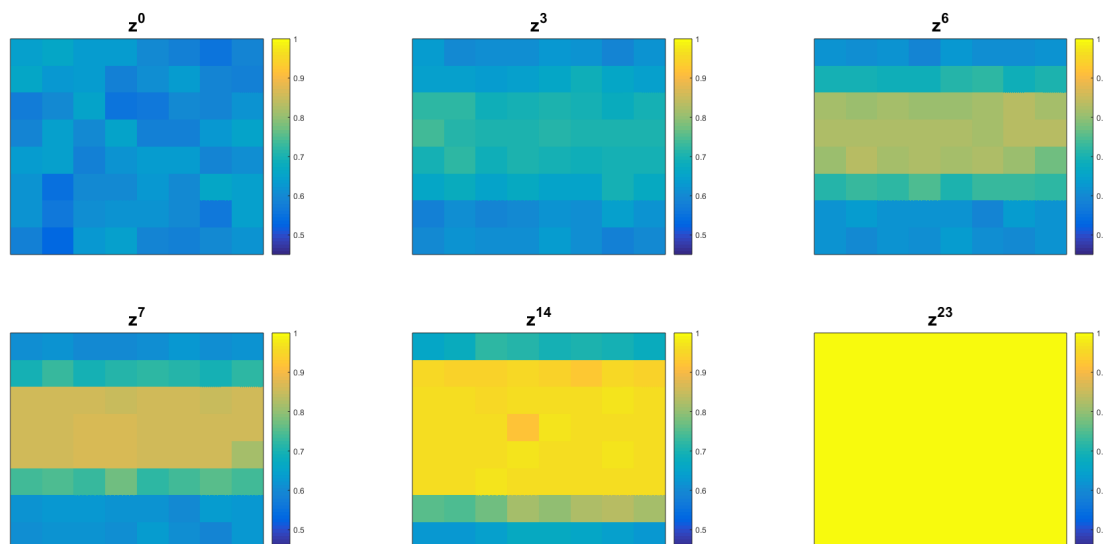
Figure 5.15: Images along the MFEP for the system with the external aligning field $\beta = 0.8$.
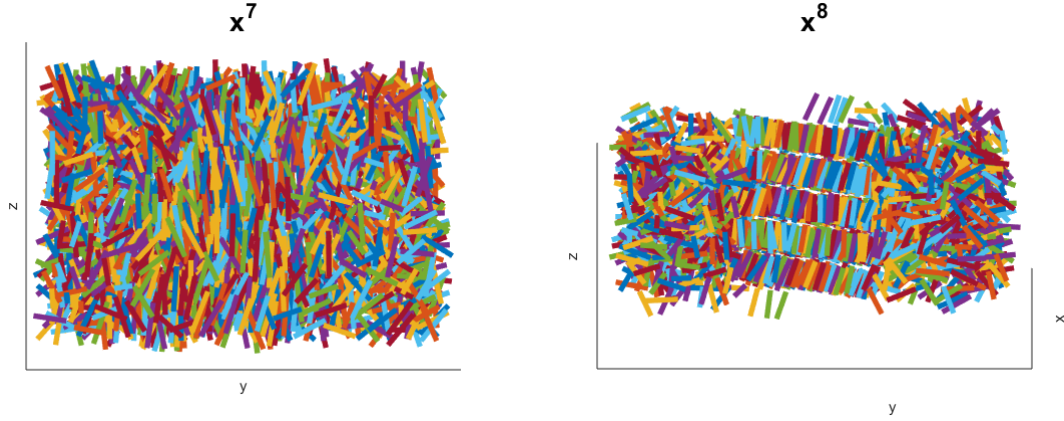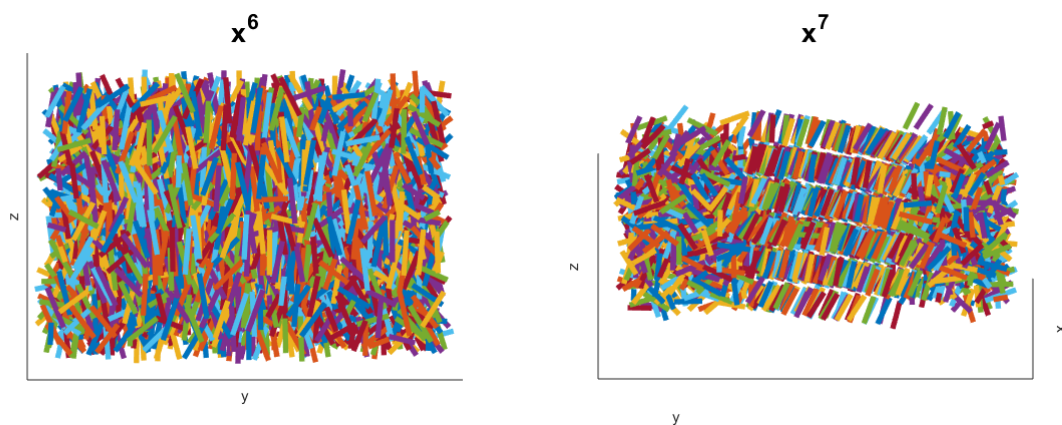

Figure 5.16: The side view of the MD replicas x^6 and x^7 along the MFEP with the external aligning field for $\beta = 0.8$. According to the free energy profile in Fig. 5.17 (marked by cross), the transition state corresponds to the critical nucleus with a multilayer structure.
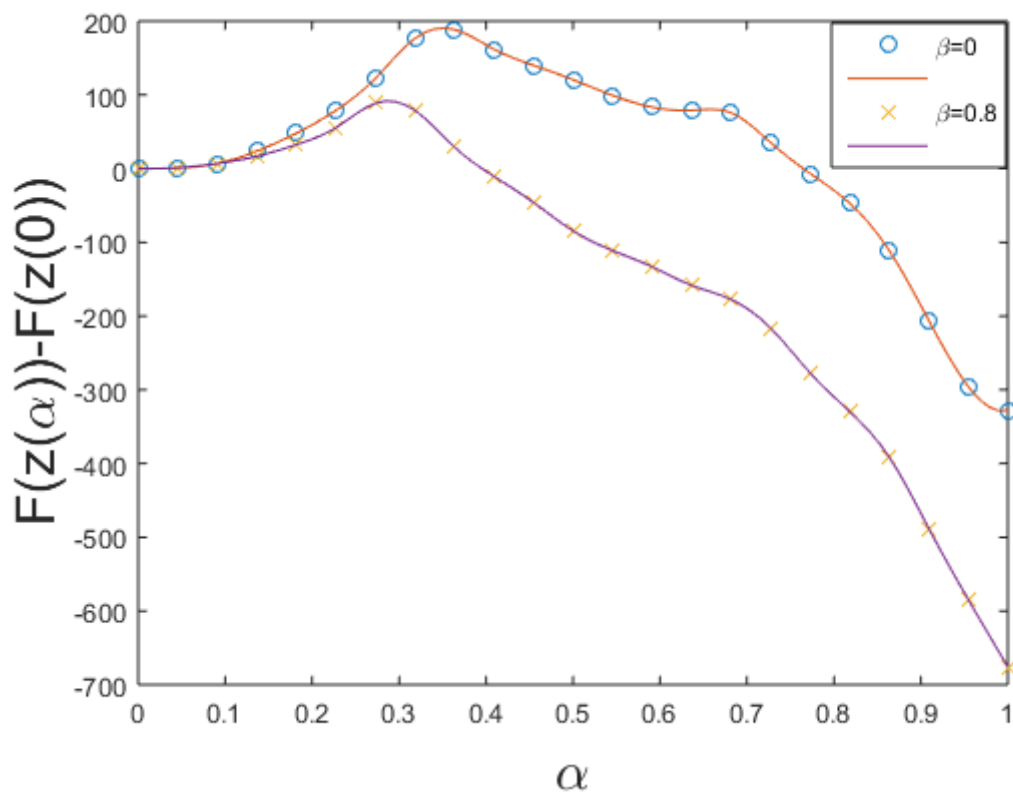
Figure 5.17: The free energy profile along the MFEP without external aligning field $\beta = 0$ and with external aligning field $\beta = 0.8$, respectively. The free energy barrier is lowered under the effects of an external aligning field.

Chapter 6

Conclusion

In this thesis, we applied the string method and its extensions to study different phase transition problems using different mathematical models. The problems are arranged in the order of increasing complexities, which demonstrates the string method as a powerful tool in studying phase transition problems even with high complexities.

Firstly, based on the string method in collective variables, we developed the climbing string method in collective variables focusing on the study of saddle points on the free energy landscape. Secondly, we studied three different phase transition problems using the string method and its extensions.

In the first problem, we numerically study the vapor condensation on the hydrophobic surfaces patterned with microstructures using a phase field model. The system consists of a two-phase fluid on a solid substrate modelled by the density field of fluid. The potential energy of the system is expressed as a functional of the density field. The two local minima of the potential energy correspond to the vapor phase and liquid phase respectively. Starting from the vapor minimum, we determine the saddle point using the climbing string method, which corresponds to the critical nucleus formed during vapor condensation. At the same time, we determine the minimum energy path (MEP) which corresponds to the formation and growth

of the vapor condensate. Two different nucleation scenarios are observed: in case of high pillar, narrow interpillar spacing, low supersaturation level and low surface wettability, the critical nucleus exhibits the Cassie state, in which the vapor condensate is suspended with air trapped inside the microstructures; otherwise it exhibits the Wenzel state, in which the vapor condensate penetrates the microstructures. The effects of different pillar structures, surface wettabilities and supersaturation level on the nucleation process are investigated. The critical value of pillar height, interpillar spacing and supersaturation level at which the critical nuclei changes from the Cassie state to the Wenzel state are identified from the phase diagram. It is observed that the critical value for the interpillar spacing follows closely to the critical radii in the homogeneous nucleation. Furthermore, the relaxation dynamics of the vapor condensate after the critical nuclei is computed using steepest descent dynamics. It is observed that the vapor condensate initially at the Cassie state will evolve to the Wenzel state during the relaxation in case of low pillar or wide interpillar spacing.

In the second problem, we study the Wenzel-to-Cassie transition of a liquid droplet on a grooved solid surface. The system is modelled by molecular dynamics, where the particles interact via Lennard-Jones potential. The molecular dynamics is governed by the Langevin dynamics described by a stochastic differential equation. Thus the corresponding energy landscape is very rough, and the model becomes more complicated than the phase field model discussed in the previous problem. To overcome this difficulty, we choose the coarse-grained density of fluid particles as the collective variables, and study the phase transition on the free energy landscape mapped in the collective variable space. As a major contribution of this thesis, we give a detailed mathematical formulation for the coarse-grained density of fluid particles as the collective variables. The transition state, free energy barrier and minimum free energy path (MFEP) are determined using the on-the-fly climbing string method. The MFEP corresponds to the pathway for the dewetting process from the Wenzel state to the Cassie state. It is observed that the dewetting process starts at the two bottom corners of the groove. At the transition state, the liquid

droplet is completely detached from the bottom solid surface and a symmetric liquid meniscus is formed inside the groove.

In the last problem, we study the isotropic-nematic phase transition in the hard spherocylinder system. The system is modelled by molecular dynamics, where the hard spherocylinders interact with each other via collisions. The corresponding energy landscape of the system is discontinuous, thus the problem becomes more complicated. The isotropic phase and nematic phase can be characterized by an order parameter which measures the nematic ordering of the system, i.e. the alignment of the spherocylinders to the nematic direction. In our study, we fix the nematic direction in advance. The order parameter by our definition measures the average alignments of the spherocylinders with respect to the prescribed nematic direction. We choose the order parameter as the collective variable and study the phase transition on the free energy landscape mapped in the collective variable space. The transition states, free energy barriers and MFEP are determined using the on-the-fly string method. It is observed that at the transition state, the critical nematic nucleus has a multilayer structure. Furthermore, we describe the hard spherocylinder system under the effects of an external aligning field. It is observed that the free energy barrier for the isotropic-nematic phase transition is lowered with the external aligning field, thus the nucleation process is enhanced.

Bibliography

[1] ALLEN, M. P.; FRENKEL, D.; TALBOT, J. *Molecular dynamics simulation using hard particles.* Comp. Phys. Rep. 9, 301 (1989).

[2] AUER, S.; FRENKEL, D. *Line tension controls wall-induced crystal nucleation in hard-sphere colloids.* Phys. Rev. Lett. 91, 015703 (2003).

[3] BAI, D.; CHEN, G.; ZHANG, X.; WANG, W. *Microsecond molecular dynamics simulations of the kinetic pathways of gas hydrate formation from solid surfaces.* Langmuir 27, 5961 (2011).

[4] BAUS, M. *Observation, Prediction and Simulation of Phase Transitions in Complex Fluids.* NATO ASI series C, Mathematical and Physical Sciences, Vol. 460, 1389 (1995).

[5] BOLHUIS, P.; FRENKEL, D. *Tracing the boundaries of hard spherocylinders.* J. Chem. Phys. 106, 666 (1997).

[6] BORCIA, R.; BORCIA, I. D.; BESTEHORN, M. *Drops on an arbitrarily wetting substrate: A phase field description.* Phys. Rev. E 78, 066307 (2008).

[7] BORMASHENKO, E. A. *Wetting of Real Surfaces.* Walter de Gruyter: Hawthorne, New York, 2013.

[8] CACCIUTO, A.; AUER, S.; FRENKEL, D. *Breakdown of classical nucleation theory near isostructural phase transitions.* Phys. Rev. Lett. 93, 166105 (2004).

[9] CASSIE, A. B. D.; BAXTER, S. *Wettability of porous surfaces.* Trans. Faraday Soc. 40, 546 (1944).

[10] DAOUD, W. A. (ED.) *Self-Cleaning Materials and Surfaces: A Nanotechnology Approach.* Wiley: New York, 2013.

[11] DARVE, E.; POHORILLE, A. *Calculating free energies using average force.* J. Chem. Phys. 115, 9169 (2001).

[12] DE GENNES, P. G.; BROCHARD-WYART, F.; QUÉRÉ, D. *Capillarity and Wetting Phenomena: Drops, Bubbles, Pearls, Waves.* Springer: New York, 2003.

[13] E, W.; REN, W.; VANDEN-EIJNDEN, E. *Energy landscape and thermally activated switching of submicron-sized ferromagnetic elements.* J. Appl. Phys. 93, 2275 (2003).

[14] E, W., REN. W.; VANDEN-EIJNDEN, E. *Simplified and improved string method for computing the minimum energy paths in barrier-crossing events.* J. Chem. Phys. 126, 164103 (2007).

[15] E, W.; REN, W.; VANDEN-EIJNDEN, E. *String method for study of rare events.* Phys. Rev. B 66, 052301 (2002).

[16] FEW, G. A.; RIGBY, M. *Equation of state for systems of hard non-spherical molecules.* Chem. Phys. Lett. Vol 20, Issue 5, 433 (1973).

[17] FISCHERMEIER, E.; BARTUSCHAT, D.; PRECLIK, T.; MARECHAL, M. *Simulation of a hard-spherocylinder liquid crystal with the pe.* Comp. Phys. Comm. 185, 3156 (2014).

[18] FRENKEL, D.; LEKKERKERKER, H.N.W.; STROOBANTS, A. *Thermodynamic stability of a smectic phase in a system of hard rods.* Nature 332, 822 (1988).

[19] FRENKEL, D. *Order through entropy.* Nature Materials 14, 9 (2015).

[20] FRENKEL, D. *Structure of hard-core models for liquid crystals.* J. Phys. Chem. 92, 3280 (1988).

[21] GIACOMELLO, A.; CHINAPPI, M.; MELONI, S.; CASCIOLA, C. M. *Metastable Wetting on Superhydrophobic Surfaces: Continuum and Atomistic Views of the Cassie-Baxter–Wenzel Transition.* Phys. Rev. Lett. 109, 226102 (2012).

[22] GIACOMELLO, A.; CHINAPPI, M.; MELONI, S.; CASCIOLA, C.M. *Geometry as a Catalyst: How Vapor Cavities Nucleate from Defects.* Langmuir, 29 (48), 14873 (2013).

[23] GIACOMELLO, A.; MELONI, S.; CHINAPPI, M.; CASCIOLA, C.M. *Cassie–Baxter and Wenzel States on a Nanostructured Surface: Phase Diagram, Metastabilities, and Transition Mechanism by Atomistic Free Energy Calculations.* Langmuir 28, 10764 (2012).

[24] GIACOMELLO, A.; MELONI, S.; MÜLLER, M.; CASCIOLA, C. M. *Mechanism of the Cassie-Wenzel transition via the atomistic and continuum string methods.* J. Chem. Phys. 142(10), 104701 (2015).

[25] GIOVANNI, B.; TATYANA, Z. T. AND MICHELE, P. *Isothermal-isobaric molecular dynamics using stochastic velocity rescaling.* J. Chem. Phys. 130, 074101 (2009).

[26] GUO, Q.; LIU, Y.; JIANG, G.; ZHANG, X. *Condensation of droplets on nanopillared hydrophobic substrates.* Soft Matter 10, 1182 (2014).

[27] Guo, Q.; Liu, Y.; Jiang, G.; Zhang, X. *Cooperative effect in nucleation: Nanosized seed particles jointly nucleate vapor−liquid transitions.* J. Chem. Phys. 138, 214701 (2013).

[28] Henkelman, G.; Jónsson, H. *A dimer method for finding saddle points on high dimensional potential surfaces using only first derivatives.* J. Chem. Phys. 111, 7010 (1999).

[29] Jónsson, H.; Mills, G.; Jacobson, K. W. *Nudged Elastic Band Method for Finding Minimum Energy Paths of Transitions.* in Classical and Quantum Dynamics in Condensed Phase Simulations, edited by B. J. Berne et al. World Scientific, Singapore, 1998.

[30] Koishi, T.; Yasuoka, K.; Fujikawa, S.; Ebisuzaki, T.; Zeng, X. C. *Coexistence and transition between Cassie and Wenzel state on pillared hydrophobic surface.* Proc. Natl. Acad. Sci. U. S. A. 106, 8435 (2009).

[31] Kuijk, A.; Byelov, D.V.; Petukhov, A.V.; Blaaderen, A.; Imhof, A. *Phase behavior of colloidal silica rods.* Faraday Discuss 159, 181 (2012) .

[32] Laio, A.; Parrinello, M. *Escaping free-energy minima.* Proc. Natl. Acad. Sci. U. S. A. 99(20), 12562 (2002).

[33] Lennard-Jones, J. E. *Cohesion.* Proc. Phys. Soc. 43, 461 (2002).

[34] Li, Y.;Ren, W. *Numerical Study of Vapor Condensation on Patterned Hydrophobic Surfaces Using the String Method.* Langmuir, 30 (31), 9567 (2014).

[35] Liu, Y.; Men, Y.; Zhang, X. *How nanoscale seed particles affect vapor−liquid nucleation.* J. Chem. Phys. 135, 184701 (2011).

[36] Liu, Y.; Men, Y.; Zhang, X. *Nucleation mechanism for vapor-toliquid transition from substrates with nanoscale pores opened at one end.* J. Chem. Phys. 137, 104701 (2012).

[37] Lv, J.; Song, Y.; Jiang, L.; Wang, J. *Bio-inspired strategies for anti-icing.* ACS Nano 8, 3152 (2014).

[38] Maragliano, L.; Fischer, A.; Vanden-Eijnden, E. and Ciccoti G. *String method in collective variables: Minimum free energy paths and isocommittor surfaces.* J. Chem. Phys. 125, 024106 (2006).

[39] Maragliano, L.; Vanden-Eijnden, E. *On-the-fly string method for minimum free energy paths calculation.* Chem. Phys. Lett. 446, 182 (2007).

[40] Men, Y.; Yan, Q.; Jiang, G.; Zhang, X.; Wang, W. *Nucleation and hysteresis of vapor−liquid phase transitions in confined spaces: Effects of fluid−wall interaction.* Phys. Rev. E 79, 051602 (2009).

[41] Page, A. J.; Sear, R. P. *Heterogeneous nucleation in and out of pores.* Phys. Rev. Lett. 97, 065701 (2006).

[42] Punnathanam, S.; Monson, P. A. *Crystal nucleation in binary hard sphere mixtures: A Monte Carlo simulation study.* J. Chem. Phys. 125, 024508 (2006).

[43] Qiu, C.; Qian, T.; Ren, W. *Application of the string method to the study of critical nuclei in capillary condensation.* J. Chem. Phys. 129, 154711 (2008).

[44] Rebertus, D. W.; Sando, K. M. *Molecular dynamics simulation of a fluid of hard spherocylinders.* J. Chem. Phys. 67, 2585 (1977).

[45] Ren, W.; Vanden-Eijnden, E. *A climbing string method for saddle point search.* J. Chem. Phys. 138,134105 (2013).

[46] Ren, W. *Wetting Transition on Patterned Surfaces: Transition States and Energy Barriers.* Langmuir 30 (10), 2879 (2014).

[47] Rosso, L.; Mináry, P.; Zhu, Z.; Tuckerman, M.E. *On the use of the adiabatic molecular dynamics technique in the calculation of free energy profiles.* J. Chem. Phys. 116, 4389 (2002).

[48] SAVOY, E. S.; ESCOBEDO, F. A. *Molecular simulations of wetting of a rough surface by an oily fluid: Effect of topology, chemistry, and droplet size on wetting transition rates.* Langmuir 28, 3412 (2012).

[49] SAVOY, E. S.; ESCOBEDO, F. A. *Simulation study of free-energy barriers in the wetting transition of an oily fluid on a rough surface with reentrant geometry.* Langmuir 28, 16080 (2012).

[50] SCHILLING, T. AND FRENKEL, D. *Self-Poisoning of Crystal Nuclei in Hard-Rod Liquids.* Phys. Rev. Lett. 92, 085505 (2004).

[51] SEAR, R. P. *Heterogeneous and homogeneous nucleation compared: Rapid nucleation on microscopic impurities.* J. Phys. Chem. B 110, 4985 (2006).

[52] SHAHRAZ, A.; BORHAN, A.; FICHTHORN, K. A. *Wetting on physically patterned solid surfaces: the relevance of molecular dynamics simulations to macroscopic systems.* Langmuir 29 (37), 11632 (2013).

[53] SHEN, V. K.; DEBENEDETTI, P. G. *A computational study of homogeneous liquid−vapor nucleation in the Lennard-Jones fluid.* J. Chem. Phys. 111, 3581 (1999).

[54] STEINHARDT, P. J.; NELSON, D. R.; RONCHETTI, M. *Bond-orientational order in liquids and glasses.* Phys. Rev. B 28, 784 (1983).

[55] TRUDU, F.; DONADIO, D.; PARRINELLO, M. *Freezing of a Lennard-Jones fluid: From nucleation to spinodal regime.* Phys. Rev. Lett. 97, 105701 (2006).

[56] ULINE, M. J.; CORTI, D. S. *Activated instability of homogeneous bubble nucleation and growth.* Phys. Rev. Lett. 99, 076102 (2007).

[57] VANDEN-EIJNDEN, E.; CICCOTTI, G. Second-order integrators for Langevin equations with holonomic constraints. Chem. Phys. Lett. 429, 310 (2006).

[58] Veerman, J. A. C.; Frenkel, D. *Phase diagram of a system of hard spherocylinders by computer simulation.* Phys. Rev. A 41, 3237 (1990).

[59] Vieillard-Baron, J. *The equation of state of a system of hard spherocylinders.* Molecular Physics 28, 3 (1974).

[60] Wenzel, R. N. *Resistance of solid surfaces to wetting by water.* Ind. Eng. Chem. 28, 988 (1936).

[61] Winter, D.; Virnau, P.; Binder, K. *Monte Carlo test of the classical theory for heterogeneous nucleation barriers.* Phys. Rev. Lett. 103, 225703 (2009).

[62] Wu, H.; Borhan, A.; Fichthorn, K. A. *Interaction of fluids with physically patterned solid surface.* J. Chem. Phys. 133, 054704 (2010).

[63] Yasuoka, K.; Zeng, X. C. *Molecular dynamics of homogeneous nucleation in the vapor phase of Lennard-Jones. III. Effect of carrier gas pressure.* J. Chem. Phys. 126, 124320 (2007).

[64] Yu, T. Q.; Chen, P. Y.; Chen, M.; Samanta, A.; Vanden-Eijnden, E.; Tuckerman, M. *Order-parameter-aided temperature-accelerated sampling for exploration of crystal polymorphism and solid-liquid phase transitions* , J. Chem. Phys 140, 214109 (2014).

[65] Zeng, X. C. ; Oxtoby, D. W. *Gas−liquid nucleation in Lennard-Jones fluids.* J. Chem. Phys. 94, 4472 (1991).

[66] Zhang, Y.; Ren, W. *Numerical study of the effects of surface topography and chemistry on the wetting transition using the string method.* J. Chem. Phys. 141, 244705 (2014).